THE UNIVERSITY OF CHICAGO

CAVITY-QED TOOLS FOR QUANTUM INTERCONNECTS

A DISSERTATION SUBMITTED TO
THE FACULTY OF THE DIVISION OF THE PHYSICAL SCIENCES
IN CANDIDACY FOR THE DEGREE OF
DOCTOR OF PHILOSOPHY

DEPARTMENT OF PHYSICS

BY
LAVANYA TANEJA

CHICAGO, ILLINOIS
JUNE 2025

Abstract

Much like robust data interconnects in classical networks, photonic quantum interconnects will be essential for high-fidelity transmission of quantum information between spatially-separated nodes in a quantum network. For matter-based qubits, this requires efficient light-matter interactions to extract quantum information from qubits in the form of light and convert it to telecom wavelengths for low-loss transmission through fibers. Cavities, by modifying the electromagnetic environment of emitters and enhancing interaction strengths, provide a powerful tool for enabling such interfaces. Leveraging techniques from atomic physics, nonlinear optics and geometric optics, this thesis presents cavity-based schemes for frequency and spatial mode conversion of light, as well as new cavity architectures with intracavity optics. The first part of the thesis demonstrates transduction of millimeter-wave photons to near-infrared optical photons using an atomic ensemble coupled to a simultaneous optical-millimeter-wave cavity, achieving an internal conversion efficiency of 58(11)%, a conversion bandwidth of 360(20) kHz, and added thermal noise of 0.6 photons. Extending the idea of dual-cavity enhancement for frequency conversion, the thesis introduces an optical cavity with an intracavity nonlinear crystal that enables strong coupling between cavity modes for optical-to-optical frequency and spatial mode conversion. Additionally, by integrating macroscopic intracavity optics into moderate- to high-finesse cavities, this work demonstrates a large-scale cavity array with approximately 30 × 30 cavities, high-bandwidth modulation of a high-finesse cavity using an intracavity nonlinear crystal, cavities with lenses supporting finesses over 10,000, and cavities with patterned end-mirrors. These techniques provide pathways for efficient extraction and transfer of quantum information in the form of light, supporting applications in quantum networking, scalable modular architectures for

fault-tolerant quantum computing, and hybrid quantum systems. Beyond quantum information science, they also address technical challenges such as aberration correction in degenerate cavities and high-bandwidth cavity stabilization, while offering unique platforms for sensing and simulation.

To my parents and all my teachers

Table of Contents

List of Figures

List of Tables

Acknowledgments

First and foremost, I want to thank Jon and Dave for creating the most exciting lab opportunities that I could have asked for. Their scientific creativity, enthusiasm to adopt the state-of-the-art techniques, openness to feedback and to sharing science, and care for their team – are but a very few examples that made graduate school fulfilling. Jon's emphasis on a hands-on, quick-iteration approach to experiments and his knack for building simple yet accurate models of complex systems have left a deep impact on me, and I hope to continue cultivating these skills. I deeply appreciate Dave's support throughout my PhD, whether through guidance, sharing equipment (from regular amplifiers to dilution refrigerators), or behind-the-scenes support that I often was not even aware of. Just as importantly, I am immensely grateful to both Jon and Dave for building an amazing team around the science.

I feel fortunate for the chance to work with, and learn from, multiple generations of the Simon lab team. When I joined the hybrid lab, Mark's patient, clear explanations, and Aziza's energy and optimism, made the lab a welcoming and engaging place to work. Working with Ash on the transduction experiment was full of learning and productivity each day with his strong grasp on both theory and experiment. Tingran's energy and dedication as an undergraduate researcher were inspiring, and I am truly grateful for his significant contributions to the Floquet engineering project (and his patience with me!). Sasha's expertise with millimeter-waves and his willingness to share time and resources were crucial to the success of the transduction experiment. At Stanford, Zeyang's quick thinking and kindness made working together a pleasure. The first year graduate students, Xin and Abhishek, are already making important improvements to the experiment, and I wish them the best for their PhD journey.

Beyond the hybrid team, I appreciated learning from Nathan, Logan, and Clai's expertise during our brief overlap in my first year. Later on, Matt's organized and thoughtful ways of engaging in science and scientific conversations were consistently inspiring and helpful. His efforts, along with those of Lukas and Claire, made twisted lens cavities a well understood reality. Claire was always available as a sounding board for various science and life conversations and tirelessly kept us safe as the lab safety officer. Lukas streamlined the lab's experimental workflow in many ways, and his proactive efforts during the move took off a lot of stress from us. Chuan, Meg, and Gabrielle, my fellow 2018 cohortmates in Simonlab, made graduate school memorable through shared experience and shared science. Henry's calm and effortless approach to complex science was always appreciated and left a gap after his departure. Danial and Anna have carried the lab forward post-move with great spirit, and I am very excited about the developments in their experiment. I have appreciated both the insightful and the humorous moments during the very short overlap with Marius and Adam. Bowen, Cady, and Da-Yeon have brought fresh energy and momentum to a diverse set of experimental efforts, and I wish them all the best in the coming years.

I want to thank Prof. David Miller and Prof. Liang Jiang for their insightful input and time as my PhD committee members. Prof. Young-Kee Kim was instrumental in convincing me to join UChicago and in building a fun, close-knit department. Prof. David Reid and Prof. Zosia Krusberg helped me navigate the academic logistics of graduate school. Prof. Stuart Gazes, Shadla Caroll, Mark Chantell, David McCowan, and Kevin van de Bogart provided support as I carried out my teaching responsibilities.

I want to thank Luigi for sharing his expertise with machining, and for the many pleasant smiles and classic Hi's in the subbasement hallway. Many thanks are also due to the people in the Physics Departments at Chicago and Stanford who made daily life as a graduate student possible: Maria Jimenez, Brenda Thomas, Amy Schulz, Putri Kusomo, Nyein Mon, Darla Le-Grand-Sawyer, Nick Swan, An Nguyen, John Phillips, Bentley Wall, and many others. I also want to thank people at the companies that supported my research, especially the team at FiveNinesOptics for patiently enabling the rather wild request of a patterned HR mirror.

After my first summer as an undergraduate researcher in Kanpur, Prof. M.K. Harbola encouraged me to pivot from being an aspiring theorist to an experimentalist, and connected me with Prof. A.K. Jha, whose lab introduced me to the world of photons by trusting an undergraduate with an expensive SLM and EMCCD. I cannot imagine reaching the end of graduate school without the tireless efforts and support of teachers, professors and mentors from school, Kanpur, and beyond.

I am incredibly grateful to my friends for all the shared moments—big and small, near and far. Their company, patience, strength, humor, home-cooked food, and kind (and sometimes tough) love carried me through these past years. I also owe heartfelt thanks to my grandparents and family, whose love and blessings reached me even when we could not talk or see each other for long years at a time.

And finally, I want to thank my parents for being there in countless ways over the years, and for shaping me into the person and scientist I have become. I owe it all to them.

Chapter 1

Introduction

Light-matter interactions are an integral part of our interactions with the world around us. They are also the backbone of technologies such as lasers, cameras and displays, solar cells, long-distance communication, to name a few. A deeper understanding of light-matter interactions has helped us observe exciting phenomena such as photon entanglement [1–4], and enabled intricate control of individual atoms and collections of atoms [5–8].

In the recent years, studies of light-matter interaction have assumed importance in the context of development of quantum information processing. A deep understanding and control over these interactions enables precisely initializing, manipulating and detecting quantum states across platforms. As examples, atoms and solid state systems interact with electromagnetic radiation in the visible and near-infrared ranges, superconducting qubit platforms interact with microwave frequencies, and qubits based on light, in turn, rely on interactions with material such as non-linear crystals to change their states.

As these systems are maturing and growing in size, there is a need for 'quantum interconnects' [9] – capabilities that can move information[1] between different platforms and modalities. This is in analogy to the classical information ecosystem where classical comput-

---

[1] There are currently two common approaches, the 'pitch-and-catch' method, and the heralded entanglement method to effectively transfer the quantum states via photons, with the latter preferred for long-distance communication with optical photons.

ers rely on information being converted from one form to another and exchanged between different locations. Information is processed as voltages in transistors in our computer processors, converted to magnetic spins in a hard disk, broadcasted as electromagnetic radiation through Wi-Fi, and sent as photons over long distances in fibers. For quantum interconnects, light-matter interaction is crucial to coherently convert the fragile quantum information encoded in individual platforms to photons for movement. At the microscopic level, typical interactions of individual photons with matter tend to be very weak. For this reason, for matter-based qubits, reading out information in photons is desirable because of lower losses in transmission. Additionally, not all photon frequencies are suited for low-loss transmission between different spatial locations. Conversion of the readout signal to telecom wavelengths is preferred, again requiring the aid of light-matter interactions to mediate the conversion.

The ability to efficiently convert photons between different frequencies while preserving their quantum properties is crucial for the development of several practical quantum technologies:

1. In **quantum networks**, for example, the ability to interface similar or different quantum platforms requires coherent frequency conversion between their native operating frequencies. A particularly relevant example is the conversion between microwave and optical frequencies, which would enable long-distance quantum communication between superconducting quantum processors through optical fibers, circumventing the practical limitations of using cryogenic microwave transmission lines.

2. Interfacing **hybrid platforms**: Some quantum systems are better suited for one task over the other, for instance, superconducting qubits are great at high-fidelity gates [10] while diamond NV-centers are good quantum memories [11]. Even within a platform such as neutral atom arrays, using different species can enhance its capabilities. Interfacing between multiple platforms will be crucial to realize a fully capable quantum information processor.

3. In the present era of Noisy Intermediate-Scale Quantum (NISQ) devices, hardware

constraints necessitate **modular architectures** for implementing error correction to scale up quantum computers. Such architecture will require quantum repeaters and high-fidelity photonic interconnects between computational modules, where photons would serve as ideal information carriers.

1.1 Thesis themes

With weak light-matter interactions, the challenge lies in achieving such frequency conversion at the single-photon level while maintaining quantum coherence. **Cavities** offer a useful capability: they confine the electromagnetic field in a smaller volume in space, enhancing the absorption and emission of an emitter into the cavity mode compared to free space. Cavities have been crucial to the development of lasers, spectroscopy [12, 13], metrology [14–17], quantum information processing [18–24] and experimentally studying some of the fundamental aspects of quantum mechanics [4].

In this thesis, we will discuss experiments that explore the deployment of cavities for frequency coupling and conversion, and present new cavity designs with intracavity optics that could aid effective and scalable readout of matter-based optical qubits.

1.1.1 Cavity-enhanced frequency coupling and transduction

After a brief introduction (chapter 2) of cavity-QED concepts and terminology used throughout the thesis, a significant portion of this thesis will focus on dual-cavity-enhanced frequency coupling of light in two regimes:

1. **Millimeter-wave photons to optical photons** [25] (chapters 3 and 4): Using neutral Rubidium-85 atoms within a hybrid 3D superconducting resonator and an optical resonator in a cryogenic vacuum chamber, we demonstrate conversion between 100 GHz photons and 384 THz photons with an internal conversion efficiency of 58(11)% and an

external conversion efficiency of ~2.5%. At the maximum conversion, the bandwidth was measured to be 360(20) kHz. At the 5K operating temperature, we characterized the added noise of ~ 0.6 mean photons coming from the thermal background.

2. **Optical-optical photons** [26] (chapter 5): Using a frequency-coupling nonlinear crystal, we present a cavity that supports (Floquet) eigenmodes that exist at two optical wavelengths simultaneously. We demonstrate strong coupling of the optical modes and present proof-of-concept demonstrations of classical transduction from 780 nm to 516 nm with 30% overall conversion efficiency, and coupling higher-order spatial modes between the two frequencies.

In chapter 6, the thesis briefly discusses the similarities and differences between the two approaches.

1.1.2 Macroscopic intracavity optics

While working with a well initialized atomic ensemble of a few 1000s of atoms with a well defined energy structure inside a cavity does not introduce internal losses for the cavity, inserting macroscopic optics with $\mathcal{O}(10^{23})$ atoms compacted together into a solid invariably introduce more losses for light due to factors such as absorption by material, absorption due to presence of impurities during manufacturing and scattering off the bulk surface of the optic. However, once the losses are managed, intracavity optics such as lenses, lens arrays and nonlinear crystals can diversify the tool box of cavity QED by adding new functionality to cavities. After an overview of the primary loss mechanisms in chapter 7, the thesis will discuss experiments with

1. **Intracavity nonlinear crystals** (chapters 5 and 7) for RF- and optical- modulation of cavities. Using a nonlinear crystal as a phase modulator, the thesis demonstrates high-bandwidth cavity modulation and stabilization of high-finesse ($\mathcal{F} = 5000$) cavities,

and optical frequency coupling.

2. **Intracavity lenses** (chapters 7 and 8) to reduce cavity astigmatism for twisted resonators, build high-NA resonators for strong coupling to atoms at low finesse, and build nearly-degenerate cavities with non-vanishing waists to explore connectivity between spatially separated points in a cavity plane.

3. **Intracavity microlens array** (chapter 7) to scale to a cavity array of $\sim 30\times\ 30$ cavities.

We will conclude (chapter 9) with the prospects of combining these devices to aid cavity-based readout and networking. The appendices A.1-A.9 list additional calculations and material necessary to support the thesis.

Chapter 2

Cavity QED

In free space, emitters such as atoms couple weakly to the continuum of electromagnetic modes [27]. Cavities modify this interaction by supporting discrete, well-defined modes that the emitter can preferentially absorb from and emit into. This enhanced coupling positions cavities as effective tools for fast and efficient qubit-readout and frequency conversion. Strong coherent interactions enabled by cavities can also generate high-fidelity entanglement between emitters, essential for gates, quantum-enhanced metrology, and quantum simulation. The key figure of merit that quantifies the strength of cavity-mediated interactions relative to dissipation is the **cooperativity** $\mathcal{C}$, which captures the ratio of coherent interactions to dissipation.

This chapter lays the theoretical groundwork common for the experiments described in the remainder of the thesis. Section 2.1 focuses on optical Fabry-Pérot cavities, defining key cavity parameters and modeling cavity input-output response using Langevin equations—a formalism central to both the millimeter-wave and optical transducers presented later. Section 2.2 outlines a formal treatment of atom–cavity interactions, including the Jaynes–Cummings Hamiltonian and strategies for enhancing cooperativity. For in-depth description of fundamentals of cavity optics and light-matter interactions, the reader is referred to standard texts [27–30].

2.1 Optical Fabry-Pérot resonators

Let us consider a Fabry-Pérot cavity of length L formed by two curved mirrors with radii of curvature R_1 and R_2. The boundary conditions imposed by the mirrors on solutions to the paraxial wave equation (derived from the Helmholtz equation) yield discrete eigenmodes. The resonance condition for constructive interference every round trip requires that each mode accumulate a total phase of 2π upon a round trip. In a planar-mirror cavity, the modes can be understood simply by fitting integer multiples of half-wavelengths along the cavity axis. However, with curved mirrors, the Hermite-Gaussian profiles of transverse modes add an additional Gouy phase due to wavefront curvature, which is also included in the total round-trip phase.

Defining

$$g_1 = 1 - \frac{L}{R_1}, g_2 = 1 - \frac{L}{R_2}, \tag{2.1}$$

longitudinal mode index q and transverse mode indices (n, m), the resonance frequencies of the cavity are [28]

$$\nu_{qnm} = (q + \frac{n+m+1}{\pi} \arccos(\sqrt{g_1 g_2}))\frac{c}{2L}, \tag{2.2}$$

where $2(n+m+1)\text{arccos}(\sqrt{g_1 g_2})$ is the round-trip Gouy phase accrued by the mode.

2.1.1 Common terms and definitions

The **free-spectral range** (FSR) of the cavity is defined as the inverse of the cavity round trip time $T_{rt} = c/2L$. From Equation 2.2, every longitudinal mode is separated by the FSR in frequency. The **transverse-mode spacing** (TMS) is the spacing between consecutive transverse modes of the cavity, given by $TMS = FSR \times$ Round-trip Gouy phase$/2\pi$. The **linewidth** κ corresponds to the full-width half-maximum (FWHM) of the cavity transmission at resonance (a Lorentzian profile as will be seen in Section 2.1.3) and is a measure of losses in the cavity.

In the thesis, we shall use three terms extensively in the context of optimizing transducer conversion efficiencies: the external linewidth, the internal (coupling) linewidth and the total linewidth. The **external linewidth** solely accounts for contributions from necessary 'losses' from the coupling ports of the cavity, for example, transmission through an end mirror and is calculated by $\kappa_{\text{ext}} = T \times FSR$ (in angular frequency), where T is the transmission coefficient of the coupling mirror. The **internal linewidth** is determined by intrinsic losses in the cavity – absorption and scattering losses, or transmission through mirrors not being used for incoupling or outcoupling. The probability of the photon being in the cavity falls off as $\exp(-\kappa t)$, where $\kappa = \kappa_{\text{int}} + \kappa_{\text{ext}}$ is the **linewidth** (total linewidth) of the cavity, defined in terms of losses.

Two non-dimensional quantities of interest that also quantify losses in a cavity are the finesse $\mathcal{F}$ and the quality factor Q. The **finesse** is defined as $\mathcal{F} = FSR \times 2\pi/\kappa$. The number $N_{rt} = \mathcal{F}/2\pi$ quantifies the mean number of round-trips a photon makes inside the cavity before leaking out. In the limit that the round-trip loss $L_{rt} \ll 1$, the finesse can be equivalently calculated via the expression $2\pi/L_{rt}$. As we shall see in Section 2.2.4, for purposes of atom-cavity coupling or cavity-cavity coupling, the finesse assumes an important place instead of solely the linewidth because $\mathcal{F}$ is an indicator of the cavity enhancement of the interaction by the number of photon roundtrips.

The **quality factor** Q of an oscillator is the ratio of the total energy stored in the system to the total energy lost per cycle. For resonators, it is given by $Q = \omega_{res}/\kappa$. For Fabry-Pérot cavities, Q is related to $\mathcal{F}$ by $Q = \mathcal{F}\omega_{res}/(2\pi \times FSR)$. For non-Fabry-Pérot like cavities such as the 3D superconducting resonator discussed in Chapters 3 and 4, the FSR is not well-defined and Q is a more useful measure than $\mathcal{F}$.

2.1.2 Quantum Langevin equations for cavities and driven cavities

While classical-field descriptions of cavities[1] are useful for building intuition and performing many analyses, a quantum mechanical treatment requires quantizing the electromagnetic field. This is achieved using a mode-operator formalism, which not only enables a proper quantum description but also simplifies certain classical calculations. Without going into the theoretical rigor of second quantization, we start from the electric field operator and replace it with a bosonic cavity mode annihilation operator $a_\alpha(t)$ [30]

$$E_\alpha^{(+)}(\vec{r},t) \to -\sqrt{\frac{\hbar\omega_\alpha}{2\epsilon_0 V_\alpha}} f_\alpha(\vec{r}) a_\alpha(t), \tag{2.3}$$

where ω_α is the mode frequency, V_α is the mode volume, and $f_\alpha(\vec{r})$ is a dimensionless mode function, describing the normalized spatial profile of the mode.

To describe the dynamics of this quantized mode in an open system, one that is coupled to external inputs and subject to decay, we can use the Heisenberg-Langevin formalism. The Heisenberg-Langevin equations for the cavity annihilation operator $a(t)$ in a system with cavity Hamiltonian $H_{\text{cav}} = \hbar\omega_c a^\dagger a$, total decay rate or linewidth κ, coupling rate at the i^{th} port κ_i, and input flux a_i^{in} is given by

$$\partial_t a = -i\omega_c a(t) - \frac{\kappa}{2} a(t) - \sum_i \sqrt{\kappa_i} a_i^{\text{in}}, \tag{2.4}$$

where the first term is derived from the Heisenberg evolution $-\frac{i}{\hbar}[a, H_{\text{sys}}]$ and the last two terms are derived from the interaction of the cavity with the external bath $-\frac{i}{\hbar}[a, H_{\text{int}}]$, using the commutation relations $[a, a^\dagger] = 1$ and $[a, a^\dagger a] = a$. The second term represents damping and the third term represents an input to the cavity. The cavity mode operator and the

---

[1] Methods such as solving for steady-state intracavity fields using boundary conditions, or summing intracavity fields over multiple round-trips via a geometric series.

input can be related to the output via the input-output relation

$$a_i^{\text{out}}(t) - a_i^{\text{in}} = \sqrt{\kappa_i^{\text{ext}}} a(t) \tag{2.5}$$

2.1.3 Example: reflection and transmission from a driven cavity

For a double-ended cavity with coupling linewidths κ_i at the two ports, total linewidth κ and input at both ports, we can write

$$\partial_t a = -i\omega_c a(t) - \frac{\kappa}{2} a(t) - \sqrt{\kappa_1^{\text{ext}}} a_1^{\text{in}} - \sqrt{\kappa_2^{\text{ext}}} a_2^{\text{in}} \tag{2.6}$$

For a steady-state analysis for a driven cavity, it is helpful to switch to the frequency domain, so that the time-dependent operators can be replaced by frequency-domain operators. Assuming no input from the second port, we write for the cavity response to a drive at frequency ω:

$$(-i(\omega - \omega_c) + \frac{\kappa}{2}) a(\omega) = -\sqrt{\kappa_1^{\text{ext}}} a_1^{\text{in}}(\omega) \tag{2.7}$$

Solving for $a(\omega)$ and using the the input-output relations, we immediately get both the transmission $a_2^{\text{out}} = \sqrt{\kappa_2^{\text{ext}}} a(t) = \left(\frac{\sqrt{\kappa_1^{\text{ext}}}\sqrt{\kappa_2^{\text{ext}}}}{i(\omega-\omega_c)-\kappa/2} \right) a_1^{\text{in}}(\omega)$ and the reflection $a_1^{\text{out}} = \sqrt{\kappa_1^{\text{ext}}} a(t) + a_1^{\text{in}} = \left(1 + \frac{\kappa_1^{\text{ext}}}{i(\omega-\omega_c)-\kappa/2} \right) a_1^{\text{in}}(\omega)$. The fraction of photons transmitted and reflected can be calculated from $\left| \frac{a_2^{\text{out}}}{a_1^{\text{in}}} \right|^2$ and $\left| \frac{a_1^{\text{out}}}{a_1^{\text{in}}} \right|^2$.

2.2 Atom-cavity interaction

Having developed the formalism for modeling a cavity's response to external inputs, we now turn to the central feature of cavity QED: the interaction between a quantized field and a quantum emitter. The simplest case involves a two-level atom coupled to a single cavity mode, described by the Jaynes-Cummings Hamiltonian.

$$\begin{aligned}\hat{H}_{\text{JC}} &= H_{\text{cav}} + H_{\text{atom}} + H_{\text{int}} \\ &= \hbar\omega_c\, \hat{a}^\dagger \hat{a} + \tfrac{1}{2}\hbar\omega_0\, \hat{\sigma}_z + \hbar g\big(\hat{\sigma}^+ \hat{a} + \hat{\sigma}^- \hat{a}^\dagger\big)\end{aligned} \tag{2.8}$$

where $a^\dagger$ and a are the cavity mode creation and annihilation operators, $\sigma_z = |e\rangle\langle e| - |g\rangle\langle g|$, and σ^+ and σ^- are raising and lowering operators for the atom. g describes the rate of exchange of excitation between the atomic dipole μ with the atom initially in the ground state, and the electric field corresponding to one photon in the cavity at frequency ω and mode volume V_m

$$g_0 = \frac{\vec{\mu} \cdot \vec{E}_{\text{cav}}}{\hbar} = \sqrt{\frac{\mu^2 \omega}{2\epsilon_0 \hbar V_m}} \tag{2.9}$$

2.2.1 Vacuum Rabi Splitting

In the single-excitation subspace spanned by $\{|g,1\rangle, |e,0\rangle\}$, where $|g,1\rangle$ denotes the atom in the ground state (g) with one photon in the cavity mode, and $|e,0\rangle$ represents the atom in the excited state (e) with no photons in the cavity, the Jaynes-Cummings Hamiltonian can be written as a 2×2 matrix:

$$H^{(1)}_{\text{JC}} = \hbar \begin{pmatrix} \omega_c & g \\ g & \omega_0 \end{pmatrix}. \tag{2.10}$$

At resonance ($\omega_c = \omega_0$), the eigenvalues are $E_\pm = \hbar\omega_0 \pm \hbar g$, with an energy separation of $2\hbar g$ between the two eigenstates. In a spectroscopic measurement, one observes two peaks separated in frequency by $2g$ (figure 2.1a), referred to as the single-atom vacuum Rabi splitting (VRS).

More generally, when the system contains n excitations shared between the atom and the cavity field, the Jaynes-Cummings model predicts that the eigenstates are split by $2g\sqrt{n}$. This anharmonic energy level structure underlies the nonlinearity of cavity QED systems with a single atom.

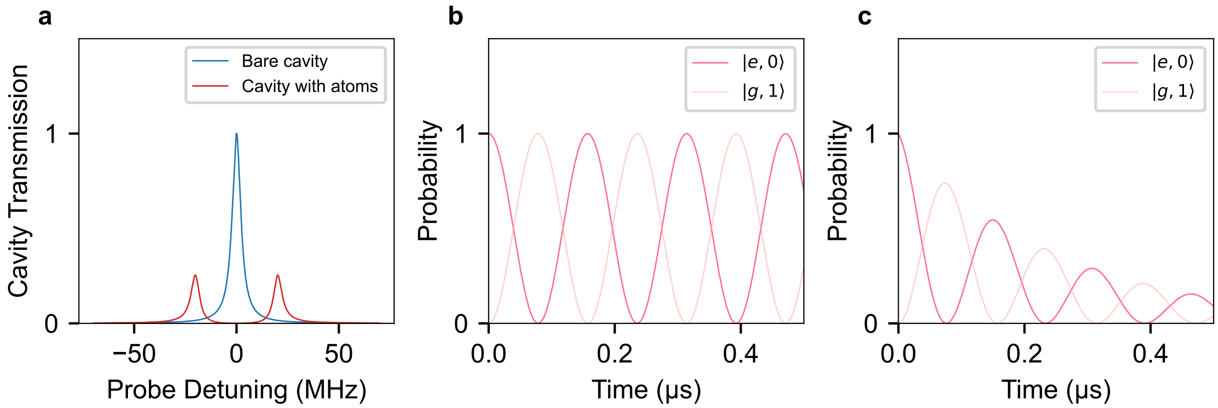

Figure 2.1: Vacuum Rabi splitting. (a) The cavity probe couples to the cavity modes which split in energy when coupled to atoms at resonance. The width of the split peaks have equal contributions from atom- and cavity- loss (b) Vacuum Rabi oscillations in time if there was no loss from atoms or cavity (c) Vacuum Rabi oscillations with loss.

Temporally, the energy between the atom and the cavity photon is continuously exchanged at rate g in the lossless case. If the system is initially prepared in $|e,0\rangle$ (atom excited, no cavity photons), the probability of finding the atom in the excited state at time t oscillates at frequency $\Omega_R = 2g$ (figure 2.1).

2.2.2 Spontaneous Emission

An excited two-level atom (or emitter) returns to its ground state by spontaneously emitting a photon into free space. The emission takes place due to an irreversible decay of the excited population due to its coupling with the electromagnetic mode continuum in free space.

One can model the atom-vacuum system in the interaction picture using the Wigner-Weisskopf approach. Suppose we have a two-level atom with ground $|g\rangle$ and excited $|e\rangle$ states, transition frequency ω_{ge} and a continuum of field modes labeled by wavevector $\vec{k}$ and polarization λ, each with frequency ω_k.

The interaction Hamiltonian in the rotating-wave approximation (RWA) takes the form

$$\hat{H}_{\text{int}} = \hbar \sum_{\mathbf{k},\lambda} \Big(g_{\mathbf{k},\lambda}\, \hat{\sigma}_{+} \hat{a}_{\mathbf{k},\lambda} + g^{*}_{\mathbf{k},\lambda}\, \hat{\sigma}_{-} \hat{a}^{\dagger}_{\mathbf{k},\lambda} \Big), \tag{2.11}$$

where $g_{\mathbf{k},\lambda}$ is the atom–field coupling strength and $\hat{\sigma}_{\pm}$ are the atomic raising and lowering operators. The total state can be written as $|\Psi(t)\rangle = c_e(t)\ |e\rangle\,|0\rangle + \sum_{\mathbf{k},\lambda} c_{\mathbf{k},\lambda}(t)\ |g\rangle\,|1_{\mathbf{k},\lambda}\rangle$, where $|0\rangle$ is the vacuum state of the electromagnetic field, and $|1_{\mathbf{k},\lambda}\rangle$ denotes a single photon in mode $(\mathbf{k}, \lambda)$. Under the Born–Markov and rotating-wave approximations [30], one obtains an exponential decay for $c_e(t)$:

$$\dot{c}_e(t) \approx -\frac{\Gamma}{2}\, c_e(t), \text{so that } c_e(t) \approx c_e(0)\, e^{-\frac{\Gamma}{2}t} \tag{2.12}$$

where Γ is the spontaneous emission rate. Thus, in free space, the atom's excitation decays irreversibly and the energy is radiated into many possible modes of the electromagnetic field.

2.2.3 Purcell-enhancement of spontaneous emission into cavity

In Section 2.2.1, we assumed that the cavities are lossless, which is not true experimentally and the cavity decay rate has to be considered. In the good cavity limit, when $g \gg \kappa$, the coherent exchanges as discussed for vacuum Rabi oscillations are primarily limited by the atomic lifetime.

In the bad-cavity limit, when $g \ll \kappa$, the rate of coupling of the atoms to the cavity mode can be calculated to be $4g^2/\kappa$.[2] The total decay rate of the atom is set by

$$\begin{aligned}\Gamma_{\text{total}} &= \Gamma + \text{Rate of coupling to the cavity mode} \\ &= \Gamma + \frac{4g^2}{\kappa} \\ &= \Gamma\left(1 + \frac{4g^2}{\kappa\Gamma}\right) = \Gamma(1+\mathcal{C})\end{aligned} \tag{2.13}$$

where $\mathcal{C} = 4g^2/\kappa\Gamma$ is defined as the cooperativity. Physically, in free-space, the atomic-dipole emits isotropically into 4π, however the cavity preferentially makes it interact more with the cavity mode and hence emit into or coherently interact with the cavity mode. Equation 2.13 also shows that the collection efficiency of the cavity mode is $\frac{\frac{4g^2}{\kappa}}{\Gamma(1+\frac{4g^2}{\kappa\Gamma})} = \frac{\mathcal{C}}{1+\mathcal{C}}$.

2.2.4 Quest for higher cooperativity

While we introduced cooperativity through the lens of spontaneous emission enhancement, its significance extends beyond spontaneous decay. The same principles apply to more general light–matter interactions where the emitter couples to the quantized field. Although spontaneous emission is characterized by the decay rate Γ, what fundamentally matters in these interactions is the strength and directionality of the coupling between the emitter and the available electromagnetic modes. The cavity modifies this coupling by selectively enhancing certain field modes, thus altering not just decay rates but also scattering rates.

The cooperativity quantifies the competition between coherent coupling and dissipative loss arising from cavity decay and emitter decoherence. Achieving the strong-coupling regime ($\mathcal{C} \gg 1$) ensures that coherent dynamics such as vacuum Rabi oscillations persist over many cycles before being damped by irreversible processes. High cooperativity is a key

---

[2] This rate can be derived from a master equation treatment of the atom-cavity system. Phenomenologically, the same result can be obtained by applying Fermi's Golden Rule with a cavity-modified density of states, $\rho_{\text{cav}}(\omega) = \frac{\kappa}{2\pi V_m}\frac{1}{(\kappa/2)^2+(\omega_c-\omega)^2}$. In the bad-cavity regime, the cavity field relaxes much faster than the atomic system evolves, justifying this Wigner-Weisskopf-like Markovian treatment.

figure of merit for a wide range of tasks in quantum information processing, including fast state readout, efficient transduction, and high-fidelity gate operations. For atomic readout, high cooperativity enables faster photon extraction into the cavity mode, improving signal collection efficiency [31]. In the context of transduction, as will be discussed in the following chapters, cooperativity determines how effectively the mediator couples to both input and output cavity modes. Large cooperativity ensures that desired coupling rates dominate over loss channels, allowing for near-unity photon conversion efficiency in principle. Furthermore, the cooperativity sets a lower bound on the error rate of cavity-mediated quantum gates, with the infidelity scaling as $\epsilon = 2\pi/\sqrt{2C}$ [32]. There are many routes to enhancing cooperativity:

2.2.4.1 Interaction with atomic ensembles

When an ensemble of N identical atoms interacts collectively with a single cavity mode, the effective atom-cavity coupling is enhanced to $g_N = \sqrt{N}g$, where g is the single-atom coupling strength (Appendix A.2). This enhancement arises from the coherent interaction of the cavity field with a symmetric collective excitation of the ensemble[3], in which all atoms participate equally. As a result, the collective cooperativity scales as $C_N = NC$, where C is the single-atom cooperativity.

Unlike a single atom, which can be saturated by a single photon, a large ensemble does not saturate with a single excitation. The cavity field can excite one atom out of the ensemble with negligible effect on the remaining atoms, allowing multiple interactions. In the large N limit, the energy level structure of the combined atom-cavity system begins to resemble that of a harmonic oscillator (Appendix A.2), where excitations are evenly spaced and multiple

---

[3] A note on collective states: Calculations for the ensemble can be greatly simplified by working with *collective* states for the atom such as the $|gggg...\rangle$ state where all atoms are in the ground state. In the single excitation limit, interaction with the cavity accesses the state that is the symmetric superposition of $|gggg..e_i..g\rangle$ terms. Using the Holstein-Primakoff transformation, the accessible space can be mapped onto an N-spin-1/2 system, with the raising and lowering operators defined as bosonic operators (see Appendix A.2). In this mapping, the collective spin-$N/2$ system behaves like a truncated harmonic oscillator, where each rung of the ladder corresponds to a symmetric Dicke state with a well-defined number of collective excitations.

photons can enter the cavity without fundamentally changing the system's dynamics. In this limit, the nonlinearity inherent in the Jaynes–Cummings model, where the energy spacing between successive excitation levels depends on the excitation number, effectively disappears, and the system responds linearly for low excitation numbers.

For applications such as transduction, where strong nonlinearity is not required, the boost in cooperativity provided by an ensemble is particularly valuable for increasing the absorption (emission) of input (output) photons by the atoms. As we shall see in Chapter 3, even with a moderate finesse optical cavity, it is possible to achieve collective cooperativity exceeding unity and see a resolvable (collective) vacuum Rabi splitting.

2.2.4.2 Rydberg states

Internal states of atoms corresponding to a high principal quantum number, termed Rydberg states, are widely used to induce strong, tunable interactions between atoms due to their large electric dipole moment. Rydberg state transitions also provide access to lower frequency microwave transitions and have long lifetimes. While ground-state hyperfine transitions in the microwave regime benefit from extremely long coherence times, their weak magnetic dipole coupling leads to relatively small g. In contrast, Rydberg transitions can provide stronger atom-cavity coupling through electric dipole coupling, making them useful for improving cooperativity at microwave frequencies.

2.2.4.3 Resonator design

The single-atom cooperativity for a closed optical transition at resonance with a cavity can be expressed solely in terms of the cavity parameters, involving cavity finesse $\mathcal{F}$, cavity waist w and resonance wavelength λ [33]

$$\mathcal{C} = \frac{12}{\pi^2}\frac{\mathcal{F}}{2\pi}\frac{\lambda^2}{w^2} \tag{2.14}$$

The strong-coupling regime can be accessed by minimizing w^2/λ^2 [34, 35], maximizing $\mathcal{F}$ as enabled by highly reflective mirrors [23, 36–38], by minimizing the waist [20, 32, 39] or a mixture of factors [40].

Chapter 3

Millimeter-wave to optical transduction: Background

This chapter is based on reference [25].

3.1 Introduction

Quantum states encoded in superconducting qubits and certain semiconductor spin qubits are read-out in the microwave frequency regime [41]. However, the microwave frequency regime is not ideal for transfer of the fragile quantum states because of transmission losses at room temperature (hence limited range) and thermal background, requiring cryogenic links [42, 43] which are impractical for large scale networking and communication. Coherently converting single photons between microwave and optical frequencies is thus crucial for long distance communication between superconducting qubit-based platforms.

A fast, efficient optical interface between microwave photons and atoms is also promising for hybrid systems that can combine the strengths of different platforms available to us. Rydberg states and hyperfine ground states of atoms have much longer lifetimes compared to superconducting qubits, making atoms promising candidates for memory qubits, in addition to rapid developments in processing [44].

There is a large body of previous work [45–50] aimed at microwave-to-optical transduction, with efforts directed towards using electro-optic, nano-mechanical, and piezoelectric coupling. We take a different approach, using neutral ^{85}Rb atoms as mediators for conversion between millimeter-wave (100GHz) photons and optical (384THz) photons. Our platform leverages the optical and microwave transitions of the atoms, combined with dual-cavity enhancement, to facilitate frequency conversion.

This chapter provides background for the millimeter-wave to optical interconversion experiment. Section 3.2 presents an overview of the transduction scheme. Section 3.3 describes the cryogenic apparatus and experimental sequence utilized for transduction. Section 3.4 discusses the theoretical model of the transducer and provide an expression for the conversion efficiency in terms of different coupling and loss rates in the system. Section 3.5 presents our methods of characterizing those rates. It also discusses our methods of measuring and tuning the millimeter-wave atomic transition frequency, and calibrating intracavity millimeter-wave photon number. Section 3.6 discusses the incorporation of the 297 nm UV laser to the apparatus. The rest of the chapter discusses the steps undertaken to increase experimental data rates (Section 3.7) that enabled fast optimizations and temporal correlation function measurements, our method of optimizing magnetic fields for optical pumping inside a superconducting cavity (Section 3.8), optical single photon detection (Section 3.9) and the method of extracting conversion efficiency from intracavity millimeter-wave photon number and optical photon count rate (Section 3.10).

3.2 Transduction scheme

We utilize the atomic levels of ^{85}Rb shown in figure 3.1a. The $|5S\rangle \rightarrow |5P\rangle$ and $|35P\rangle \rightarrow |36S\rangle$ transitions correspond to 780 nm (384 THz) and 100 GHz respectively. Strong coherent drives at 481 nm (blue) and 297 nm (UV) couple the lower-lying states to the higher-lying

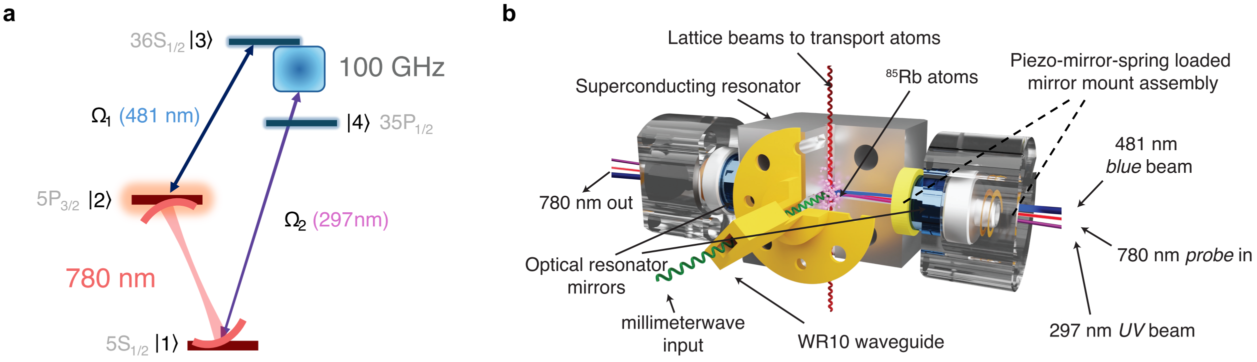

Figure 3.1: Transduction (a) scheme and (b) platform

Rydberg states. The atom-field interaction at 100 GHz is enhanced by a near-resonant superconducting cavity. At 780 nm, the cooperative enhancement is achieved via a resonant optical cavity, with a large portion of the enhancement derived from the collective interactions of the entire atomic ensemble with the cavity. Unlike electro-optic platforms, the optical pumps in this scheme are far separated from the frequencies of interest and don't add noise to the scheme. Thermal photon background at the operating temperature 5 K is the primary source of added noise in the system.

The UV laser is sufficiently detuned from the transition such that a very small population of atoms is in the $35\mathrm{P}_{1/2}$ Rydberg state on average, dressing the ground state with the Rydberg state and reducing the system to an effective three-level system. The dressed population in the $35\mathrm{P}_{1/2}$ state is sufficient for the absorption of a millimeter-wave photon from the cavity, which puts the ensemble in a collective $36S_{1/2}$ Rydberg state. From there, a stimulated emission process of a blue photon and spontaneous emission of a 780 photon into the optical cavity brings the atomic ensemble back to collective dressed ground state[1]. It is important for the ensemble to return to the same many-particle quantum state including all the internal and motional degrees of freedom. This ensures that minimal coherence is lost

---

[1] The two-photon resonance at the 780 nm cavity and 481 nm Rydberg transition effectively eliminates the undesired losses from the intermediate, broad $5\mathrm{P}_{3/2}$ state and is discussed more in section 3.5.2 and chapter 6.

to the atoms, enabling taking advantage of collective cavity enhancement[2] and preserving information in the photons. In addition to energy conservation, closing the transduction loop requires momentum conservation via phase-matching (Section 3.6.2) and spatial mode-matching of the different fields at the atom cloud.

3.3 Apparatus and experimental sequence

The transduction takes place inside the structure shown in figure 3.1b. The experiment utilizes an approximately 1" x 1" x 1" superconducting niobium spacer housing two evanescent modes near 100 GHz. The three perpendicular holes drilled into the spacer act as evanescent waveguides forming a cavity at their intersection in the center [51]. One of the holes is used to provide optical access for the optical cavity. The second hole is used as a port to drive the millimeter-wave cavity. The third hole is used for transporting the atomic ensemble to the center so that it can interact with both the optical cavity and the millimeter-wave cavity simultaneously. A detailed description of the physical apparatus can be found in References [51, 52].

A typical experimental sequence begins with loading ^{85}Rb atoms from a dispenser into a 3D holographic-grating magneto-optical trap (MOT) [51, 52]. After polarization-gradient-cooling to $\sim$5 μK (measured via time-of-flight measurements [51]), the MOT atomic cloud is loaded into a 785 nm transport lattice and transported $\sim$ 6.5 cm below into the cavities [52].

To ensure angular momentum conservation for interconversion, we choose our quantization axis to be in the lattice transport direction orthogonal to the optical cavity axis (figure 3.1a) and utilize the hyperfine levels and corresponding transitions as shown in figure 3.2. After transport, the atomic ensemble is optically pumped to the $|5S_{1/2}, F = 3, m_F = 3\rangle$ hyperfine ground state using σ^+ polarized light on the transition to the $|5P_{3/2}, F = 3, m_F = 3\rangle$

---

[2] Coupling to states that are not the symmetric Dicke-states leads to a decrease in coupling G_{opt}, hence cooperativity.

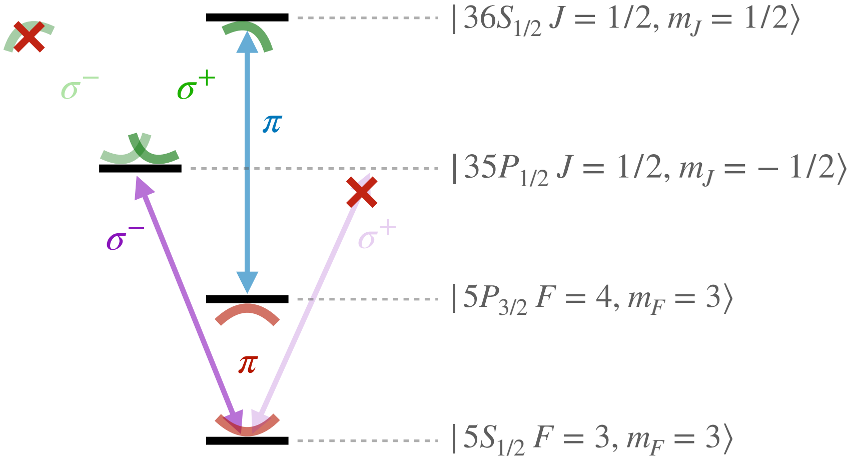

Figure 3.2: Hyperfine levels and polarizations for interconversion

state. A magnetic field of about 3.2 G, optimized for optical pumping, was previously 'frozen' in the superconducting cavity along the lattice direction.The transport lattice is reduced to a depth of about 20% to prevent broadening of the dark polariton due to differential light shifts for atoms depending on their spatial position in the trap.

After the state preparation of atoms, we operate the transducer by driving the ensemble with classical coherent pumps at 297 nm (UV) and 481 nm (blue). The total 'on time' of the UV beam is limited to below 300 μs per shot to avoid damage to cavity mirrors from UV exposure (section 3.6.1). The transducer is driven with a coherent millimeter-wave source attenuated to the single photon level, and the optical photons are detected at the output.

For coherent millimeter-wave drive conversion, each shot involves five 10 μs long transduction steps separated by 50 μs of optical pumping. The optical pumping is required because the conversion cycle depolarizes the atoms because the transition corresponding to the optical cavity is not a cycling transition in the current experiment design. The depolarization depends on the external millimeter-wave drive strength (next chapter), so we do not always require the intermediate optical pumping as in the case of measuring conversion of thermal millimeter-wave photons in the cavity at 5K in the absence of an external drive.

3.4 Theoretical model

The full Hamiltonian can be written including all the atoms in the ensemble and the four states of interest, the two coherent drives and the millimeter-wave and optical cavity modes, after the time-dependence is removed through a unitary transformation and ensuring energy conservation[3]:

$$\begin{aligned}H = {} & \delta_a \hat{a}^\dagger \hat{a} + \delta_b \hat{b}^\dagger \hat{b} + \delta_e E^\dagger E + \delta_r R^\dagger R + \Delta F^\dagger F \\ & + \Big(g_{opt}\sqrt{N}\hat{a}E^\dagger + \Omega_b E R^\dagger + g_{mm}\hat{b}^\dagger F^\dagger R + \sqrt{N}\Omega_{UV} F^\dagger + h.c \Big)\end{aligned} \tag{3.1}$$

where E, R and F are the bosonized collective excitation operators (Appendix A.2) to the $5P_{3/2}$, $36S_{1/2}$ and the $35P_{1/2}$ states respectively, from a reservoir of N atoms prepared in the $5S_{1/2}$ ground state, g_{opt} and g_{mm} are the single atom coupling strengths for the optical (a) and millimeter-wave (b) cavity modes, and Ω_b and Ω_{UV} are the Rabi frequencies for the 481 nm and UV fields.

We can write the Heisenberg-Langevin equations for the Hamiltonian in equation 3.1:

$$\begin{aligned}\dot{a} &= (i\delta_a - \frac{\kappa_{opt}}{2})a - i\sqrt{N}g_{opt}E + \sqrt{\kappa_o^{ext}}a_{in}(t) \\ \dot{E} &= (i\delta_e - \frac{\Gamma}{2})E - i\sqrt{N}g_{opt}a - i\Omega_b R \\ \dot{R} &= (i\delta_r - \frac{\Gamma_R}{2})R - i\Omega_b^* E + ig_{mm}bF \\ \dot{b} &= (i\delta_b - \frac{\kappa_{mm}}{2})b - ig_{mm}RF^\dagger + \sqrt{\kappa_{mm}^{ext}}b_{in}(t) \\ \dot{F} &= (i\Delta - \frac{\Gamma_F}{2})F - ig_{mm}Rb^\dagger - i\sqrt{N}\Omega_{UV}\end{aligned} \tag{3.2}$$

where the external linewidths and total linewidths of the cavities, the total decay and dephasing rates of the collective states, and the inputs to the cavities have been included.

---

[3] See supplemental information to reference [25] for a derivation of the conversion efficiency starting from the full time-dependent Hamiltonian.

We operate the interconverter with a detuning between the millimeter-wave atomic transition and the millimeter-wave cavity. The constraint of energy conservation (equivalently, time independence of the Hamiltonian), necessitates that the UV drive be detuned from the 5S to 35P transition as well. In the limit[4] that $\Omega_{UV} \ll |\Delta|$ and greater than millimeter-wave coupling g_{mm}, the small nonlinear term $g_{mm}Rb^\dagger$ in the equation for $\dot{F}$ can be neglected and operator F can be adiabatically eliminated by setting $\langle \dot{F} \rangle = 0$, yielding $\langle F \rangle = \frac{\sqrt{N}\Omega_{UV}}{\Delta - i\Gamma_F/2}$. In the limit $|\Delta| \gg \Gamma_F/2$, the decay can also be neglected. Replacing the operator F by its average value linearizes the Heisenberg-Langevin equations, simplifying the term $-ig_{mm}RF^\dagger$ in the equation for $\dot{b}$ to $-iG_{mm}R$, where $G_{mm} = \frac{\sqrt{N}\Omega_{UV}}{\Delta}g_{mm}$.

Similar to the single cavity calculation, we transform equations 3.2 to the Fourier space, and reduce the problem to a set of simultaneous equations $\mathbf{G}(\omega)\mathbf{v}(\omega) + \mathbf{u}(\omega) = \mathbf{0}$, where at atomic and cavity resonances ($\delta_i = 0$)

$$\begin{aligned}
v(\omega) &= \begin{pmatrix} a(\omega) & E(\omega) & R(\omega) & b(\omega) \end{pmatrix}^T \\
u(\omega) &= \begin{pmatrix} \sqrt{\kappa_{opt}^{\text{ext}}}a_{\text{in}}(\omega) & 0 & 0 & \sqrt{\kappa_{mm}^{\text{ext}}}b_{\text{in}}(\omega) \end{pmatrix}^T \\
G(\omega) &= \begin{pmatrix} i\omega - \frac{\kappa_{opt}}{2} & -iG_{opt} & 0 & 0 \\ -iG_{opt} & i\omega - \frac{\Gamma}{2} & -i\Omega_b & 0 \\ 0 & -i\Omega_b & i\omega - \frac{\Gamma_R}{2} & -iG_{mm} \\ 0 & 0 & -iG_{mm} & i\omega - \frac{\kappa_{mm}}{2} \end{pmatrix}
\end{aligned} \tag{3.3}$$

3.4.1 Transducer transfer function and conversion efficiency

For an input $b_{\text{in}}(\omega)$, the output $a_{\text{out}}(\omega)$ can be calculated from the input-output relation $a_{\text{out}}(\omega) = \sqrt{\kappa_{opt}^{\text{ex}}}a(\omega)$. We set $a_{in}(\omega) = 0$ because there is no significant thermal input at the optical side. We define a transfer function $S(\omega)$ from the input of the millimeter-wave

---

[4] See supplemental information to reference [25] for details.

cavity and the output of the optical cavity such that

$$\begin{aligned} a_{out}(\omega) &= S(\omega) b_{in}(\omega) \\ \langle a_{out}^\dagger(\omega) a_{out}(\omega)\rangle &= |S(\omega)|^2 \langle b_{in}^\dagger(\omega) b_{in}(\omega)\rangle \end{aligned} \tag{3.4}$$

$|S(\omega)|^2$ provides a conversion efficiency. Writing $S(\omega)$ explicitly

$$S(\omega) = \sqrt{\frac{\kappa_{opt}^{ext}\kappa_{mm}^{ext}}{\kappa_{opt}(\omega)\kappa_{mm}(\omega)}} \frac{2\sqrt{C_o(\omega)C_{mm}(\omega)C_b(\omega)}e^{i\phi}}{(C_b(\omega) + (1 + C_o(\omega))(1 + C_{mm}(\omega)))} \tag{3.5}$$

where $\gamma_j(\omega) \equiv \gamma_j - 2i\omega$ for $\gamma_j \in \{\kappa_{opt}, \kappa_{mm}, \Gamma, \Gamma_R\}$, ϕ is the phase difference between the 481 nm and the UV beams in the rotating frame, and $C_o(\omega) = \frac{4|G_{opt}|^2}{\kappa_{opt}(\omega)\Gamma(\omega)}$, $C_b(\omega) = \frac{4|\Omega_b|^2}{\Gamma(\omega)\Gamma_R(\omega)}$, and $C_{mm}(\omega) = \frac{4|G_{mm}|^2}{\kappa_{mm}(\omega)\Gamma_R(\omega)}$ are generalized frequency-dependent cooperativities.

At resonance,

$$|S(0)|^2 = \frac{\kappa_{opt}^{ext}\kappa_{mm}^{ext}}{\kappa_{opt}\kappa_{mm}} \frac{4C_oC_bC_{mm}}{(C_b + (1 + C_{mm})(1 + C_o))^2} \tag{3.6}$$

where the generalized cooperativities are evaluated at $\omega = 0$. We identify the overall conversion efficiency ϵ with $|S(\omega)|^2$ and an internal conversion efficiency [53] denoted by $\eta_{o\leftrightarrow mm}$ such that

$$\epsilon = \frac{\kappa_{opt}^{ext}\kappa_{mm}^{ext}}{\kappa_{opt}\kappa_{mm}}\eta_{o\leftrightarrow mm} \tag{3.7}$$

3.4.2 Impedance matching

For a fixed C_b, the internal conversion efficiency η is maximized when

$$\mathcal{C}_{mm} = \mathcal{C}_o = \sqrt{1 + \mathcal{C}_b} \tag{3.8}$$

Physical intuition: For all the millimeter-wave cavity photons to be absorbed by the atoms, we require that the rate of coupling of photons to the atoms either goes to the useful atomic state or is lost (we have no control over that rate). The rate at which the atoms couple to the cavity should be equal to the rates at which the photon is lost from the atom or coupled to the lower excited state.

$$\frac{4G_{mm}^2}{\kappa_{mm}} = \Gamma_R + \frac{4\Omega_b^2}{\frac{4G_{opt}^2}{\kappa_{opt}} + \Gamma}$$

The term on the LHS is the rate at which the cavity photons excite the atoms, the first term on RHS is the rate at which the atom excitation is lost to the environment, and the second term is the rate at which the excitation is transferred to the lower state. The denominator $\frac{4G_{opt}^2}{\kappa_{opt}} + \Gamma$ in the second term sums up all loss channels from the lower atomic level (via coupling to the optical cavity and spontaneous emission). The condition can be rewritten as:

$$\left(\frac{4G_{mm}^2}{\kappa_{mm}\Gamma_R} - 1\right)\left(\frac{4G_{opt}^2}{\kappa_{opt}\Gamma} + 1\right) = \frac{4\Omega_b^2}{\Gamma_R\Gamma} \tag{3.9}$$

$$(\mathcal{C}_{mm} - 1)(\mathcal{C}_o + 1) = \mathcal{C}_b \tag{3.10}$$

Due to the symmetry between a → b and b → a conversions, the $\mathcal{C}_{mm}$ and $\mathcal{C}_o$ can be exchanged, providing the impedance-matching condition:

$$\mathcal{C}_{mm} = \mathcal{C}_o = \sqrt{1 + \mathcal{C}_b} \tag{3.11}$$

yielding an optimum internal conversion efficiency, that in the limit of high C_b is

$$\eta \xrightarrow[C_b \gg 1]{} 1 - \frac{2}{\sqrt{C_b}} \tag{3.12}$$

3.5 Machine characterizations

3.5.1 Collective vacuum Rabi splitting

As discussed in the previous chapter, coupling a single atom to a cavity mode leads to a splitting in the cavity spectrum. In the presence of multiple identical atoms, the splitting is increased by a factor of $\sqrt{N}$[5]. A typical optical cavity transmission spectrum from our experiment is shown in figure 3.3 with $G_{opt} = 2\pi \times 8$ MHz when the cavity couples to the 5S-5P transition near 780 nm. For interconversion, the optimum operation was at $G_{opt} = 2\pi \times 5$ MHz, with an effective atom number in the ground state of about 600.

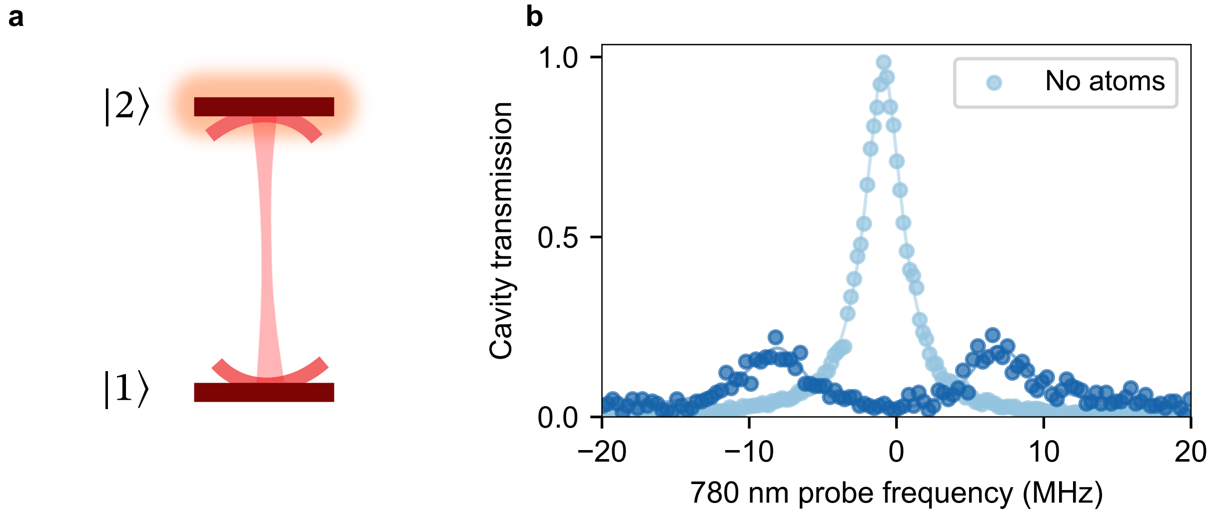

Figure 3.3: Vacuum Rabi splitting. (a) Optical cavity at resonance with the atomic transition. (b) Vacuum Rabi splitting ($= 2\sqrt{N_{\text{atoms}}}\ g$) of the cavity transmission peak due to coupling with the atomic ensemble. This spectrum corresponds to the transition $|5S_{1/2}, F = 3, m_F = 3\rangle \rightarrow |5P_{3/2}, F = 4, m_F = 4\rangle$.

Extracting the number of atoms from the splitting requires knowledge of the single-atom

---

[5] The vacuum Rabi splitting of $2G_{opt} = 2\sqrt{N}g_{opt}$ can be formally derived from the coupling of the cavity vacuum with the lowest excitation manifold of an ensemble of N atoms, with single-atom cavity coupling g_{opt} (Appendix A.2). Another interesting route is to model the cloud of atoms as a medium with frequency dependent refractive index, leading to a change in the cavity resonance conditions and consequent splitting in the spectrum [54].

cavity coupling g_{opt}. For our experiment, $g_{opt} = 2\pi \times 206$ kHz is calculated[6] from equation 2.9. It should be noted that the vacuum Rabi splitting is observed due to interactions of the atomic ensemble with the *standing-wave* of the cavity, not just one running-wave component which primarily contributes to interconversion due to momentum-conservation. Hence, the measured splitting carries an extra factor of $\sqrt{2}$ such that $G_{opt} = \frac{G_{opt,\text{measured from VRS}}}{\sqrt{2}}$.

3.5.2 Blue Rabi frequency and Γ_R: Cavity Rydberg EIT

To calibrate the blue Rabi frequency, we implement a cavity Rydberg Electromagnetically Induced Transparency (EIT) scheme [56–60]. In this scheme, in addition to the optical cavity coupling to the 5S-5P transition, a coherent 481 nm drive couples the 5P state to the 36S Rydberg state. At two-photon resonance, quantum interference of probability amplitudes eliminates the participation of the broad 5P state ($\Gamma = 6$ MHz) in one of the three system eigenstates, preventing absorption via this lossy intermediate state.

This state – the 'dark polariton' – is a superposition of the cavity photon (entangled with the atomic ground state) and the collective Rydberg state. Its linewidth γ_D follows $\gamma_D \approx \kappa\ \cos^2\theta + \Gamma_R\ \sin^2\theta$, where $\tan\theta = G_{opt}/\Omega_b$ defines the dark polariton angle. When $G_{opt} > \Omega_b$, the state is more Rydberg-like, and vice versa. For the interconverter, we operate in the Rydberg-dominated regime with $G_{opt} \sim 2\pi \times 5$ MHz and $\Omega_b \sim 2\pi \times 1.45(5)$ MHz (Figure 3.4), resulting in a narrow dark polariton linewidth. We also extract Γ_R from the dark polariton feature, which is primarily limited by Doppler broadening. This is after the suppression of Doppler broadening to linear scaling with ensemble temperature by the cavity EIT scheme [56]. For comparison, the bare 36S Rydberg state linewidth is expected to be $2\pi \times 3.6$ kHz according to the python package `arc`. Note that for the experiment parameters presented in the next chapter, we use the fit to the EIT spectrum to extract the value of G_{opt} as well.

---

[6] In an atom projection-noise limited measurement of the cavity spectrum, the quantities can also be

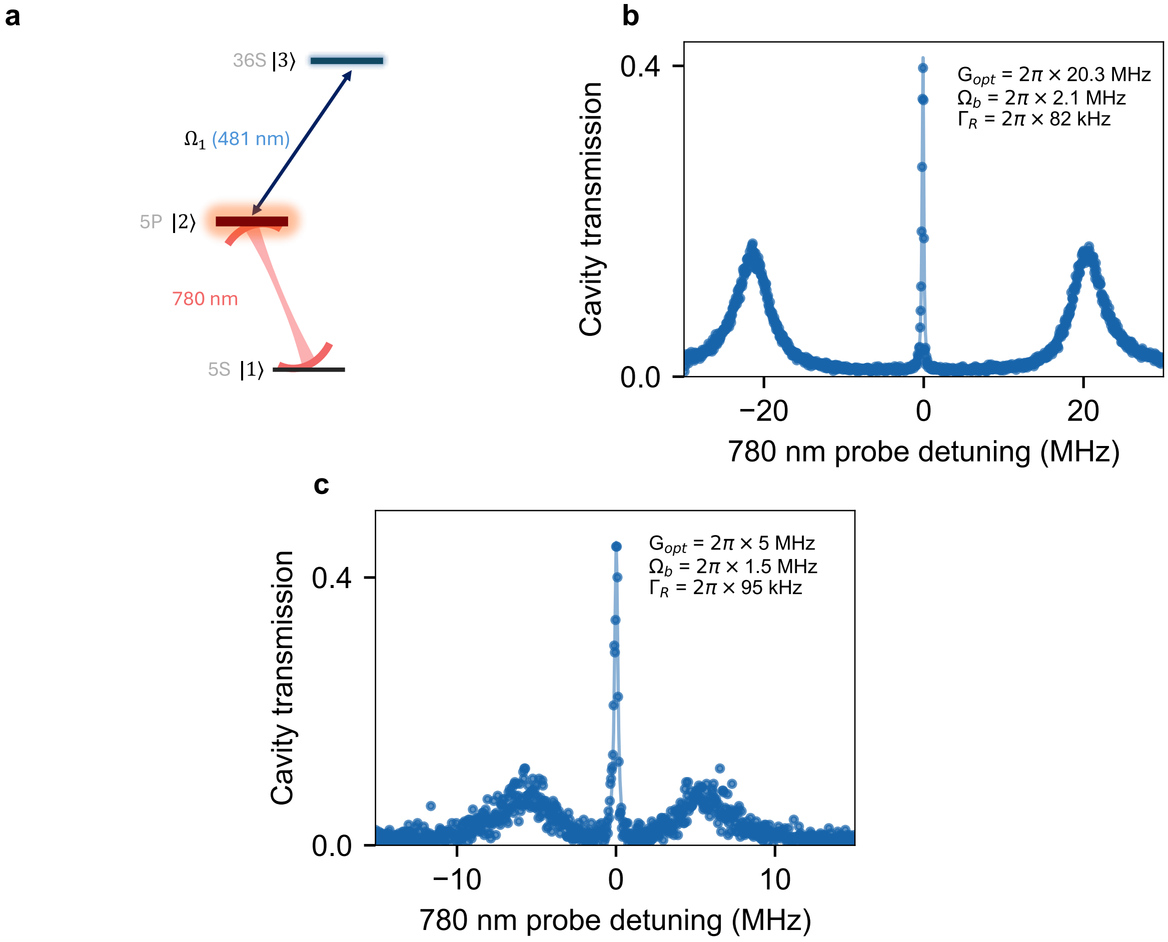

Figure 3.4: Cavity Rydberg EIT. (a) A strong coherent drive at 481 nm is introduced to couple to the 36S Rydberg level. At two-photon resonance (cavity resonance frequency and 481 nm drive), the spectrum exhibits three features corresponding to the three eigenstates of the system with a central narrow feature (the 'dark' polariton). The dark polariton is narrow because it has no contribution from the broad intermediate 5P state. Fitting the spectrum to a closed form solution allows us to extract the 481 nm Rabi frequency (Ω_1) and the inferred linewidth of the collective Rydberg state (Γ_R). The latter includes contributions from both the bare linewidth of the 36S state, and dephasing terms introduced from sources such as the drive laser and the Doppler broadening due to finite cloud temperature. (c) Typical operating point for the transducer scheme.

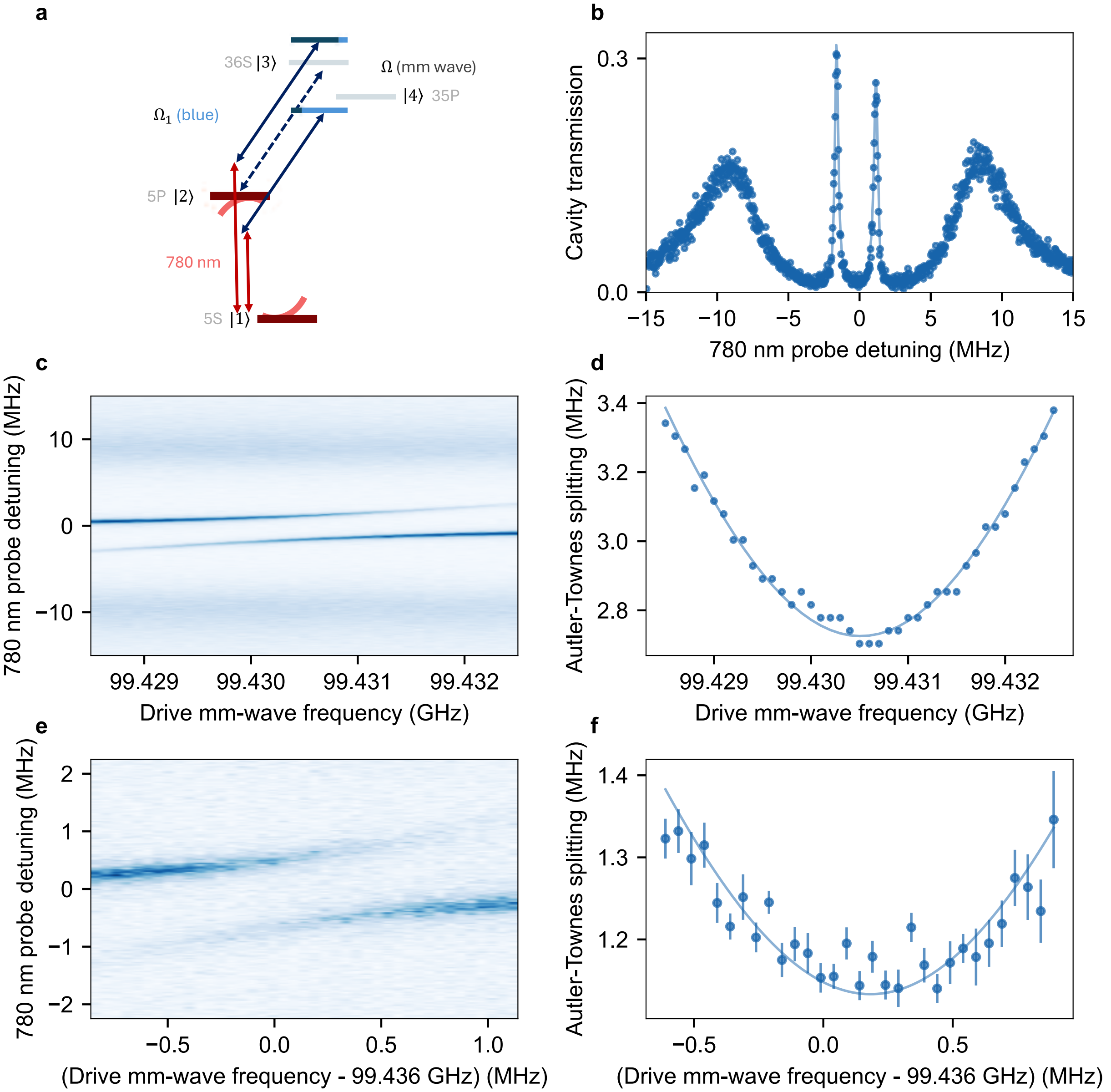

Figure 3.5: Autler-Townes splitting of dark polariton due to strong classical millimeter-wave drive. (a) The system shown in Figure 3.4 is driven by a strong millimeter-wave drive with a frequency that is around the 35P → 36S atomic transition frequency. This leads to a splitting in the EIT spectrum as shown in (b). As the frequency of the millimeter-wave drive is swept across the atomic resonance, the contribution of the 36S state in the coupled eigenstates varies, as exhibited by the avoided crossing diagram in (c). (d) The exact millimeter-wave atomic resonance frequency can be extracted from the minimum splitting between the two eigenstates. This data was taken with the $|5P_{3/2}, F = 4, m_F = 4\rangle$ state. (e), (f) Characterization for the transducer levels and fields. The data is taken at low probe powers to not heat the atoms away. The bright polariton features are not shown in (e).

3.5.3 Finding millimeter-wave transition frequency of atoms via Autler-Townes splitting of the EIT peak

In the presence of a strong resonant millimeter-wave drive, the 36S Rydberg state hybridizes with the 35P Rydberg state, producing an Autler-Townes splitting that yields two distinct two-photon resonances in the EIT spectrum. By scanning the millimeter-wave frequency, we observe the avoided crossing shown in Fig. 3.5, providing the atomic transition frequency of $\sim$ 99.436 GHz. The superconducting science cavity mode is away from resonance with this transition by around $\sim 2\pi \times 12$ MHz for this measurement to make its influence on the splitting is negligible. The strong coherent millimeter-wave drive is forced through the off-resonant cavity mode.

3.5.4 Tuning the millimeter-wave atomic transition frequency

For optimizing interconversion, control over Δ, the detuning of the atomic transition from the millimeter-wave cavity mode is required to control G_{mm}. It is nontrivial to tune the millimeter-wave cavity towards or away from resonance with the atomic millimeter-wave transition. The millimeter-wave cavity is designed and machined for a few GHz higher than the transition, and then coarsely tuned closed to the atomic resonance by first chemical etching [51], and then mechanical squeezing using a hydraulic press. After cooldown, the cavity was measured to be about 6 MHz detuned from the atomic transition in the absence of a magnetic field. For approaching resonance, instead of tuning the cavity, we Stark-shift the atomic transition (specifically, states $35\mathrm{P}_{1/2}$ and $36\mathrm{S}_{1/2}$) into resonance with the millimeter-wave cavity.

The superconducting spacer cavity is designed to have an additional “tuning” mode at 101.3 GHz which is $\sim$2 GHz away from the 35P to 36S atomic transition. We drive this mode to Stark-shift (Figure 3.6) the atomic transition into resonance with the main “science”

---

extracted from the mean and variance of the measurement [55].

mode of the cavity.

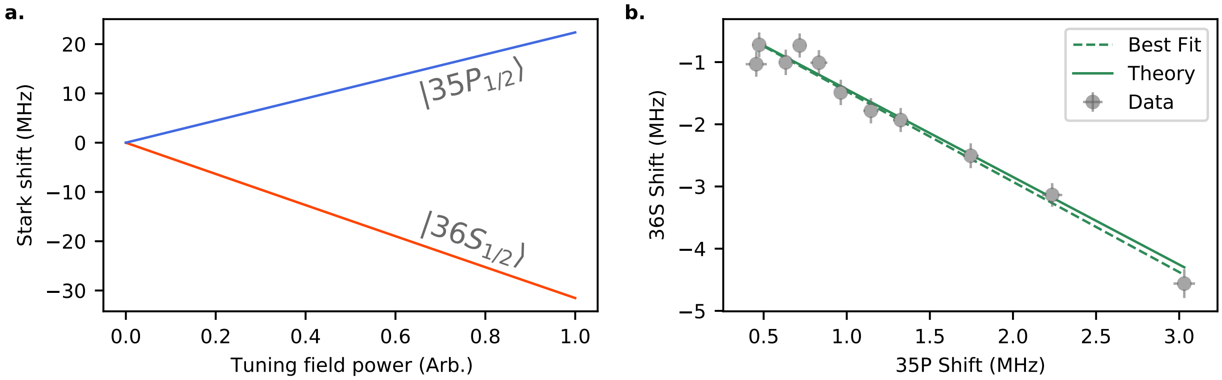

Figure 3.6: Stark tuning of the atomic Rydberg states. (a) The calculated ac Stark shifts of the $36S_{1/2}$ and $35P_{1/2}$ states as the power in the 101.318 GHz *tuning* mode of the cavity is increased. (b) As we vary the classical drive on tuning mode, we measure the shifts of the $36S_{1/2}$ and $35P_{1/2}$ states using cavity Rydberg EIT and direct UV spectroscopy from the $5S_{1/2}$ state (figures 3.8 and 3.13), respectively. This calibration then allows us to infer the $35P_{1/2}$ shift directly from the $36S_{1/2}$ shift measured via cavity Rydberg EIT.

3.5.4.1 Purcell-like broadening of the EIT peak

The measurement of the atomic transition frequency from the Autler-Townes splitting gives us precise information about the detuning from the millimeter-wave cavity. When we tune the atoms closer to the cavity frequency using the tuning mode, we observe that the dark-polariton peak gets broadened (Figure 3.7), signalling added loss to the 36S Rydberg state via the millimeter-wave cavity/transition strengthened by the cavity vacuum and thermal photon population.

Figure 3.7a highlights the difference between the same measurement taken on two different millimeter-wave cavities. The quadratic increase happens due to inhomogeneous broadening of the EIT peak due to spatial non-uniformity of the auxiliary mode across the atom cloud. Atoms at different positions in the auxiliary mode are Stark-shifted different amounts.

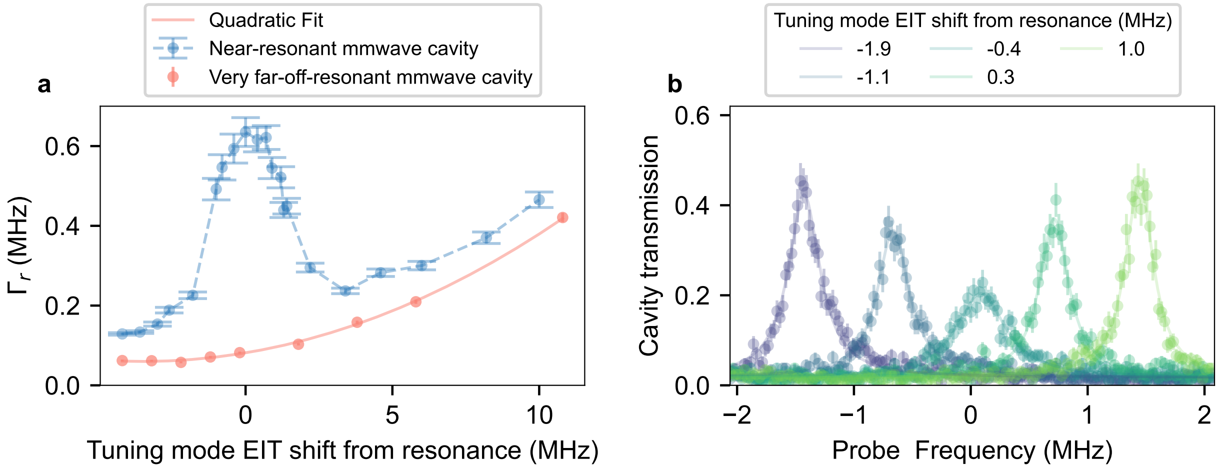

Figure 3.7: Broadening of the dark polariton feature as the millimeter-wave atomic transition is Stark-shifted into resonance with the millimeter-wave cavity (a) Linewidth of the collective 36S state as a function of the Stark-shift of the atomic transition using the tuning mode. Comparison with an older cavity designed to be far off-resonant from the atomic transition with the near-resonant cavity. The quadratic increase is due to the inhomogeneous spread of the Stark-shifts across the atomic cloud. (b) Dark polariton features at different atom-cavity detunings for the transducer's levels and optimized fields, different from (a).

3.5.5 Calibrating millimeter-wave photon number via Stark-shift of the EIT resonance

To measure the conversion efficiency, we require a measure of the number of millimeter-wave photons at the cavity input. However, we do not have the means to measure the attenuation of the millimeter-wave drive as it traverses through the room-temperature-cryo barrier to the cavity. We instead calibrate our drive by measuring the dispersive Stark-shift of the EIT peak (36S state) and extracting the mean *intracavity* photon number.

The external millimeter-wave drive power is stabilized via feedback to a voltage controlled attenuator. Fig.3.8a shows the shift of the EIT feature, which increases with increasing millimeter-wave drive power at the science cavity mode frequency. The measurement is taken when the millimeter-wave atomic transition is $\Delta = 2\pi \times 1.4$ MHz detuned from the cavity using the tuning mode. The reference EIT is taken by turning off the millimeter-wave source (orange curve), which already accounts for the effect of the cavity vacuum and thermal photons.

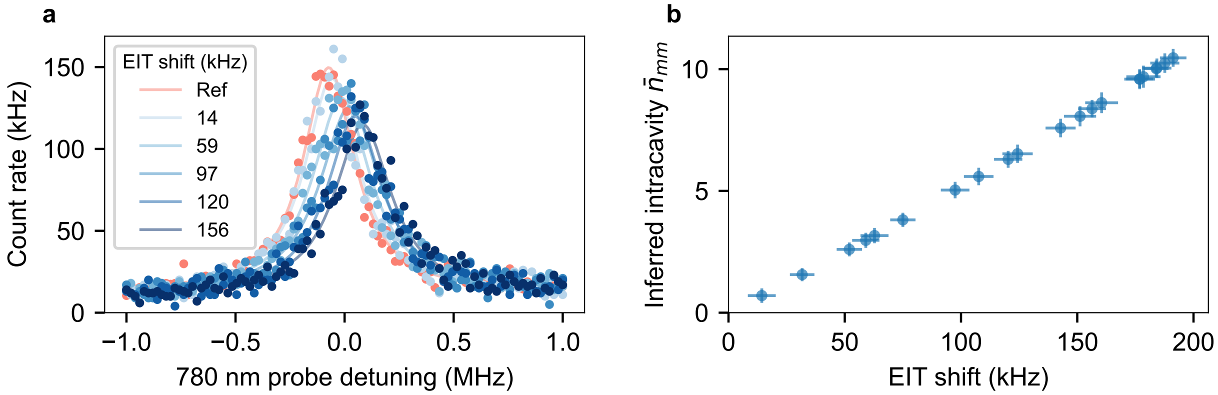

Figure 3.8: Calibration of intracavity millimeter-wave photon number via shift of the EIT peak. (a) Presence of millimeter-wave cavity photons shifts the 36S state energy, changing the two-photon resonance condition for the 780 nm cavity and the blue drive frequency. At fixed blue frequency, this change manifests as a shift of the EIT peak as a function of the probe frequency and the drive strength. The reference spectrum, with no external millimeter-wave input is shown in orange. The peak shifts increase with increasing millimeter-wave drive strength. (b) Extracted mean number of intracavity millimeter-wave photons from the EIT shifts (details in text). The interconversion results shown in the next chapter were typically performed at $\bar{n}_{mm} \sim 2$.

The functional form of the shift is evaluated from the near-zero eigenenergy $E_0(n'_{mm})$ of the Hamiltonian corresponding to dark polariton energy

$$H(n'_{mm}) = \begin{bmatrix} 0 & G_{opt} & 0 & 0 \\ G_{opt} & 0 & \Omega_b & 0 \\ 0 & \Omega_b & 0 & \sqrt{n'_{mm}+1}g_{mm} \\ 0 & 0 & \sqrt{n'_{mm}+1}g_{mm} & \Delta \end{bmatrix} \tag{3.13}$$

The measured shift corresponds to $E_0(n_{mm} + n_{th}) - E_0(n_{th})$, where n_{th} is set to 0.6 corresponding to the thermal population. This helps us infer the intracavity millimeter-wave photon number as shown in figure 3.8b.

To verify that we were not seeing background at the ‘science’ mode due to a high power drive at an auxiliary 'tuning' mode of the millimeter-wave cavity at 101 GHz 3.5.4, we deployed room temperature aluminum filter cavities [52] to suppress any tails or sidebands at the science frequency for comparison. We did not observe any effect of the 101 GHz tuning drive. This step was also crucial for noise characterization of the transducer.

3.5.6 Cavity linewidths

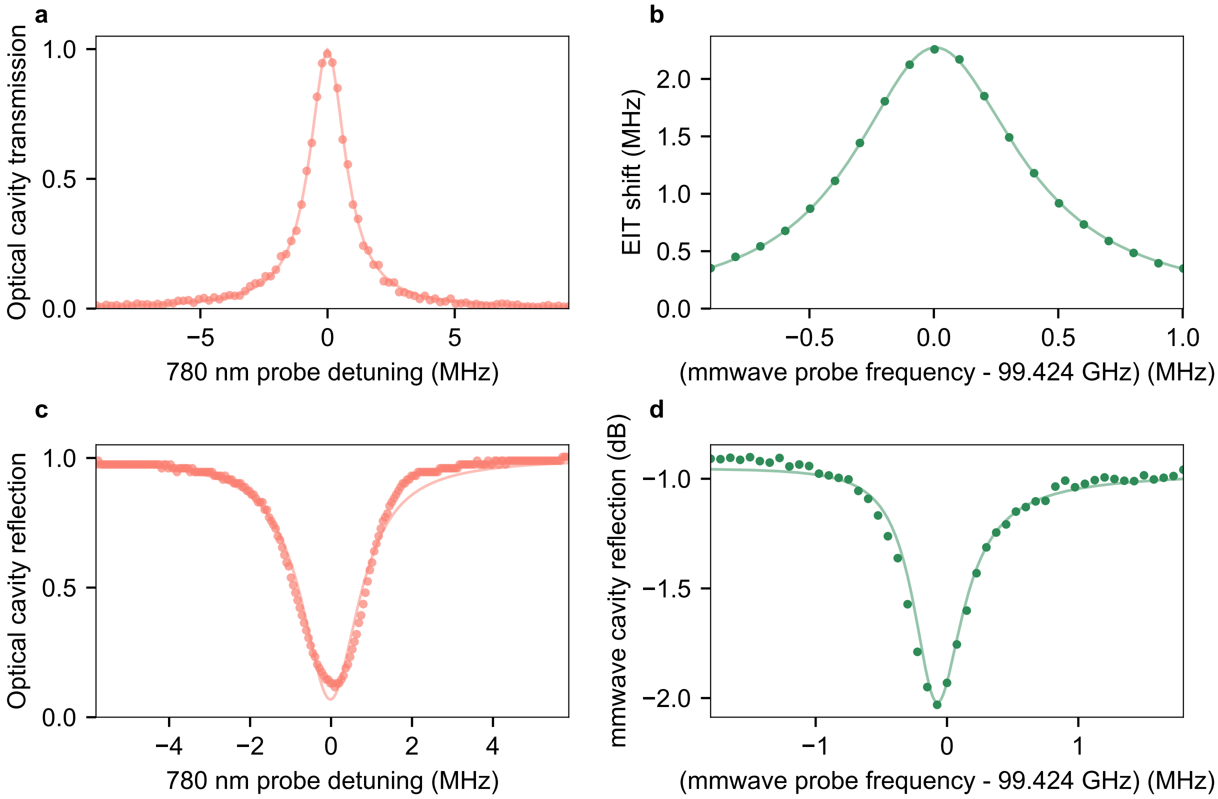

Figure 3.9: Methods for optical and millimeter-wave cavity external and total linewidth characterization. (a), (c) Transmission and reflection for the optical cavity as the 780 nm probe frequency is scanned. (b) The shift in the position of the EIT peak as the millimeter-wave probe frequency is scanned. Since the shift is proportional to the millimeter-wave drive strength (Figure 3.8), this data provides us information about the linewidth of the millimeter-wave cavity. (d) Reflection measurement from the millimeter-wave cavity using the circuit shown in figure 3.10.

Both internal and external cavity linewidths play a role in determining the conversion efficiency 3.6. The optical cavity is designed to be approximately single-ended to maximize

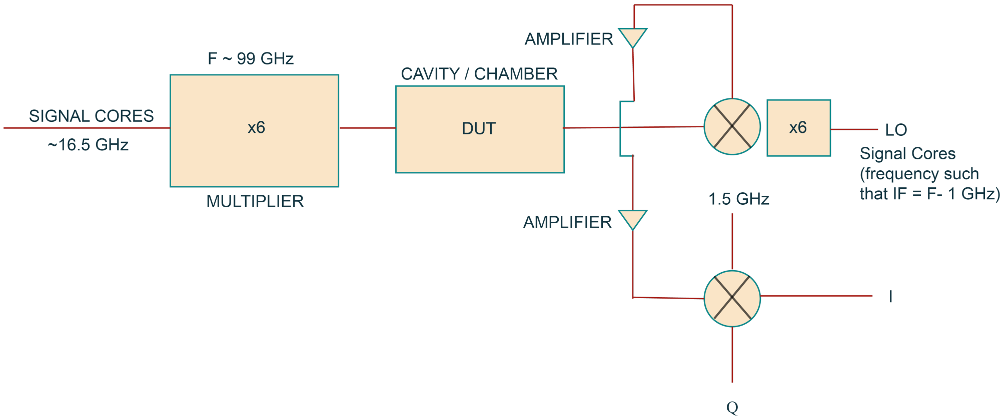

Figure 3.10: Millimeter-wave cavity measurement circuit. We measure the in-phase (I) and quadrature (Q) components of the reflection from the cavity (DUT) on a network analyzer and extract the amplitude and phase from the data. The reflection is obtained via a directional coupler at the input of the cavity (not shown in the schematic).

collection of converted photons[7]. After cooldown, the in-cryo total and external linewidths for the optical cavity were measured to be $2\pi \times 1.71(4)$ MHz and $2\pi \times 1.07(3)$ MHz via transmission and reflection measurements respectively (Figure 3.9). The transmission measurement provides the total linewidth from the full-width half maximum of the Lorentzian profile, and the reflection spectrum provides the internal to external linewidth ratio since the minimum reflection point is $(1 - 2\kappa_{\text{opt}}^{\text{ext}}/\kappa_{\text{opt}})^2$ (Chapter 2).

The internal millimeter-wave cavity linewidth is dependent on factors such as temperature of and impurities within the superconducting cavity. The coupling linewidth is determined by the length and diameter of the tubes. We measure the total linewidth by measuring the shift of the EIT peak as the millimeter-wave drive's frequency is swept (Figure 3.10). The coupling linewidth is extracted from the fit to a reflection measurement (Figure 3.9). To measure the reflection from the cavity, we use a Keysight PNA-X Network Analyzer N5242A using the circuit shown in Figure 3.10. In principle, we simultaneously measure the amplitude and phase of the reflected signal, obtaining enough information about the cavity to extract both the linewidths from the fits. The EIT shift measurement is a more direct

---

[7] The end mirrors were coated for R>99.995% and R=99.88% at 780 nm.

measurement of the total linewidth. The total and external linewidths are $2\pi \times 805(5)$ kHz and $2\pi \times 55(5)$ kHz respectively at 5K.

3.5.7 Millimeter-wave cavity coupling strength g_{mm}

Given the classical millimeter-wave mode-field distribution $E_{mode}(r)$ and the atomic dipole moment μ for the millimeter-wave transition, we calculate g_{mm} at the position of the atoms r_0 to be $2\pi \times 182$ kHz from the expression

$$g_{mm} = \frac{1}{\hbar}\vec{\mu} \cdot \vec{E}_{1ph}(\vec{r_0}) = \frac{\mu E_{mode}(r_0)/\sqrt{2}}{\hbar} \sqrt{\frac{\hbar\omega}{2\epsilon_0 \int_V \left|\vec{E}_{mode}(r')\right|^2 d^3r'}} \tag{3.14}$$

where $\vec{\mu}\cdot\vec{E}_{1ph}(\vec{r_0})$ is the quantized single-photon electric field at r_0 calculated by normalizing the classical field. The $\sqrt{2}$ factor for the field appears because for our choice of quantization axis, the millimeter-wave mode is lin-polarized and the atomic transition of interest is σ^- polarized. We simulate the electric field profile of the millimeter-wave cavity mode using the ANSYS HFSS software and obtain the dipole matrix element corresponding to the $|35P_{1/2}, J = 1/2, m_J = -1/2\rangle \rightarrow |35S_{1/2}, J = 1/2, m_J = 1/2\rangle$ transition using `arc`.

3.6 Integrating the 297 nm UV laser

As mentioned in the introduction, we need an additional 297 nm pump laser for energy and momentum conservation in the interconversion cycle, such that all atoms come back to the initial state and there's minimal leakage of quantum coherence through the atoms. The following sections describe the integration of the drive with the experiment.

3.6.1 UV induced optical damage

We tested for the effect of continuous UV irradiation of about 200 mW on an out-of-vacuum cavity with a finesse of 9000 and saw no degrading effects. In contrast, the effects on the science cavity even with <100 mW in cryo-vacuum were significant. Even with the FHG stage of the laser unlocked, the finesse was observed to degrade by a factor of 3 because of a few 100 microseconds of UV exposure, and recover slowly over the course of a few minutes after the UV input was blocked. With the FHG stage locked, the cavity resonance moves by >10× the cavity linewidth, accompanied with a degradation in finesse, destabilizing the 1560 nm lock as well.

Interestingly, turning on the blue laser helps recover the cavity finesse almost instantaneously for temporary damages induced by lower UV powers. For all our experiments with UV, we kept the blue laser on for most stages that do not interfere with other parts of the experiment. Figure 3.11 shows the effect of the UV beam on the cavity transmission with blue recovery on. At higher powers and longer hold times, the effect of UV is still visible.

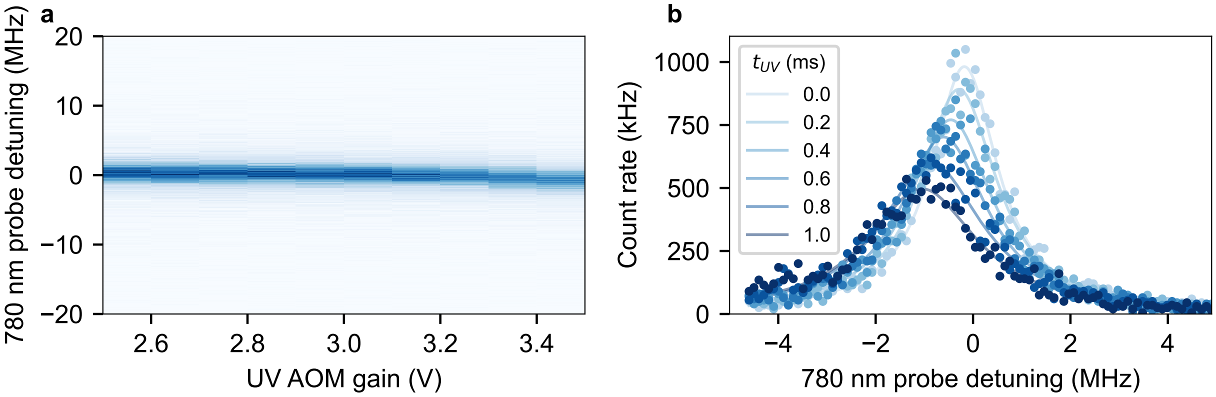

Figure 3.11: Damaging effect of the 297 nm laser on bare optical cavity transmission with blue recovery on (in the absence of atoms). (a) The resonance frequency of the optical cavity shifts as the UV power is increased (the x-axis represents the voltage to the AOM controlling the UV power incident on the chamber and is monotonically increasing in power) (b) Effect on cavity transmission as the on-time of the UV is increased. To limit the damage, we run short cycles of UV.

3.6.2 Phase matching

For closing the interconversion cycle, in addition to energy conservation (ensured by wavelength of the beams) and angular momentum conservation (ensured by polarization of the beams), linear momentum conservation is equally critical: $\Delta k = \vec{k}_{UV} + \vec{k}_{mm} - \vec{k}_{blue} - \vec{k}_{opt} = 0$. In the absence of phase-matching, i.e., when $2\pi/\Delta k < L_c$, where L_c is the length of the atomic cloud, converted light from different parts of the cloud carries different phases, leading to lower overall conversion efficiency due to destructive interference than obtained if the conversion was coherent throughout the cloud.

Since $\vec{k}_{mm}$ is negligible because of large wavelength of millimeter-wave with respect to the size of the atomic cloud, we can reduce the phase matching requirement to

$$\vec{k}_{UV} = \vec{k}_{blue} + \vec{k}_{opt} \tag{3.15}$$

In our experiment, due to accidental mirror damage due to long high power UV exposure (on the back surface, so the optical finesse was not affected) we could not send in the blue and UV collinear to cavity axis, and had to offset the blue beam by ~6 degrees. This required a different angle of incidence for the UV such that $k_{blue} \sin\theta_{blue} = k_{UV} \sin\theta_{UV}$. The phase coherence rapidly deteriorates in the radial direction away from this condition due to sinusoidal dependence on the angles of incidence.

3.6.3 Probing coupling of 297 nm drive with atoms via cavity

When impinged by UV light resonant with the 5S → $35P_{1/2}$ or $35P_{3/2}$ transition, atoms are removed from the 5S state. We can measure this decrease in population via coupling of the optical cavity to the atoms as shown in figures 3.12a and b. This measurement requires a two-dimensional scan. If we detune the cavity from the 5S-5P transition, we can instead measure the dispersive shift (figure 3.12c) which approximately goes linearly with N, the number of atoms. We park the probe on the linear side of slope of the dispersive peak to observe the effect of the UV beam more directly. This method allows us to do single-shot UV spectroscopy through the cavity (figure 3.12d and section 3.6.4), estimate Rydberg state lifetime (section 3.6.5) and observe Rabi flopping (section 3.6.6).

3.6.4 Single-shot UV transition spectroscopy via cavity transmission

We perform external vapor cell spectroscopy with the 297 nm laser (Appendix A.5) to find the correct wavelength for the 5S → 35P transitions. For the main experiment however, the exact frequency depends on magnetic fields and requires more precise spectroscopy on the intracavity atoms. We do this measurement using the dispersive shift measurement described in the previous section. We scan the frequency of the input UV beam and at resonance, expect to see the transmission change as atoms are removed from the ground state. Figures 3.12d and 3.13a show the spectroscopy for the $35P_{3/2}$ states and the $35P_{1/2}$ states respectively.

Scanning the UV frequency: we lock a frequency sideband of the carrier of the 1188 nm laser seed of the 297 nm laser to a stable reference cavity which is coresonant with the 780 nm probe laser and the 481 nm EIT laser. To sweep the frequency of the UV beam at the cavity (which is 4 times the frequency of the seed), we sweep the sideband frequency such that the sideband remains referenced to the stable cavity while the carrier frequency changes. The frequencies on the x-axis in the spectroscopy plots refer to this EOM sideband frequency. In the presence of an external millimeter-wave drive, we can also look at the Stark-shift and Autler-Townes splitting of the Rydberg states via UV spectroscopy (figure 3.13). These measurements help us calibrate the detuning of the atomic transition from the millimeter-wave cavity (section 3.5.4).

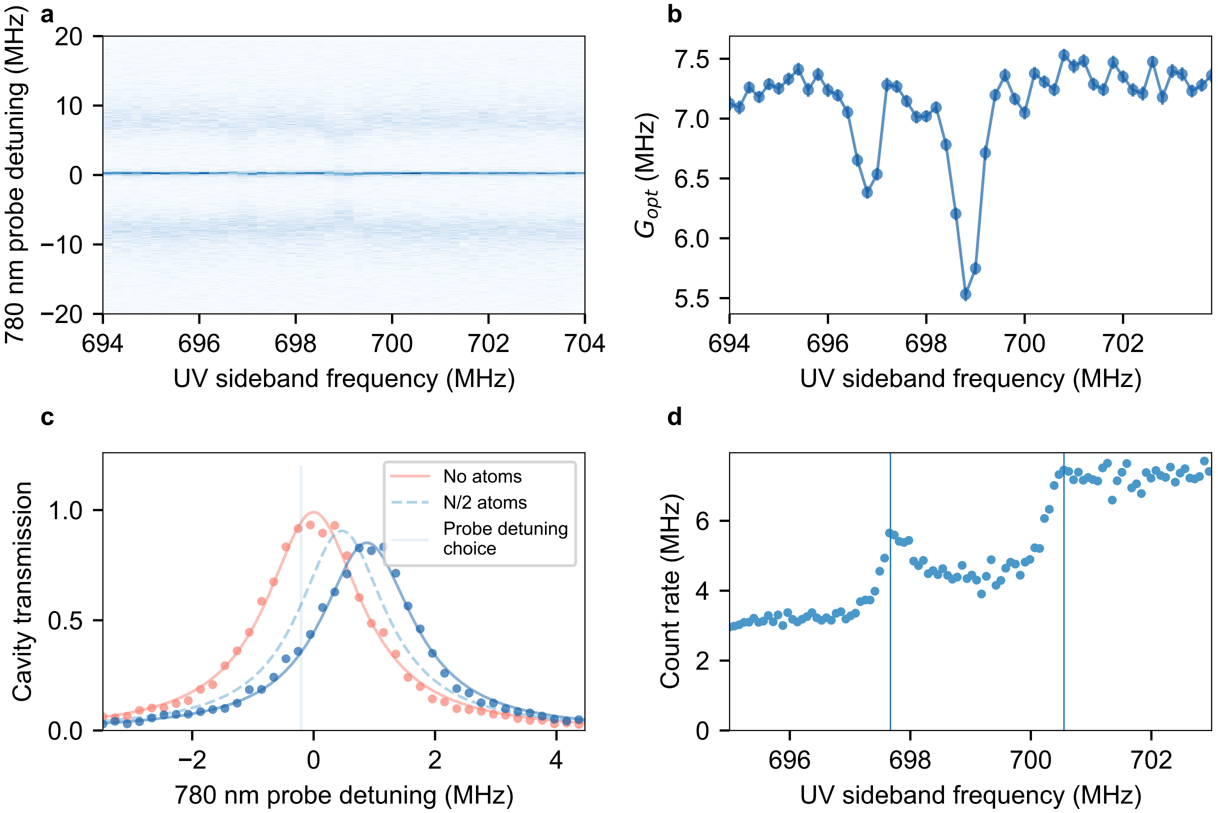

Figure 3.12: Single-shot spectroscopy of the 5S → 35P transition (a) Cavity EIT spectrum as a function of UV drive frequency. The number of atoms in the ground state falls when the UV is resonant with the 5S → 36S transition, leading to a decrease in G_{opt}, as seen in (a) and the fitted G_{opt} values from (a) shown in (b). The detail about the sideband frequency on the x-axis is discussed in section 3.6.4. (c) In place of the 2D scan, we can operate in the dispersive regime when the optical cavity is detuned from the 5S → 5P transition. The cavity spectrum shifts with varying atom number, leading to a change in the transmission at a fixed 780 nm probe frequency. (d) We park the probe at a particular frequency on the side of the transmission spectrum and observe the change in transmission as the UV frequency is scanned. The two peaks correspond to $35P_{3/2}, m_j = 3/2(m_F = 4)$ and $-1/2(m_F = 2)$ (based on the linear polarization of the incident UV laser which should couple to these two states). The latter state would couple to other m_F states in the ground state, which is likely manifesting as atom loss in the right peak (as the cavity transmission is not recovered). The x-axis translation compared to (b) is primarily due to change in locking conditions. The splitting can also give an estimate of the internal field strength, in this case about 2.1322 G.

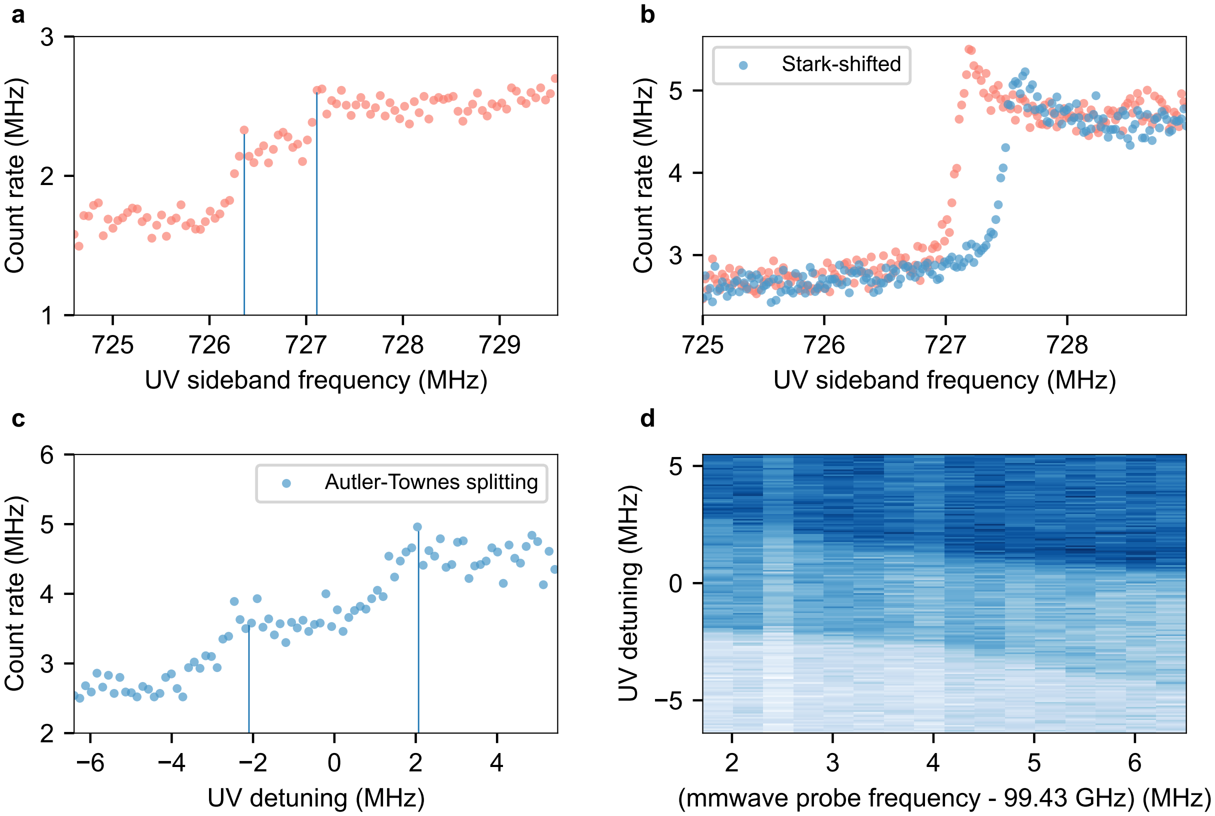

Figure 3.13: Autler-Townes splitting of the 35P state. (a) Spectroscopy for the $35P_{1/2}, m_J = 1/2$ and $-1/2$ states (the magnetic fields were changed between data shown in figure 3.12d and this data). (b), orange, We change the polarization to focus on one of the $35P_{1/2}$ states. blue, Stark-shifting of the state is observed when a millimeter-wave drive detuned from the 35P → 36S transition is turned on. (c) Autler-Townes splitting of the 35P state with a millimeter-wave drive that is resonant with the atomic transition. (d) Autler-Townes splitting as the millimeter-wave drive frequency is scanned around the atomic resonance.

3.6.5 An estimate of 35P state lifetime

An indirect measurement of the $35P_{3/2}$ state lifetime is shown in figure 3.14a. We turn on the UV drive after optically pumping the atomic sample and before the probe stage, which leads to an initial decay in population (hence increase in cavity transmission approximately proportional to the atom number). However, soon we see an increase in the ground state atom population (when the transmission decreases) with the inferred mean decay time of 72 microseconds. The `arc` predicted lifetime for the $35P_{3/2}$ state at 5 K is 83 microseconds. The transmission likely increases later due to heating of atoms from the 780 nm probe. Note that for interconversion, we worked with the $35P_{1/2}$ state and the state lifetime was inconsequential as we operated in the detuned limit. Figure 3.14b shows the population at the parameters we operate at.

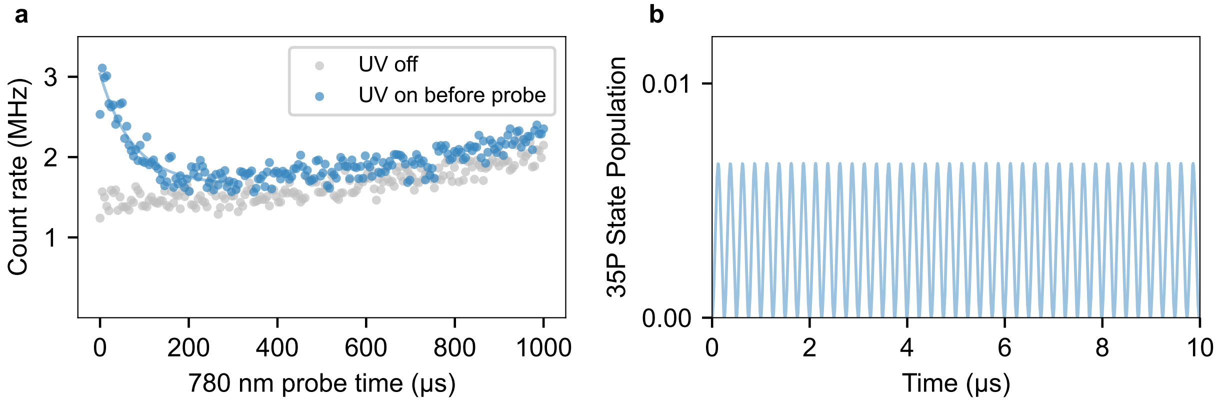

Figure 3.14: Estimate of 35P state lifetime. The resonant UV drive is turned on before the 780 nm probe to excite the ground state atoms to the 35P state and is turned off when the probing period begins. The decay in the excited state population leads to an increase in the ground state population which decreases the cavity transmission and provides an estimate of the $35P_{3/2}$ state lifetime. The later increase in transmission is due to heating of the atoms from the 780 nm probe. (b) 35P Rydberg dressing of the ground state. Only a very small fraction of the ground state population is in the 35P state at any instant for interconversion.

3.6.6 Rabi oscillations between ground state and Rydberg state

We observe Rabi oscillations on the 5S-35P transition with the UV using the method described in 3.6.3 to measure the coupling strength of the UV drive Ω_{UV} as shown in figure 3.15a and b. If the probe frequency is set to correspond to the approximately linear region of the Lorentzian, the change in transmission scales approximately linearly with the atomic state population, giving a good estimation for day-to-day optimizations. Figure 3.15b shows the oscillation when converted to state population.

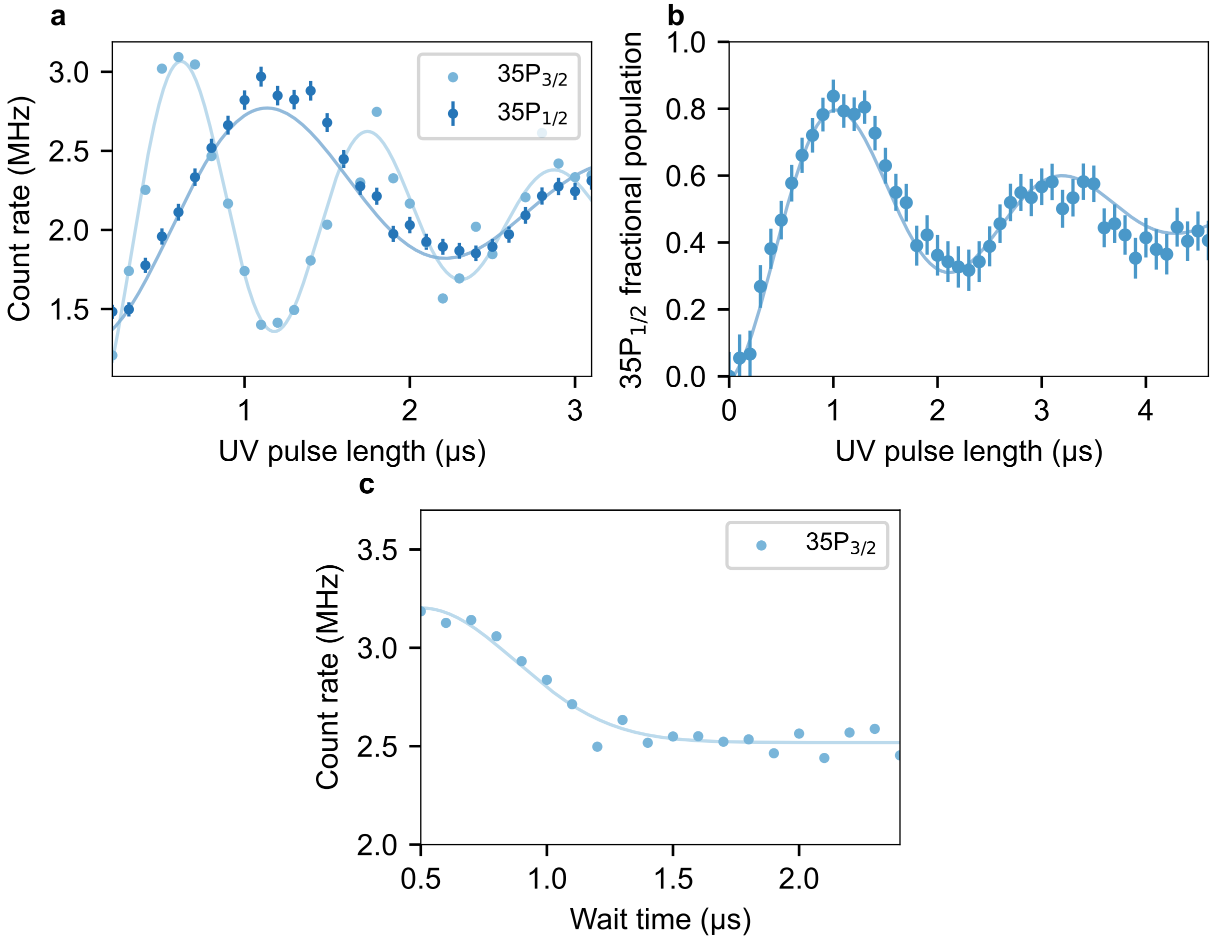

Figure 3.15: Resonant Rabi oscillations between 5S and 35P states, and a corresponding Ramsey measurement. (a) Rabi oscillations between the ground 5S and 35P Rydberg state. (b) Rabi oscillations for $35\mathrm{P}_{1/2}$ for the transducer (with count rate converted to atomic population) with Rabi frequency $\Omega_{UV} = 2\pi\times230$ kHz. (c) Ramsey measurement yielding a decoherence time of $T = 0.543\,\mu$s.

While we get more coupling strength (higher Rabi frequency) at $35\mathrm{P}_{3/2}$ transition due to a stronger matrix element, we have to operate at the $35\mathrm{P}_{1/2}$ transition to conserve angular momenta and complete the interconversion cycle. At the maximum available UV power, we can increase the Rabi frequency by making the waist smaller. However, in that case, we were limited by the inhomogeneous spread in Rabi frequency due to the comparable size of the atomic cloud (see numerics in Appendix A.3). We performed a Ramsey measurement and obtained the decoherence time $T = 0.543$ microseconds from a Gaussian fit of the form $e^{-(t/T)^2}$ (figure 3.15c). We expect Doppler broadening and UV frequency fluctuations to be limiting this time. It should be pointed out that the decoherence time did not limit us ultimately for interconversion as we were operating far from resonance.

3.6.6.1 Intracavity 785 nm lattice

To resolve the issue of inhomogeneous UV Rabi frequencies across the cloud, we tested if introducing an intracavity lattice can compress the cloud along one of the transverse directions. While we observed some improvement in the oscillation contrast, we were severely limited by fast noise on the laser that limited lifetime of atoms in the intracavity lattice. The observations are presented in Appendix A.4.

3.7 Increasing data rates

Initially, we were limited by photon shot noise at lower probe powers and not atom number fluctuations. We improved our data rate and hence statistics by doing multiple probes per shot, instead of probing with higher power (figure 3.16). The eventual limit to increasing data rates was heating from the probe.

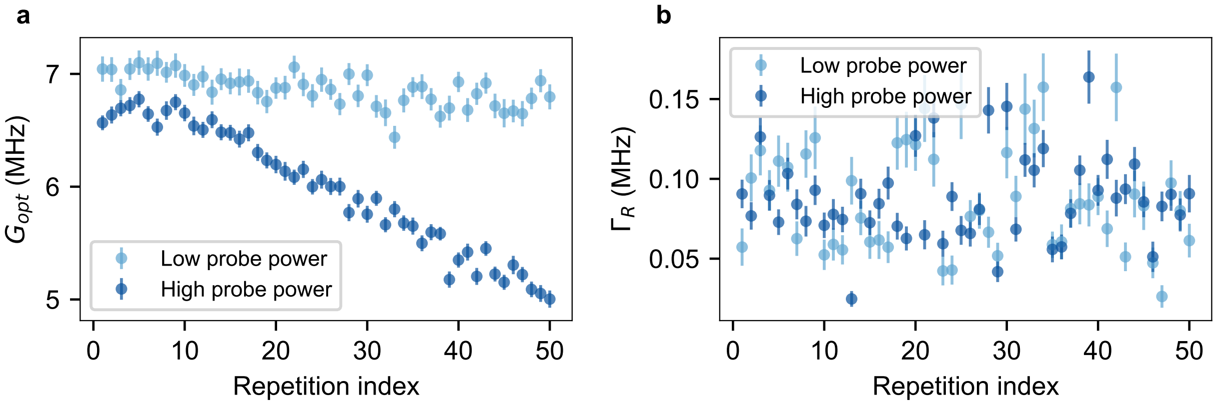

Figure 3.16: By optimizing initial optical pumping, we could probe for up to 50 ms at low probe powers without significantly heating or depumping atoms as evidenced by the measurements of g in (a) and the collective 36S Rydberg state linewidth from EIT in (b). Each individual probe cycle is 1 ms long for this data. Unless for quick optimizations, for a typical experimental sequence, we operate in the low probe power regime.

3.8 Optimizing optical pumping

To optimize fields inside the superconducting cavity for optical pumping, we heat the spacer to above Niobium's T_c to about 10K using an internal heating resistor that is thermally shorted to the cavity. This is because below T_c the external changes in B fields are not reflected inside the cavity because it is superconducting. We then optimize magnetic fields while maximizing atom-optical cavity coupling G_{opt} (Section 3.5.1) and minimizing collective Rydberg state linewidth Γ_R (Section 3.5.2). This step needs to be done with longer wait times to allow for ringing down of fields elsewhere in the chamber to simulate below T_c conditions when the fields are always stable (with respect to the intracavity atoms). We then turn off the current through heating resistor and cool the cavity back down to 5K while the fields are constantly on to 'freeze' these fields inside the superconducting cavity [52].

3.9 Single photon detection

We observe the output of the optical cavity through the mirror with 99.88% transmission. The output is split into two paths using a non-polarizing beam splitter, to be collected by two fiber-coupled single-photon counting modules (SPCM, Excelitas SPCM-AQRH-14-FC). The SPCMs generate a transistor-transistor logic (TTL) pulse at the incidence of a photon, which is time tagged using custom firmware on a field-programmable gate array (FPGA). The time resolution of tagging is about 10 ns, and later analyzed to calculate the total count rate and the temporal correlation function (discussed in next chapter).

To minimize background counts, we use dichroic mirrors to separate out the 297 nm, 481 nm and 1560 nm light. We also use two narrow 780 nm filters at the fiber coupling port to block any scattering from the 785 nm lattice light. It was critical for us to use a single-mode fiber to couple to the SPCM to not couple to background signal correlated with blue light (We speculate that the blue light generated fluorescence along the path at 780 nm which led to a strong background *at 780 nm* with a multimode fiber). We wrapped the fiber in black tape and coiled it into small circles to generate bending losses for other wavelengths. With these precautions, we measured a dark count rate of ~165 Hz (specifications: 34 Hz).

At higher count rates, it becomes critical to consider the nonlinearity of the SPCM. We used the calibration from the manufacturer for corrections. We also calibrate the photon detection efficiency (PDE) of the SPCM at 780 nm. For this, we first calibrate an absorptive filter using a CW diode at 780 nm and a calibrated Thorlabs power detector. We then use the power detector to measure power before the SPCM, and measure the filter attenuated signal at the SPCM, after accounting for nonlinearity correction factor. We measure an average PDE of 57.2%.

3.10 Extracting conversion efficiency from optical count rate measurement

We can currently only measure the intracavity millimeter-wave photon number through the shift of the dark polariton feature (section 3.5.5) and the rate of optical photons that are incident on a single photon counter after conversion and leakage through the optical cavity. The following calculations allow us to extract an internal conversion efficiency from the measured optical output, and later calculate the temporal correlation $g^{(2)}(\tau)$ function measurement predictions from theory.

We define unnormalized first-order correlation function for the output of the transducer:

$$\begin{aligned}\overline{g}^{(1)}(\tau) &= \langle a_{out}^{\dagger}(\tau) a_{out}(0)\rangle \\ &= \frac{1}{2\pi}\iint\limits_{-\infty}^{+\infty} S(\omega)^{*}S(\omega')\langle b_{in}^{\dagger}(\omega) b_{in}(\omega')\rangle e^{-i\omega\tau} d\omega d\omega'\end{aligned} \tag{3.16}$$

using the definition, $a_{out}(t) = \frac{1}{\sqrt{2\pi}}\int_{-\infty}^{\infty} a_{out}(\omega)e^{-i\omega t}d\omega$ and the transfer function $S(\omega)$ defined and derived in the previous chapter.

For our experiments the input field is a coherently displaced thermal field, which we write as

$$b_{in}(t) = \beta e^{-i\omega_D t} + b_{in}^{th}(t)$$

where $|\beta|^2$ is the mean photon flux of the coherent drive and ω_D is the detuning of the drive from the millimeter-wave cavity in the rotating frame. Taking a fourier transform, we get $b_{in}(\omega) = \sqrt{2\pi}\beta\delta(\omega - \omega_D)$. In the frequency space, we write:

$$b_{in}(\omega) = \sqrt{2\pi}\beta\delta(\omega - \omega_D) + b_{in}^{th}(\omega) \tag{3.17}$$

From equations 3.16 and 3.17, the rate at the output $\overline{g}^{(1)}(\tau)$ can be separated into two parts corresponding to the coherent drive ($\overline{g}^{(1)}_{coh}(\tau)$) and the thermal drive ($\overline{g}^{(1)}_{th}(\tau)$). This is because the cross-term between the drives averages to zero in the term $\langle b^{\dagger}_{in}(\omega) b_{in}(\omega') \rangle$ since $\langle b^{th}_{in}(\omega) \rangle = 0$ (Appendix A.6). For the coherent drive, Eq. 3.16 simplifies to:

$$\overline{g}^{(1)}_{coh}(\tau) = |\beta|^2 |S(\omega_D)|^2 e^{-i\omega_D \tau} \tag{3.18}$$

We want to relate β to our measured intracavity millimeter-wave photon number n_{ph}. From cavity evolution equations (Chapter 2), $b(\omega) = \frac{2\sqrt{\kappa^{ext}_{mm}}}{\kappa_{mm} - 2i\omega_D} \beta \delta(\omega - \omega_D)$. This allows us to go back to the expression for $b(t)$ and relate n_{ph} to β at resonance:

$$n_{ph} = \langle b^{\dagger}(t) b(t) \rangle = \frac{4|\beta|^2 \kappa^{ext}_{mm}}{\kappa^2_{mm}} \tag{3.19}$$

For a thermal input, $\langle {b^{th}_{in}}^{\dagger}(\omega) b^{th}_{in}(\omega') \rangle = n_{th} \delta(\omega - \omega')$ [61]. n_{th} is the number of thermal photons at frequency ω, which is assumed to be constant for the transduction bandwidth in our experiment. To evaluate $\overline{g}^{(1)}_{th}(\tau)$, it should be noted that the transfer function has to be evaluated with $\kappa^{ext}_{mm} = \kappa_{mm}$ because thermal photons couple from everywhere in the cavity in contrast to the coherent drive which couples in only at the input port:

$$\overline{g}^{(1)}_{th}(\tau) = \frac{n_{th}}{2\pi} \int_{-\infty}^{\infty} |S(\omega)|^2 \Big|_{\kappa^{ext}_{mm} = \kappa_{mm}} e^{-i\omega\tau} d\omega \tag{3.20}$$

We can thus write

$$\begin{aligned} \overline{g}^{(1)}(\tau) &= \overline{g}^{(1)}_{coh}(\tau) + \overline{g}^{(1)}_{th}(\tau) \\ &= \frac{n_{ph} \kappa^2_{mm}}{4\kappa^{ext}_{mm}} |S(\omega_D)|^2 e^{-i\omega_D \tau} + \frac{\kappa_{mm}}{\kappa^{ext}_{mm}} \frac{n_{th}}{2\pi} \int_{-\infty}^{\infty} |S(\omega)|^2 e^{-i\omega\tau} d\omega \end{aligned} \tag{3.21}$$

where the $\frac{\kappa_{mm}}{\kappa^{ext}_{mm}}$ factor in the second term allows us to use the input-port referenced transfer function $S(\omega)$ derived in the previous chapter.

The rate of the transduced optical photons at the photon detector is $R = R_{coh} + R_{th} =$

$f_o \overline{g}^{(1)}(0)$, where f_o is the optical path efficiency after the cavity (including the efficiency of the single photon counter). In terms of the measured quantities, the overall (ϵ) and internal (η) conversion efficiencies can be extracted as:

$$\epsilon_{mm\to o} = \frac{\langle a^\dagger_{out}(t) a_{out}(t)\rangle}{|\beta|^2} = \frac{1}{f_o}(R - R_{th})\frac{4\kappa^{ext}_{mm}}{\kappa^2_{mm} n_{ph}} \tag{3.22}$$

$$\eta_{mm\to o} = \frac{1}{f_o}(R - R_{th})\frac{4\kappa_{opt}}{\kappa^{ext}_{opt}\kappa_{mm} n_{ph}} \tag{3.23}$$

where R is the rate of photons measured at the single photon counter with the coherent drive, and R_{th} is the rate of photons measured when the interconverter is run without an external drive (so only thermal photons are converted). The error bars on the efficiency are calculated by propagating the errors in the individual quantities.

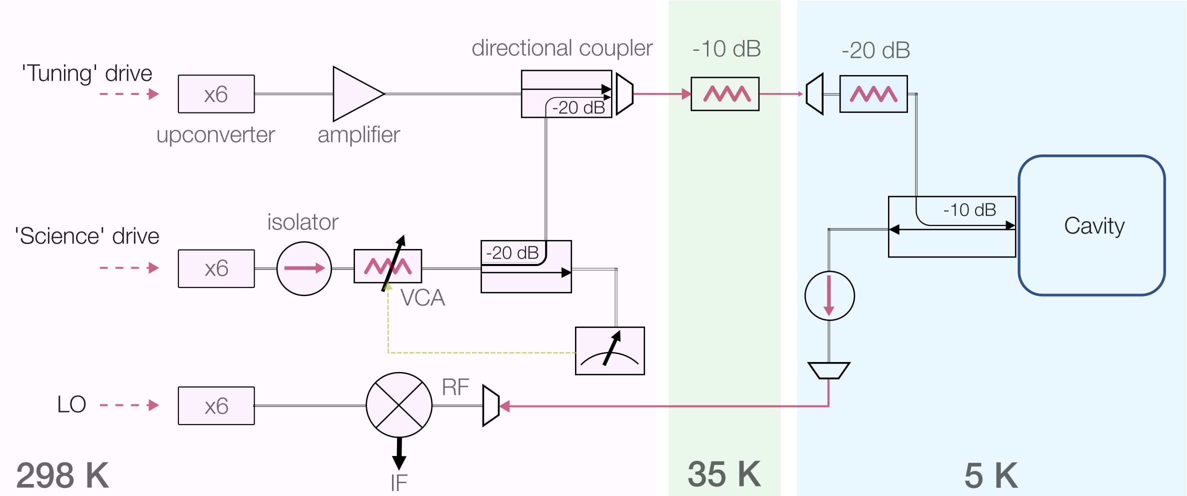

Figure 3.17: Millimeter-wave circuit used in the experiment.

Chapter 4

Millimeter-wave to Optical Transduction: Results

This chapter is based on reference [25].

With a good handle on the different aspects of the experiment and the theoretical model for conversion efficiency, we are now ready for interconversion. We freeze the optimal fields for the optical pumping scheme for interconversion (section 3.8) and do machine characterizations (section 3.5) following the processes detailed in the previous chapter to obtain the experimental parameters mentioned in Table 4.1.

We can change certain rates in the interconversion loop via the following 'tuning knobs' available in the experiment for impedance matching (section 3.4.2):

- Millimeter-wave tuning mode drive strength and frequency: controls the detuning of the atoms with the millimeter-wave cavity Δ, hence the dressing fraction of the ground state to the $35P_{1/2}$ via the UV drive. The dressing fraction in turn controls the collective cooperativities G_{mm} and G_{opt} at the millimeter-wave transition and optical 780 nm transitions. With UV dressing, the effective number of atoms in the ground 5S state is $N_g = N\cos^2\theta$ and Rydberg 35P state is $N_{mm} = N\sin^2\theta$, where $\tan\theta = \left|\frac{\Omega_{UV}}{\Delta}\right|$.

In the small dressing fraction limit that we operate at (~0.003, figure 3.14 in the previous chapter), the effect on the optical cooperativity is negligible. We operate at the maximum Ω_{UV} achievable in the system to be able to operate at the maximum Δ, constrained by the available UV laser power.

- Number of atoms loaded in the cavity N: also controls the collective cavity-atom cooperativities.
- Blue power: controls the generalized cooperativity C_b via Rabi frequency Ω_b. For optimal performance in our current setup, we operate at the maximum Ω_b achievable, constrained by the available blue laser power.

4.1 Conversion efficiency and bandwidth

Figure 4.1a shows the internal conversion efficiency and bandwidth (inset) of millimeter-wave photons to optical photons conversion as the atom-cavity detuning is scanned using the millimeter-wave tuning mode. At each point, we measure the conversion efficiency as a function of the millimeter-wave drive's detuning from the cavity (figure 4.1b) and extract the peak value and bandwidth (figure 4.1a inset) from Lorentzian fits to account for the offset in the measurement. We see a maximum efficiency of 58(11)% and bandwidth of 360(20) kHz when impedance matched, at $\Delta \approx 2\pi \times 4$ MHz. We typically operate at an input coherent drive corresponding to $n_{ph} \sim 2$. The end-to-end conversion efficiency is estimated to be about 2.5% based on our measurement of external cavity linewidths. The solid curves in the plots are theory curves obtained by using parameters derived from the characterizations discussed in the previous chapter.

Figure 4.2 shows the dependence of the conversion efficiency on the number of atoms in the cavity. The peak efficiency is when $N \approx N_g \sim 600$. The UV dressing fraction is $\sim$ 0.003, corresponding to about 1.8 mean number of atoms in the 35P Rydberg state in steady

Parameter	**Symbol**	**Value**
Millimeter-wave cavity "science" mode frequency	–	$2\pi \times 99.42376(1)$ GHz
Millimeter-wave cavity "tuning" mode frequency	–	$2\pi \times 101.318$ GHz
$35P_{1/2} \leftrightarrow 36S_{1/2}$ transition frequency without stark tuning	–	$2\pi \times 99.436$ GHz
Single atom-optical cavity coupling	g_{opt}	$2\pi \times 206$ kHz
Optical cavity linewidth	κ_{opt}	$2\pi \times 1.71(4)$ MHz
Out-coupling rate of the measurement optical cavity port	κ_{opt}^{ext}	$2\pi \times 1.07(3)$ MHz
Decay rate of the $5P_{3/2}$ state	Γ	$2\pi \times 6.065$ MHz
481 nm beam Rabi frequency	Ω_b	$2\pi \times 1.45(5)$ MHz
Decoherence rate of the $36S_{1/2}$ collective state	Γ_R	$2\pi \times 56(8)$ kHz
Single atom-millimeter-wave cavity coupling	g_{mm}	$2\pi \times 182$ kHz
Millimeter-wave cavity linewidth	κ_{mm}	$2\pi \times 805(5)$ kHz
Millimeter-wave cavity external coupling rate	κ_{mm}^{ext}	$2\pi \times 55(5)$ kHz
UV beam effective Rabi frequency	Ω_{UV}	$2\pi \times 230(3)$ kHz
Optical path efficiency including SPCM efficiency	f_o	0.28(2)

Table 4.1: Table of key experimental parameters for transduction

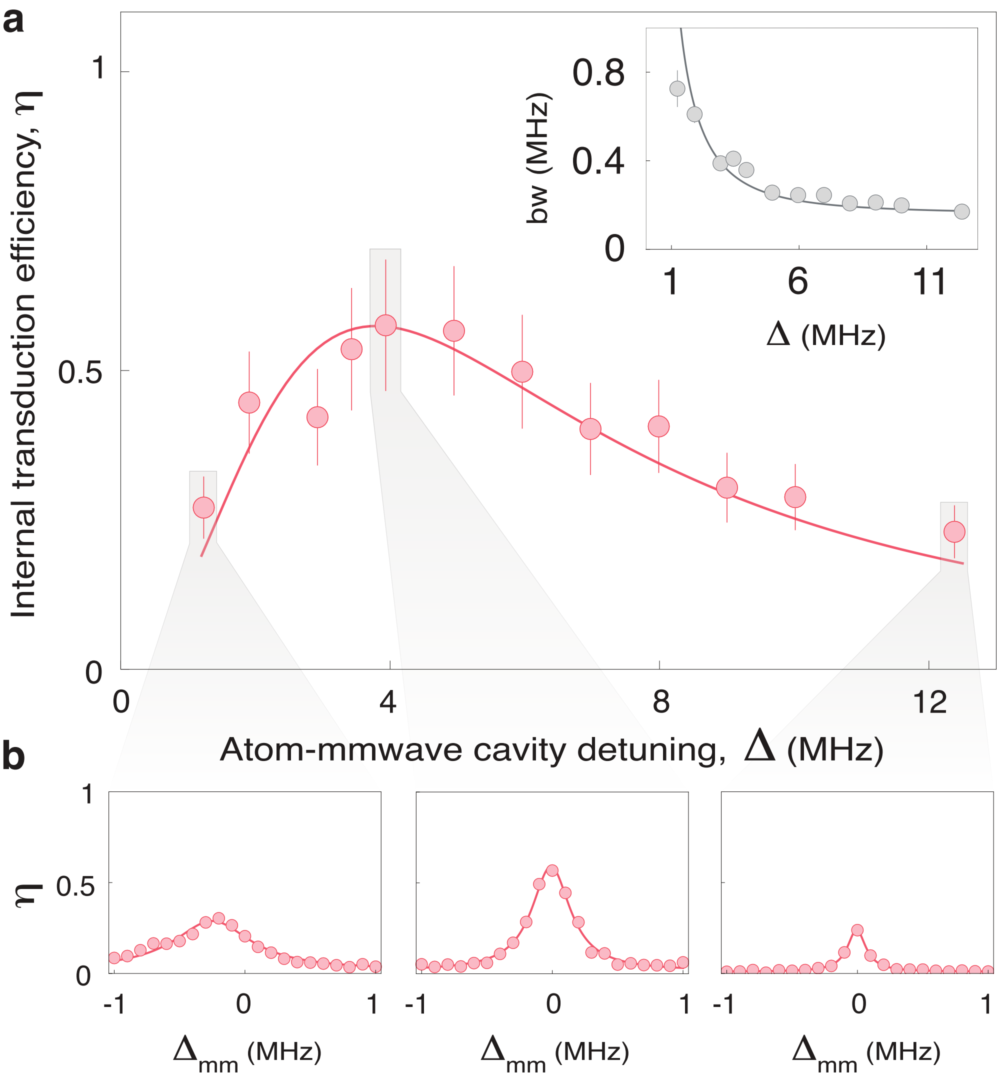

Figure 4.1: Internal conversion efficiency for millimeter-wave → optical conversion. (a) The internal conversion efficiency as the detuning Δ between the millimeter-wave cavity and the millimeter-wave atomic transition is scanned. The peak internal efficiency is measured to be 58(11)% with a corresponding external conversion efficiency of ∼2.5%. (b) For each point in (a), the millimeter-wave drive frequency is scanned. Δ_{mm} represents the detuning of the drive from the millimeter-wave cavity resonance. The spectra are fitted to a Lorentzian profile with an offset to extract the peak conversion efficiency. The FWHM of the fitted Lorentzian provides the bandwidth shown in the inset to (a). All solid curves are theory curves obtained by using parameters derived from the characterizations discussed in the previous chapter.

state, leading to a cooperative enhancement of the same magnitude on the millimeter-wave transition. Because of the UV detuning from the atomic transition, the atomic population in the Rydberg state is continuously refreshed at fast rates, making them available for the millimeter-wave conversion.

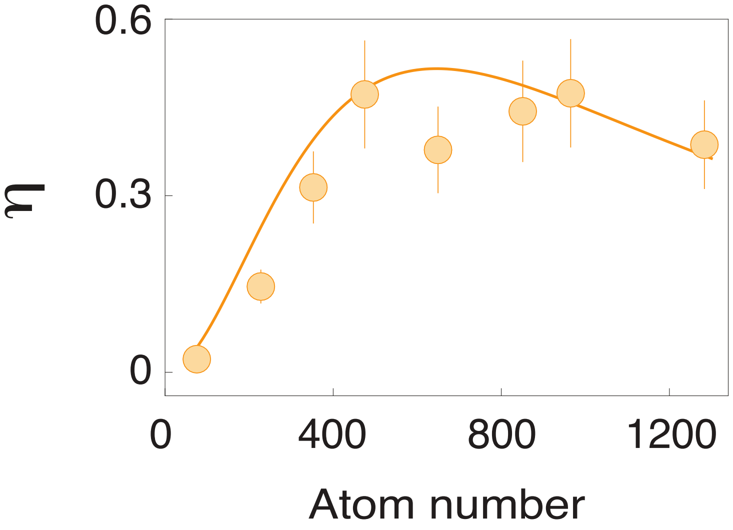

Figure 4.2: Dependence of conversion efficiency on atom number.

4.2 Added noise characterization

At 5K operating temperature, we expect the cavity to have 0.6 mean thermal photons. We characterize the added noise in the system by measuring the output of the optical cavity with no input millimeter-wave photons. Figure 4.3 shows the data for when we operate near the optimal impedance-matched point for conversion and measure the count rate of converted optical photons as a function of UV drive frequency with 1) no input (grey) and 2) a coherent drive with mean $n_{ph} = 0.55$ photons (green). Without the coherent drive, we observe a broad feature corresponding to the background thermal photons emitted by the broad millimeter-wave cavity. The feature becomes narrower with a stronger drive (while still including contribution from the thermal background). The asymmetry in both the features arises because lower Δ_{UV} is closer to the ground-Rydberg transition, which changes the interconverter's impedance matching condition away from the optimum.

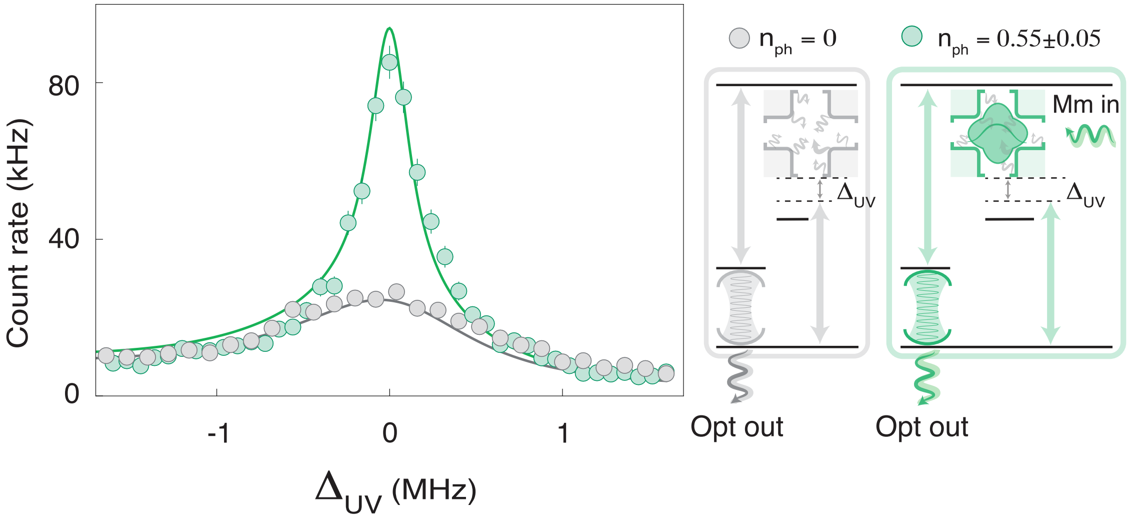

Figure 4.3: **Thermal noise characterization.** Optical count rate measured when the transducer is operated with no external millimeter-wave drive (gray) versus with an external drive (green) with an approximately an equal number of mean photons in the coherent drive as the thermal occupation.

The optical output rate with no drive is consistent with the theoretical predictions for $\bar{n}_{\text{thermal}} = 0.6$. However, to confirm that the noise isn't added from another source, we also perform $g^{(2)}(\tau)$ second-order temporal intensity correlation measurements of the converted output photons to characterize the statistics of the converted photons. For a coherently displaced thermal state, the second order correlation function $g^{(2)}(\tau)$ can be derived using methods similar to section 3.10:

$$\begin{aligned} g^{(2)}(\tau) &= \frac{\langle a^\dagger(0) a^\dagger(\tau) a(\tau) a(0)\rangle}{\langle a^\dagger(0) a(0)\rangle \langle a^\dagger(\tau) a(\tau)\rangle} \\ &= 1 + \frac{|\overline{g}^{(1)}_{th}(\tau) + \overline{g}^{(1)}_{coh}(\tau)|^2 - |\overline{g}^{(1)}_{coh}(\tau)|^2}{|\overline{g}^{(1)}_{th}(0) + \overline{g}^{(1)}_{coh}(0)|^2} \end{aligned} \tag{4.1}$$

We use the time tags on the photon detections on the two photon counters, and bin the counts to calculate the number of instances two photon clicks are detected at interval τ

averaged over the detection period, and normalize accordingly, to calculate $g^{(2)}(\tau)$.

Figure 4.4 shows the results for the $g^{(2)}(\tau)$ measurement for no coherent drive ($\bar{n}_{ph} = 0$, grey), coherent drive with mean number of photons equal to the mean thermal population ($\bar{n}_{ph} = 0.59$, orange) and coherent drive with $\bar{n}_{ph} = 1.25$ (green). At $\tau = 0$, $g^{(2)}(0) = 2$ for optical photons converted in the presence of no external drive, consistent with the bunched statistics of thermal photons (Appendix A.6, can also be seen from equation 4.1). As the strength of the coherent drive is increased, the $g^{(2)}(0)$ falls towards 1 because the coherent drive dominates.

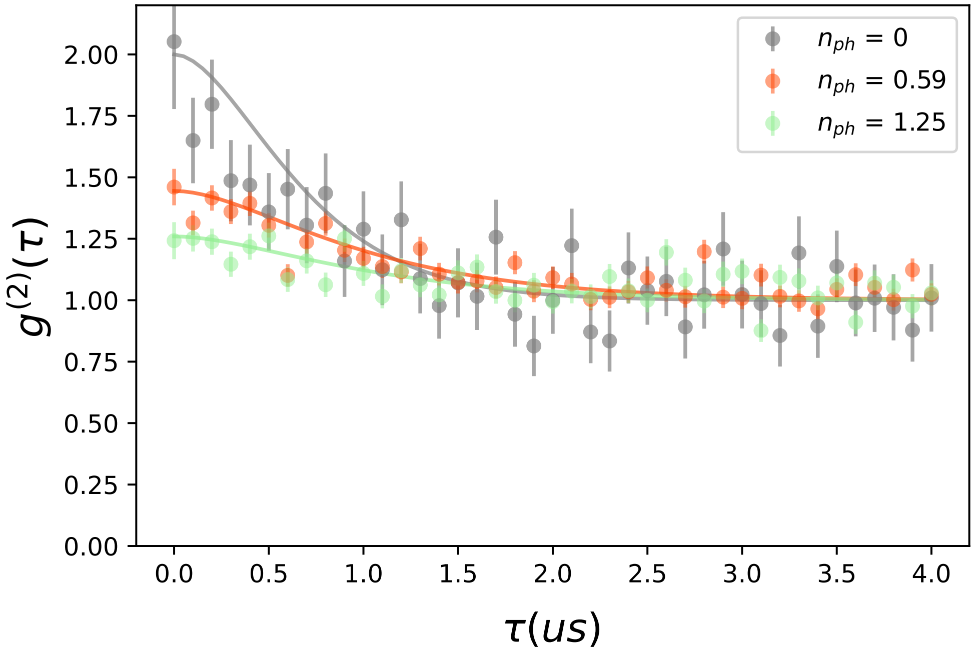

Figure 4.4: **Thermal noise characterization.** We measure the statistics of the optical photons converted from millimeter-wave photons by measuring the second-order intensity correlation function. The $g^{(2)}(0)$ is 2 for no external drive (corresponding to thermal millimeter-wave photons converted to optical photons) and approaches 1 as the external coherent drive is made stronger. The solid curves are theory curves.

4.3 Indirect probe of optical to millimeter-wave conversion

In the current experimental setup, we have in-chamber millimeter-wave attenuators (figure 3.17) in place to limit the entry of room-temperature thermal photons into the cavity through the millimeter-wave cable. This limits us from directly probing the optical to millimeter-wave conversion as the output signal will be highly attenuated. We indirectly probe the conversion of optical photons to millimeter-wave photons by turning the UV beam on at the impedance-matched parameters (figure 4.5). We observe that on turning interconversion on, the dark polariton feature becomes lower and broader. The lost optical photons correspond not only to the converted photons, but also to the extra photons reflected off the cavity input (because of different impedance matching conditions for the optical cavity due to conversion coupling). The probe-independent background in the case of conversion can be attributed to the conversion of thermal millimeter-wave photons to optical photons. The data matches our theoretical predictions (purple solid line) well.

4.4 Dependence on millimeter-wave drive strength

As we increase the external millimeter-wave drive strength, we observe that the conversion efficiency decreases faster as a function of conversion time for higher drive strengths (figure 4.6). This is likely because of the depumping of the atoms from the 5P state to outside the 4-level scheme in our model. It is for this reason we have to do intermediate optical pumping in our transduction measurement sequence.

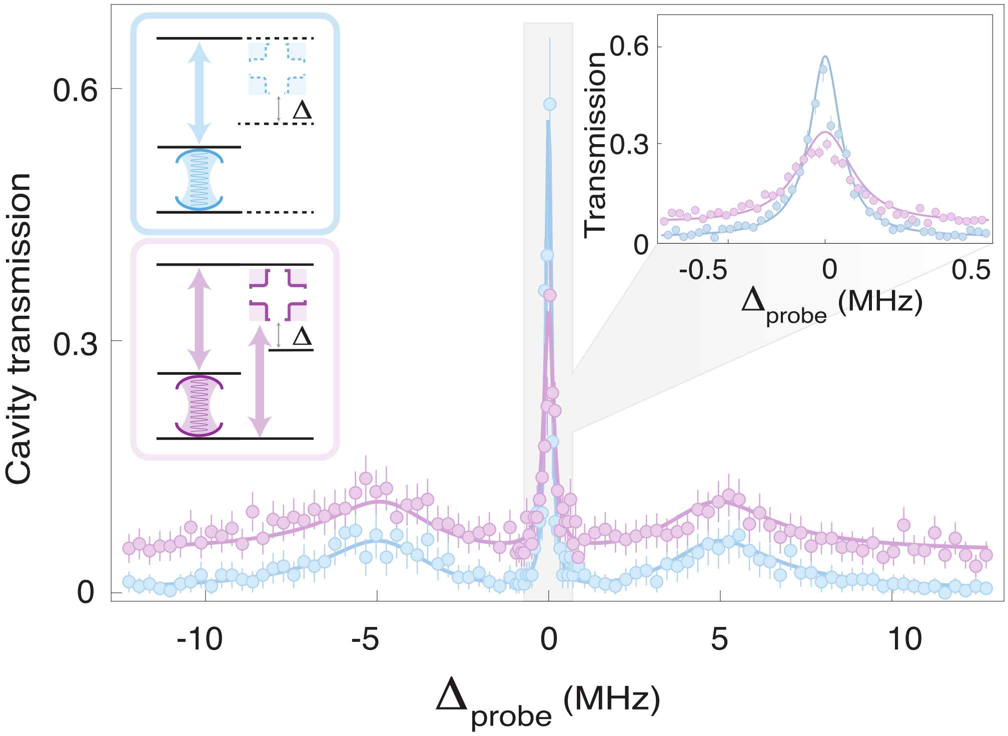

Figure 4.5: Indirect probe of conversion from optical photons to millimeter-wave photons. We indirectly probe optical → millimeter-wave transduction by observing optical transmission with (purple) and without (blue) the UV drive. The x-axis represents the detuning of the 780 nm probe from the optical cavity resonance. The inset zooms into the dark polariton feature in the spectrum, which is suppressed and broadened by the additional loss of conversion to millimeter-wave photons. The offset is due to conversion of thermal photons to optical photons.

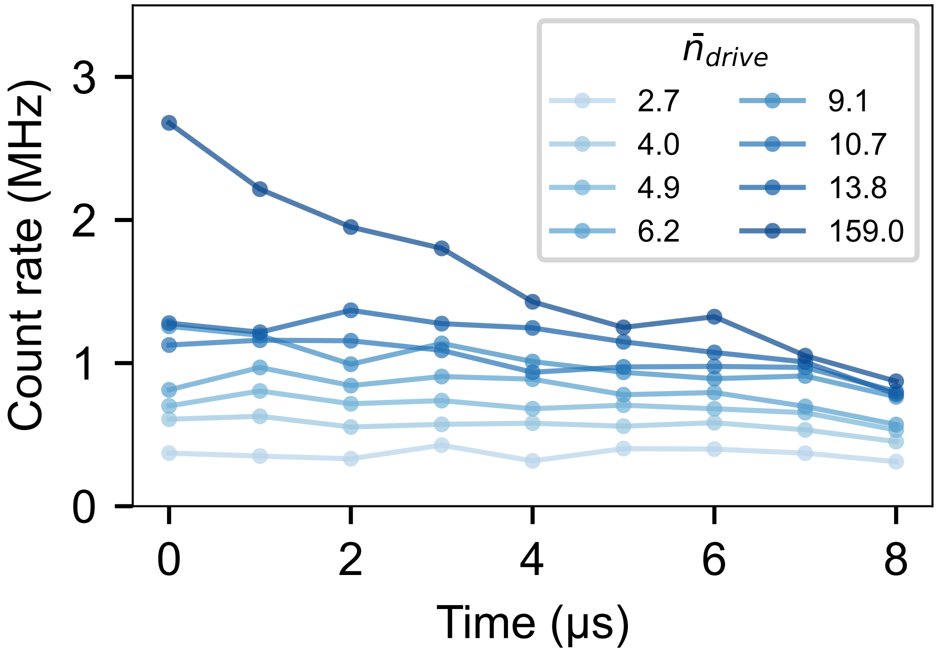

Figure 4.6: Dependence on millimeter-wave drive strength and interconversion time

4.5 Discussion

Performance metrics of the transducer

There are various metrics that can be used to characterize a transducer, with the primary metrics being the conversion efficiency, bandwidth and added noise in the transducer [62]. For quantum networking purposes, the figure of merit is the entanglement generation rate, which is the product of the efficiency, bandwidth and duty cycle of the transducer [63]. This distribution over a few performance metrics can allow for a lower efficiency continuous-wave transducer. However, the efficiency has to be high enough so as to not be limited by added noise.

Internal conversion efficiency

The internal conversion efficiency is currently limited by the blue cooperativity, which is dependent on the blue Rabi frequency and the loss rate of the collective 36S Rydberg state. There are several routes to improvement:

mm-wave mode polarization: switching the tubes such that the lowest frequency mode (the science mode) has polarization orthogonal to the optical cavity axis, would let us have circular polarizations for all the fields while maintaining phase matching – winning a factor of two for the blue Rabi frequency (hence 4 on cooperativity. It also provides a 1.2 enhancement for the optical cavity coupling g_{opt}).

Further cooling of the atomic ensemble: Techniques such as degenerate Raman sideband cooling can be employed to cool the cloud below 5 microkelvins to reduce the dark polariton linewidth (the reduction is linear in temperature).

Compression of cloud: The blue beam is required to be uniform across the atomic ensemble to maintain the collective state coherence. Compressing the cloud using an intracavity lattice or dipole trap will allow to work with smaller beam waists at the same power, leading to a stronger field and hence a higher Rabi frequency.

An increased blue cooperativity will require an increase in the optical and millimeter-wave cooperativities as well, which can be more easily increased by increasing the total atom number and the 35P dressing fraction via UV detuning. These factors should enable an internal efficiency of about 96%.

Overall conversion efficiency

The overall conversion efficiency, given by $\epsilon = \frac{\kappa_{\text{opt}}^{\text{ext}}\kappa_{\text{mm}}^{\text{ext}}}{\kappa_{\text{opt}}\kappa_{\text{mm}}}\eta$, where η is the internal conversion efficiency. In our system, it is primarily limited by the external linewidth of the millimeter-wave cavity $\kappa_{\text{mm}}^{\text{ext}}$. It can easily be increased by a factor of about 2 by removing a copper plate currently between the millimeter-wave waveguide and the resonator (it was placed for another experiment to decrease the total cavity linewidth for observing single millimeter-wave photon nonlinearity). It can further be increased by a factor of about 50 by shortening the length of the incoupling waveguide by 2 mm. The increase in the external coupling will also increase the overall linewidth, leading to a decrease in the cooperativity at the millimeter-wave transition. This can be offset by increasing the 35P state dressing fraction.

Colder temperatures

Ultimately, going to colder temperatures around 1K is desirable because 1) lower thermal background of ∼0.01 photons instead of 0.6 at 5K. 2) Higher quality factor leading to higher cooperativity at the millimeter-wave transition, which will help in suppressing the loss channels faster. At 1K, the internal loss rate of the cavity can be reduced to under $2\pi\times10$ kHz [51], with the possibility of increasing the external coupling by a factor of 10, resulting in roughly the same κ_{mm} and conversion bandwidth that we now have. 3) Transducing *microwave* photons to integrate with existing superconducting qubit-based processors:

The technique can potentially be implemented for microwave ↔ optical interconversion via either (1) direct interconversion with atoms in larger, microwave resonators and higher Rydberg levels; or (2) four-wave mixing with kinetic inductance devices as an intermediate stage to interconvert millimeter-waves and microwaves [64].

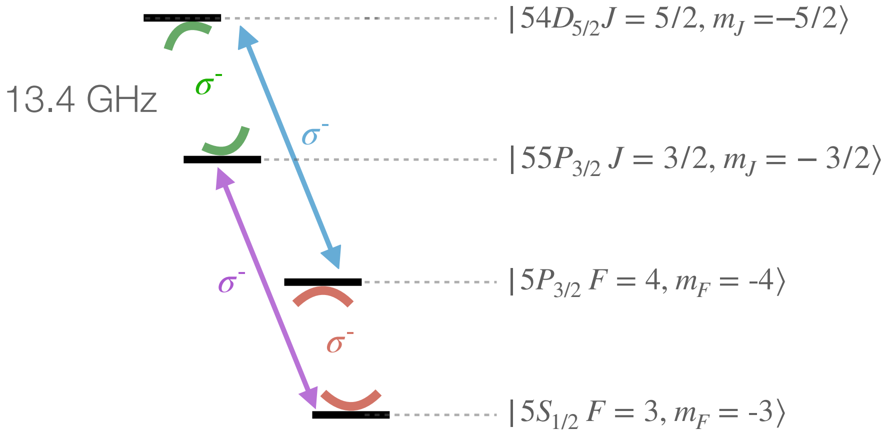

Figure 4.7: A possible scheme for higher Rydberg states

Scaling up the current resonator by a factor of about 10, for example, operating at a lower temperatures, and using $n = 55$ $P_{3/2}$ and $n = 54$ $D_{5/2}$ Rydberg states in Rubidium could enable conversion close to $\sim$ 13 GHz frequencies. Appendix A.7 shows some EIT spectra for higher Rydberg states upto n = 60 in our current cavity. The larger resonator would imply a larger mode volume ($\sim 10^3$ times) leading to a factor of about 30 decrease in single-atom-cavity coupling. This effect can be partially offset by the lower linewidth from colder temperatures.

Chapter 5

Strong coupling between optical cavity modes separated by 200 THz

This chapter is based on reference [26].

Typical applications of optical cavities rely on uncoupled, monochromatic cavity eigenmodes. In the previous two chapters, we saw how coupling cavity modes at different frequencies can enable frequency conversion across a wide energy gap. In addition to frequency transduction, coupled[1] cavity modes can enable applications such as generation of squeezed light [66, 67], narrow bandwidth generation of entangled photon-pairs [68], and generation of single-photon nonlinearities [69–71]. The coupling can be mediated by atomic ensembles, or more commonly, by $\chi^{(2)}$ nonlinear materials [45, 66–72].

This chapter presents a macroscopic, doubly-resonant cavity with an intracavity nonlinear crystal to demonstrate strong coherent coupling between cavity modes at two *optical* frequencies (384 THz (780 nm) and 580 THz (516 nm)). The coupling, mediated by a classical, non-resonant optical pump, provides hybridized Floquet eigenmodes at the two frequencies.

---

[1] The coupling can be of different types. For example, the Hamiltonian of resonant OPOs has terms such as $\sim g_{pump} a^\dagger b^\dagger + g^*_{pump} ab$ [65]. In this experiment, we work with an $a^\dagger b + ab^\dagger$ Hamilonian.

We utilize this mode coupling to demonstrate frequency conversion for a classical input with 30(1)% end-to-end efficiency in free space, at 90 mW of pump power. We also demonstrate strong coupling between otherwise orthogonal spatial modes at the two frequencies.

The chapter is organized as follows: sections 5.1 and 5.2 provide a brief background on nonlinear crystals. Sections 5.3 and 5.4 discuss the theory and the experimental platform. Section 5.5 presents data demonstrating strong coherent coupling between two single-frequency cavity modes. Sections 5.6 and 5.7 discuss the cooperative enhancement provided by the system and present results on classical transduction and spatial mode coupling respectively. Sections 5.8 - 5.9 outline routes to improve performance of the platform toward higher cooperativities and lower pump powers, and discusses potential applications to atomic and classical optics platforms.

5.1 Sum-frequency and difference-frequency generation in nonlinear crystals

When a dielectric material is placed in an electric field, its constituent charges are displaced. The material becomes polarized according to

$$P = \varepsilon_0 \left(\chi^{(1)} E + \chi^{(2)} E^2 + \chi^{(3)} E^3 + \cdots \right) = P^{(1)} + P^{(2)} + P^{(3)} \cdots ,$$

where $\chi^{(1)}$ is the linear susceptibility and $\chi^{(2)}$, $\chi^{(3)}$, etc., are higher-order nonlinear susceptibilities. The nonlinear effects become significant in the presence of one or more strong electric fields. Sum-Frequency Generation (SFG) and Difference-Frequency Generation (DFG) are two such nonlinear processes, where two input waves interact within a nonlinear medium to generate a third wave. The induced polarization $P^{(2)}(\omega_3) = \epsilon_0 \chi^{(2)} E_1(\omega_1) E_2(\omega_2)$ acts as a source term in Maxwell's equations, leading to the generation of the new wave at ω_3.

In SFG, two incident waves at frequencies ω_1 and ω_2 combine to generate a higher-frequency wave at $\omega_3 = \omega_1 + \omega_2$. This process is commonly used for frequency upconversion, such as visible light generation from infrared sources. In DFG, the nonlinear interaction produces a lower-frequency wave at $\omega_3 = |\omega_1 - \omega_2|$, effectively converting higher-energy photons into lower-energy ones.

In addition to sum- and difference-frequency generation, nonlinear crystals can support other nonlinear optical processes. In second-harmonic generation (SHG), two photons at the same frequency combine to produce a single photon at twice the frequency. Parametric down-conversion (PDC) is another important process, in which a single high-energy photon splits into two lower-energy entangled photons.

These nonlinear processes preserve the quantum coherence and phase relationships of the interacting fields. They have been the backbone of experiments for generation of entangled pair sources [72–74], photonic gates [69, 70] and are widely used for quantum frequency conversion applications [75–81].

5.2 Intracavity nonlinear processes

Low-finesse cavity enhancement of strong pump and/or input fields is commonly employed to obtain high conversion efficiencies for nonlinear frequency mixing in free-space platforms [72, 82]. Taking advantage of small mode volumes, integrated photonics platforms can provide higher conversion efficiencies at lower pump powers [70, 71, 83, 84].

In addition to field build-up at the input and the pump, Purcell-enhanced emission of the output into resonant cavity modes has enabled various applications such as doubly-resonant optical parametric oscillators [72] to obtain gain for photon-pair generation, optical frequency tweezers to pick and convert frequencies from a broad source [85], sources for frequency-converted orbital angular momentum modes [86, 87], and photon-pair sources with bandwidths matched to atomic quantum memories [68].

A strong coupling condition for two cavity modes is very similar to that discussed in chapter 2 for an atom and a cavity mode. It is achieved when the coupling strength between two modes exceeds the loss rates of the two modes. Strong coupling of optical cavity modes and consequent frequency conversion have previously been demonstrated in triply-resonant aluminum nitride [88] and silicon nitride [89] microring resonators. The tight confinement of optical modes and longer interaction lengths in these nanophotonic platforms provide large coupling strengths at low pump powers [69–71]. However, compared to free-space cavities, these systems are limited by fiber-device coupling efficiencies[2] and cannot accommodate quantum systems such as neutral atoms for cavity-QED experiments.

5.3 Theory: Coupled cavity modes in a free-space doubly-resonant cavity

5.3.1 Coupled cavity Hamiltonian

Let us consider the interaction between two cavity modes, $\hat{a}_{\mathrm{DF}}$ and $\hat{a}_{\mathrm{SF}}$, mediated by an intracavity $\chi^{(2)}$ nonlinear crystal that is driven by a classical pump field at frequency ω_p. In the laboratory frame, the Hamiltonian describing this system is

$$\begin{aligned} H = {} & \hbar\omega_{\mathrm{DF}}\hat{a}^{\dagger}_{\mathrm{DF}}\hat{a}_{\mathrm{DF}} + \hbar\omega_{\mathrm{SF}}\hat{a}^{\dagger}_{\mathrm{SF}}\hat{a}_{\mathrm{SF}} \\ & + \hbar g\left(\hat{a}^{\dagger}_{\mathrm{DF}}\hat{a}_{\mathrm{SF}}e^{-i\omega_p t} + \hat{a}_{\mathrm{DF}}\hat{a}^{\dagger}_{\mathrm{SF}}e^{i\omega_p t}\right), \end{aligned} \tag{5.1}$$

where ω_{DF} and ω_{SF} are the resonance frequencies of the bare cavity modes, and g is the nonlinear coupling strength. The time dependence of the coupling arises from the classical pump field, which oscillates at ω_p.

---

[2] Integrated photonics platforms typically lose 4-8 dB in fiber-chip coupling per facet [69, 70].

In a frame rotating with the pump field, the Hamiltonian can be written as

$$H = -\delta_{\text{pump}}\hat{a}^{\dagger}_{\text{SF}}\hat{a}_{\text{SF}} + g(\hat{a}^{\dagger}_{\text{DF}}\hat{a}_{\text{SF}} + \hat{a}_{\text{DF}}\hat{a}^{\dagger}_{\text{SF}}) \tag{5.2}$$

δ_{pump} is the detuning between the two cavity modes set by the detuning of the pump from $\omega_{p,0} = \omega_{\text{SF}} - \omega_{\text{DF}}$. The coupling strength is $g = \sqrt{\epsilon}\ \Phi\ \nu$, where ϵ is the single-pass conversion efficiency for the crystal, Φ is the spatial mode overlap factor for the pump beams and the cavity modes, and ν is the free-spectral range $c/2L$, where L is the length of the cavity. The expression generally holds true for any two cavity modes coupled by a coupler of efficiency ϵ [30] and has been experimentally demonstrated for near-degenerate coupled resonators [90, 91]. Appendix A.8 outlines a first-principles derivation of g from a three-level system modeling of the $\chi^{(2)}$ coupling. Since the out-of-cavity conversion efficiency ϵ scales linearly with pump-power, the coupling has a square-root dependence on the pump-power.

The beamsplitter Hamiltonian in Eq. 5.2 describes two coupled bosonic modes with the pump frequency controlling the detuning of the drive between the DF and SF cavity modes, and the pump power controlling the coupling strength. Diagonalizing the Hamiltonian yields two eigenmodes that are superpositions of the uncoupled cavity eigenmodes of the form $\hat{a}_{+} = (\cos\left(\frac{\theta}{2}\right)\hat{a}_{\text{DF}} + \sin\left(\frac{\theta}{2}\right)\hat{a}_{\text{SF}})$ and $\hat{a}_{-} = (-\sin\left(\frac{\theta}{2}\right)\hat{a}_{\text{DF}} + \cos\left(\frac{\theta}{2}\right)\hat{a}_{\text{SF}})$, where $\tan(\theta) = 2g/\delta_{\text{pump}}$. Thus, the new cavity quantizes the electromagnetic field in a way such that each eigenmode has two frequency components.

Once losses are introduced via the total linewidths of the cavity at the SF and DF, the two-mode-cooperativity $\mathcal{C} = \frac{4g^2}{\kappa_{\text{DF}}\kappa_{\text{SF}}}$ compares the coupling rate with dissipation rates of the two modes. It provides information about the maximum number of coherent exchanges that can take place between the two cavity modes before the light is lost to the environment. A resolvable splitting in the spectrum, corresponding to the condition $2g > (\kappa_{\text{SF}} + \kappa_{\text{DF}})/2$, implies cooperativity $\mathcal{C} > 1$, the strong-coupling condition of cavity QED.

5.3.2 Driven cavity equations for coupled cavity modes

From the simplified Hamiltonian, the Langevin equations for coupled cavity modes a and b (single-ended cavity) are written as [30]

$$\begin{aligned}
\partial_t a(t) &= -i\omega_{0,a}a(t) - \frac{\kappa_a}{2}a(t) - i\mathcal{E}e^{-i\omega_L t} - \sqrt{\kappa_a^{\text{ext}}}a_{in}(t) - ige^{i\omega_p t}b(t) \\
\partial_t b(t) &= -i\omega_{0,b}b(t) - \frac{\kappa_b}{2}b(t) - \sqrt{\kappa_b^{\text{ext}}}b_{in}(t) - ige^{-i\omega_p t}a(t)
\end{aligned}$$

where $\mathcal{E}e^{-i\omega_L t}$ is the coherent drive term with frequency ω_L for cavity mode a, $\{\omega_{0,i}$, κ_i and $\kappa_i^{\text{ext}}\}$ are the resonance frequency, total linewidth and external linewidth for mode i. $ge^{i\omega_p t}$ is the coupling term introduced by the pump. We define rotating frame operators:

$$\begin{aligned}
\tilde{a} &:= ae^{i\omega_L t} \\
\tilde{b} &:= be^{i(\omega_L+\omega_p)t}
\end{aligned}$$

With the external bath in vacuum state (hence $\langle a_{in}\rangle, \langle b_{in}\rangle = 0$), at steady state:

$$\begin{aligned}
i(\omega_L - \omega_{0,a})\tilde{a} - i\mathcal{E} - \frac{\kappa_a}{2}\tilde{a} - ig\tilde{b} &= 0 \\
i(\omega_L + \omega_p - \omega_{0,b})\tilde{b} - \frac{\kappa_b}{2}\tilde{b} - ig\tilde{a} &= 0
\end{aligned}$$

Let $\omega_L - \omega_{0,a} = \delta_{L,a0}$ and $\omega_p = \omega_{0,p} + \delta_{pump}$. With $\omega_{0,a} + \omega_{0,p} = \omega_{0,b}$,

$$\begin{aligned}
i\delta_{L,a0}\tilde{a} - i\mathcal{E} - \frac{\kappa_a}{2}\tilde{a} - ig\tilde{b} &= 0 \\
i(\delta'_{L,a0} + \delta_{\text{pump}})\tilde{b} - \frac{\kappa_b}{2}\tilde{b} - ig\tilde{a} &= 0
\end{aligned}$$

The input-output relations provide the output leaking out of the cavity for the two modes:

$$\begin{aligned}
\langle a_{out}\rangle &= \mathcal{E}e^{-i\omega_L t}/\sqrt{\kappa_a^{\text{ext}}} + \sqrt{\kappa_a^{\text{ext}}}\langle\tilde{a}\rangle e^{-i\omega_L t} \\
\langle b_{out}\rangle &= \sqrt{\kappa_b^{\text{ext}}}\langle\tilde{b}\rangle e^{-i(\omega_L+\omega_p)t}
\end{aligned} \tag{5.3}$$

These relations provide expressions that are used to fit experimental data. The κ_{DF} is determined independently from fits to finesse measurements.

5.3.3 Coupled cavity conversion efficiency and impedance matching

Using the input-output relations, the conversion efficiency from DF to SF at DF resonance and zero probe detuning is

$$\left|\frac{\hat{a}_{\mathrm{SF}}^{\mathrm{out}}}{\hat{a}_{\mathrm{DF}}^{\mathrm{in}}}\right|^2 = \frac{16g^2\kappa_{\mathrm{DF}}^{\mathrm{ext}}\kappa_{\mathrm{SF}}^{\mathrm{ext}}}{(4g^2+\kappa_{\mathrm{DF}}\kappa_{\mathrm{SF}})^2} = \frac{4\mathcal{C}}{(1+\mathcal{C})^2}\frac{\kappa_{\mathrm{DF}}^{\mathrm{ext}}}{\kappa_{\mathrm{DF}}}\frac{\kappa_{\mathrm{SF}}^{\mathrm{ext}}}{\kappa_{\mathrm{SF}}} \tag{5.4}$$

where $\kappa_i^{\mathrm{ext}} = T_i\nu_i$ denote the external linewidths of the cavity modes, with T = transmission coefficient of the coupling mirror at frequency i.

For fixed internal losses and coupling g, the highest conversion efficiencies are achieved when there is zero reflection from the input port. The expression for the reflection is

$$\left|\frac{\hat{a}_{\mathrm{DF}}^{\mathrm{out}}}{\hat{a}_{\mathrm{DF}}^{\mathrm{in}}}\right|^2 = \Big(\frac{\mathcal{C}_{\max}+(\beta_{\mathrm{DF}}-1)(1+\beta_{\mathrm{SF}})}{\mathcal{C}_{\max}+(1+\beta_{\mathrm{DF}})(1+\beta_{\mathrm{SF}})}\Big)^2$$

where $\beta_i = \frac{\kappa_i^{\mathrm{ext}}}{\kappa_i^{\mathrm{int}}}$.

Physically, the condition $|a_{out}|^2 = 0$ requires the input rate of photons ($\kappa_{\mathrm{DF}}^{\mathrm{ext}}$) should equal to the sum of the loss rate from the first cavity ($\kappa_{\mathrm{DF}}^{\mathrm{int}}$) and the rate of coupling to the other cavity ($\frac{4g^2}{\kappa_{\mathrm{SF}}}$)

$$\kappa_{\mathrm{DF}}^{\mathrm{ext}} = \kappa_{\mathrm{DF}}^{\mathrm{int}} + \frac{4g^2}{\kappa_{\mathrm{SF}}}$$

$$(\kappa_{\mathrm{DF}}^{\mathrm{ext}} - \kappa_{\mathrm{DF}}^{\mathrm{int}})(\kappa_{\mathrm{SF}}^{\mathrm{ext}} + \kappa_{\mathrm{SF}}^{\mathrm{int}}) = 4g^2$$

Since the converter should be symmetric in operation, we can interchange a and b to write

$$(\kappa_{\mathrm{SF}}^{\mathrm{ext}} - \kappa_{\mathrm{SF}}^{\mathrm{int}})(\kappa_{\mathrm{DF}}^{\mathrm{ext}} + \kappa_{\mathrm{DF}}^{\mathrm{int}}) = 4g^2$$

which implies

$$\frac{\kappa_{\mathrm{DF}}^{\mathrm{ext}}}{\kappa_{\mathrm{DF}}^{\mathrm{int}}} = \frac{\kappa_{\mathrm{SF}}^{\mathrm{ext}}}{\kappa_{\mathrm{SF}}^{\mathrm{int}}} = \sqrt{1 + \frac{4g^2}{\kappa_{\mathrm{DF}}^{\mathrm{int}}\kappa_{\mathrm{SF}}^{\mathrm{int}}}}, \text{ or}$$

$$\beta_{\mathrm{DF}} = \beta_{\mathrm{SF}} = \sqrt{1 + \mathcal{C}_{\mathrm{max}}}$$

Given the constraints on $\kappa_{\mathrm{DF}}^{\mathrm{int}}$ and $\kappa_{\mathrm{SF}}^{\mathrm{int}}$, the optimum overall efficiency achievable is

$$\begin{aligned} \left|\frac{\hat{a}_{\mathrm{SF}}^{\mathrm{out}}}{\hat{a}_{\mathrm{DF}}^{\mathrm{in}}}\right|_{\mathrm{opt}}^{2} &= \frac{2 + \mathcal{C}_{\mathrm{max}} - 2\sqrt{1 + \mathcal{C}_{\mathrm{max}}}}{\mathcal{C}_{\mathrm{max}}} \\ &\underset{\mathcal{C}_{\mathrm{max}} \gg 1}{\approx} 1 - \frac{2}{\sqrt{\mathcal{C}_{\mathrm{max}}}} \end{aligned}$$

5.4 Experimental platform

The experiment is described in Fig 5.1. We integrate a bulk 1 cm long 5% MgO-doped ppLN crystal within a macroscopic Fabry-Pérot optical cavity designed to be resonant at 780 nm and 516 nm. The surfaces of the crystal are AR coated for 780 nm (R ∼ 0.0005) and 516 nm (R ∼ 0.0004) to minimize cavity loss. The crystal supports a cavity finesse of up to 830(10) (figure 5.2a) at 780 nm, with a limiting finesse of about 1000.

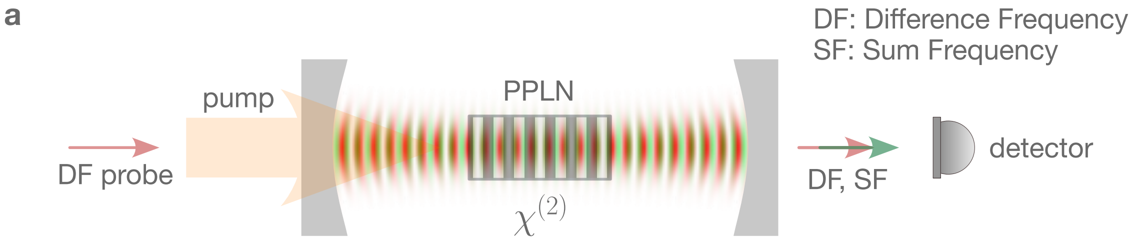

Figure 5.1: Intracavity nonlinear crystal in a doubly-resonant cavity. An AR-coated and periodically-poled 5% MgO doped lithium niobate (ppLN) bulk crystal is placed within a macroscopic Fabry-Pérot cavity which is doubly-resonant at 780 nm (difference-frequency or DF) and 516 nm (sum-frequency or SF) wavelengths. The 10 mm long crystal is positioned approximately at the center of the 82 mm long cavity. At the input and output, the different beams are combined and separated using dichroics. The cavity length is stabilized by locking to a reference 785 nm tracer laser for most experiments.

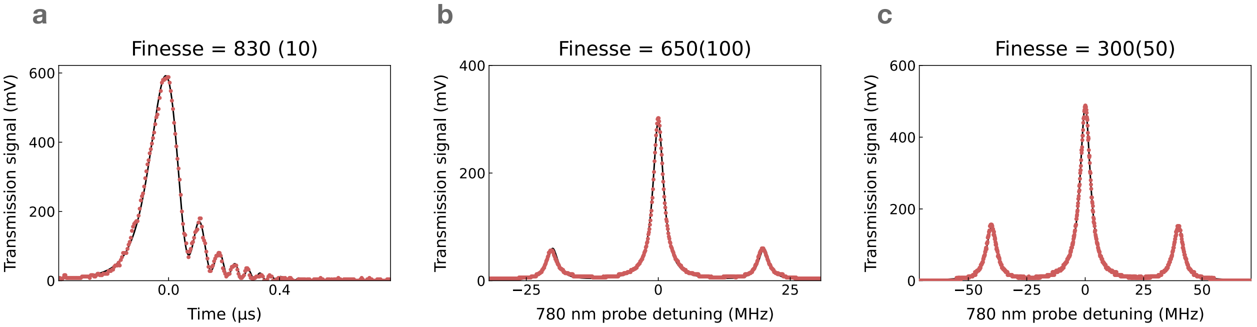

Figure 5.2: Measurement of cavity finesse with intracavity 5%-MgO doped ppLN crystal at 780 nm for various experiments in the chapter. (a) Measurement via a cavity ringdown measurement [92]. The cavity transmission, when the probe frequency sweep rate $> \kappa/\mathcal{F}$, displays an oscillating behavior which can be fit to an exp-erfc function. The measured finesse $\mathcal{F} = 830(10)$ suggests a round-trip loss of 0.76% in the crystal cavity. The error is calculated from the fit. (b), (c) Finesse measurements by modulating the probe using an EOM for (b) avoided-crossing measurements, and (c) conversion efficiency measurements with higher transmission outcoupler. The errors are calculated from uncertainties in cavity length measurement and x-axis calibration. The difference in (a) and (b) is most likely due to contamination during the course of the experiment. The finesse in (c) is lower due to contributions from the higher outcoupling end mirror.

5.4.1 Phase matching

In a material like lithium niobate, the refractive indices at the pump, sum-frequency (SF), and difference-frequency (DF) wavelengths are considerably different, leading to a wavevector mismatch that prevents natural phase matching. This limits the usable length of the crystal to smaller than the coherence length $L_c = \pi/|\Delta k| = \pi/|k_{pump} + k_{DF} - k_{SF}|$, which for our wavelengths is about 3 microns at 35° C. Beyond this length, the accumulated phase mismatch causes newly generated waves to interfere destructively with earlier ones, reducing the overall efficiency of the nonlinear process. To extend the effective interaction length, quasi-phase matching (QPM) is implemented, where the nonlinear susceptibility is periodically inverted to compensate for phase mismatch and maintain constructive interference over a longer propagation distance.

The periodic poling of the crystal in the experiment is designed (HC Photonics) to provide quasi-phase matching at 35° C. Fig 5.3(a) shows the temperature dependence of converted power in free-space. The translation of the peak from specified temperature is likely due to angle of incidence deviation from 0°. Once the crystal is placed inside the cavity, we observed a maximum around 34.9°C (Fig 5.3(b). Since our crystal surfaces are ∼30% reflective at 1529 nm, the pump wavelength, there is an etalon effect leading to periodic variations in intracavity pump power, which leads to dips in Fig 5.3(b). With the temperature fixed, when the pump frequency is scanned (Fig 5.3(c)), the frequency spacing of the oscillations is $\sim 4\times$ cavity FSRs = 6.4 GHz, which matches the crystal etalon free-spectral range after accounting for the refractive index of lithium niobate.

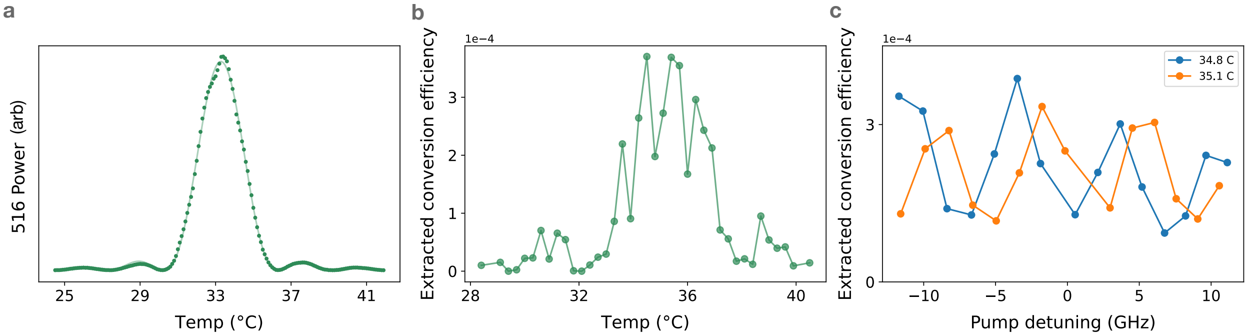

Figure 5.3: Phase matching characterizations (a) Out of cavity, we send 780 nm light into the crystal and measure the converted 516 nm power to characterize the crystal temperature dependence of frequency conversion. The data is fit to a sinc-squared function. (b) We place the crystal within the cavity and extract the single-pass conversion efficiency from the splitting in the spectrum ($g = \sqrt{\epsilon}\ \nu$). In this measurement, the temperature is scanned and the pump frequency is kept fixed. The difference in optimal temperature is likely due to different crystal angles. The anomalous dips appear due to a crystal etalon effect for the pump (see text), confirmed by a pump frequency scan in (c) at fixed temperature.

The crystal is mounted on a 4-axis translation stage between two curved mirrors (ROC 100 mm) that form a standing-wave cavity at 780 nm and 516 nm. The 780 cavity waist is designed to be 110 μm, 516 to be 90 μm and the pump waist is estimated to be $\sim$ 116 μm (Sec 5.8). The 1529 nm pump is sourced from an EDFA (Amonics AEDFA-PM-37-R-NC, seed: Gooch and Housego).

It is noteworthy that the crystal simultaneously provides quasi-phase-matching for the difference-frequency generation of 780 nm from 516 nm using the same pump at 1529 nm, allowing symmetric bidirectional coupling.

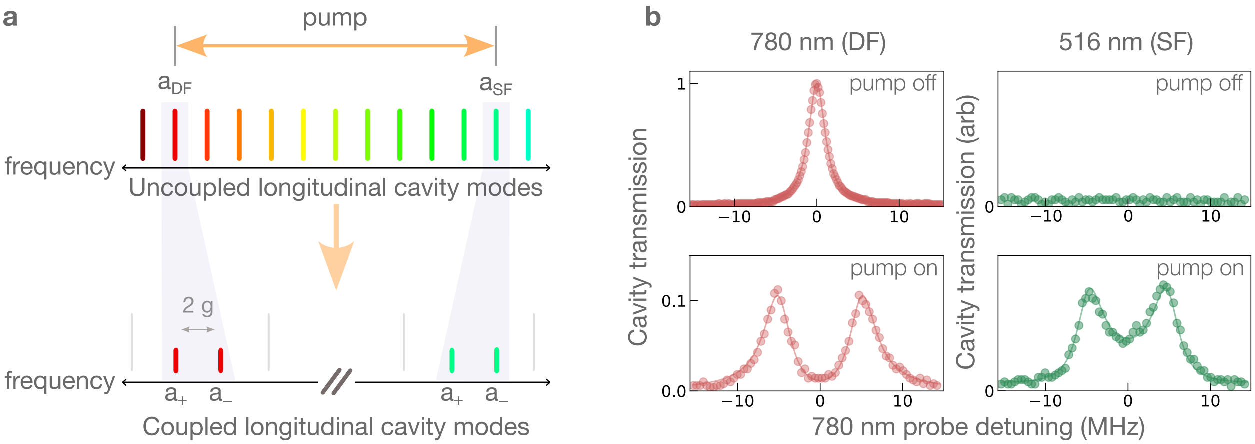

Figure 5.4: Optical pump-mediated coupling of cavity modes at 780 nm and 516 nm. (a) When pumped at 1529 nm, the crystal couples the two cavities modes ($\hat{a}_{\mathrm{DF}}$ and $\hat{a}_{\mathrm{SF}}$) via sum- and difference-frequency generation processes. When the pump is near two-mode resonance, this coupling admixes the two modes yielding eigenmodes (with lowering operators $\hat{a}_+$ and $\hat{a}_-$) that are the superposition of the DF and SF modes. In the absence of loss, the minimum frequency splitting between the hybridized modes is determined by the coupling strength $g = \sqrt{\epsilon}\ \nu$, where ϵ is the single-pass wavelength-conversion efficiency and ν is the cavity free-spectral range ($c/2L_{\mathrm{cav}}$). (c) We measure the coupled resonator transmission at DF and SF as a function of the detuning of the DF probe laser from the DF cavity resonance and observe a mode splitting in the spectrum when the crystal is driven by a pump. The frequency splitting is evidence of hybridization of the DF and SF modes. The solid lines are fits. The spectra correspond to a coupling $g = 2\pi \times 5.0(2)$ MHz and cavity decay rates $\{\kappa_{\mathrm{DF}}, \kappa_{\mathrm{SF}}\} = 2\pi \times \{2.5(1), 6(1)\}$ MHz, providing a cooperativity $\mathcal{C} = 4g^2/\kappa_{\mathrm{DF}}\kappa_{\mathrm{SF}} = 7(1)$.

5.5 Coupled-cavity spectroscopy: splitting of modes

At the two-cavity resonance ($\delta_{\mathrm{pump}} = 0$), the coupling between the two frequency modes manifests spectroscopically as a frequency splitting of $2g$ in the cavity transmission spectrum (figure 5.4a). Fig 5.4(b) shows the observed spectrum at 780 nm and 516 nm when the cavity is probed via an input at 780 nm using a pump power of ∼200 mW. The symmetric splitting corresponds to $g = 2\pi \times 5.0(2)$ MHz, with total cavity linewidths of $\{\kappa_{\mathrm{DF}}, \kappa_{\mathrm{SF}}\} = 2\pi \times \{2.5(1), 6(1)\}$ MHz, corresponding to $\mathcal{C} = 7(1)$.

Figure 5.5 shows an avoided crossing in cavity transmission around the bare DF and SF

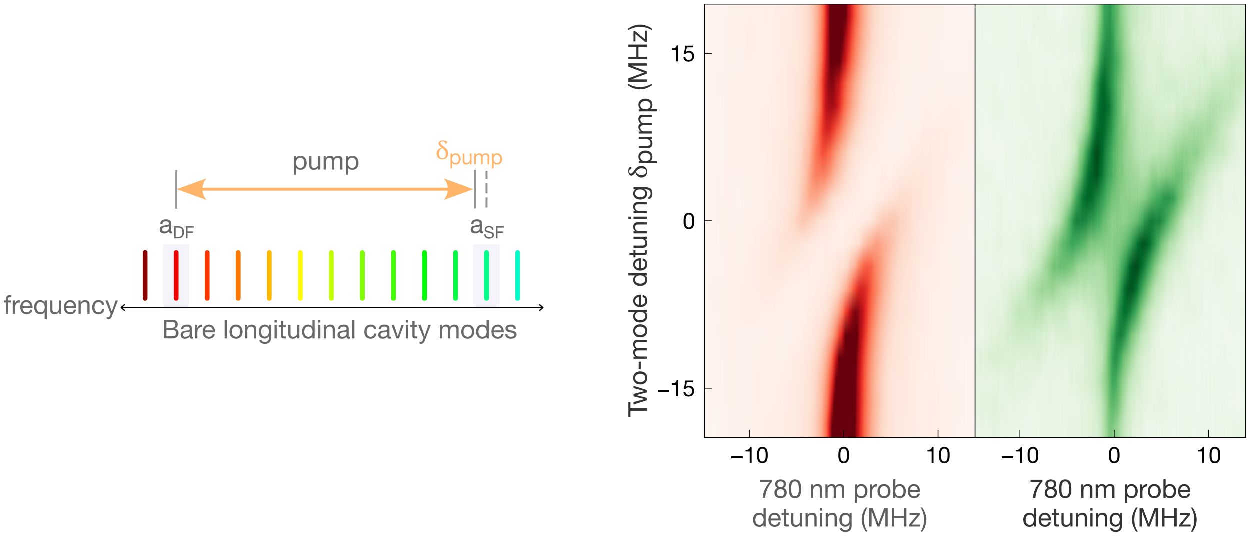

Figure 5.5: Dependence on pump frequency. The contribution of the bare modes to the hybridized modes is controlled by the detuning δ_{pump} of the pump from the two-mode resonance. The relative strengths of the DF and SF modes in the hybridized modes vary as the pump frequency is swept across two-cavity resonance as depicted in the cavity transmission at 780 nm (left, red) and 516 nm (right, green), as the 780 nm probe frequency and the two-cavity detuning (set by the 1529 nm pump frequency) are simultaneously scanned.

modes as the cavity is probed with 780 nm light and the pump detuning δ_{pump} is scanned. Each horizontal slice on the avoided-crossing diagram in figure 5.5 is the output of the cavity at 780 nm and 516 nm when it is probed with 780 nm light.

The contributions of each of the bare modes toward the new eigenmodes vary with the pump detuning, resulting in the variation of the cavity transmission of the peaks. At the two-cavity resonance, we measure two peaks with equal transmission. Away from resonance, we measure more 780 nm transmission corresponding to the mode that has more contribution from the uncoupled DF eigenmode.

If the dissipation of the two modes are equal, we expect equal transmissions for the split peaks in the SF transmission. This is because even with a lower SF contribution in an eigenmode, the excitation amplitude from the DF probe is stronger due to larger DF mode contribution. The two peak transmissions in the 516 nm spectrum should simultaneously decrease as the pump is tuned away from the two-mode resonance, because the eigenmodes that are excited more have less contribution from the SF mode. In this case, however, we see asymmetric transmission for the two 516 nm peaks at each horizontal slice away from resonance. This is due to a higher dissipation rate of the SF cavity mode than of the DF cavity mode, leading to seeing more loss (hence lower SF transmission) for coupled modes that have higher contribution of the bare SF mode.

For this experiment, the cavity is crystal-loss dominated as both end-mirrors are coated at 99.965% for 780 nm and 99.963% for 516 nm, leading to an undercoupled resonator setup. For better impedance matching and thus higher SNR, the mirrors should be coated for higher transmission at 780 nm and 516 nm. The mirrors are coated for high transmission at 1529 nm (R = 0.02%).

The cavity length is locked absolutely to a stable reference. It is stabilized to a tracer 785 nm laser, which has been co-locked with the probe carrier using a separate stable transfer cavity. We sweep the probe frequency using an electro-optic modulator driven by a crystal oscillator and vary the detuning of the two cavities via frequency sweep of the 1529 nm pump.

5.6 Optical transduction of a classical drive

While ultimately, we would want to characterize transduction of individual photons, we present an experimental proof of concept using a classical drive. This section presents conversion efficiency results for conversion from a continuous classical drive at 780 nm to 516 nm.

To obtain higher end-to-end conversion efficiency from better impedance matching, the mirror used as the 780 nm incoupler and 516 nm outcoupler is coated for 1.34% transmission at 780 nm and 2.36% transmission at 516 nm. The other end-mirror is the same from the avoided-crossing experiment, functioning as the blocked end of the cavity. The small leakage at 780 nm from the this highly reflective mirror is used to stabilize the cavity to 780 nm resonance. The outcoupler is unintentionally coated for 98.6% reflection at 1529 nm, which

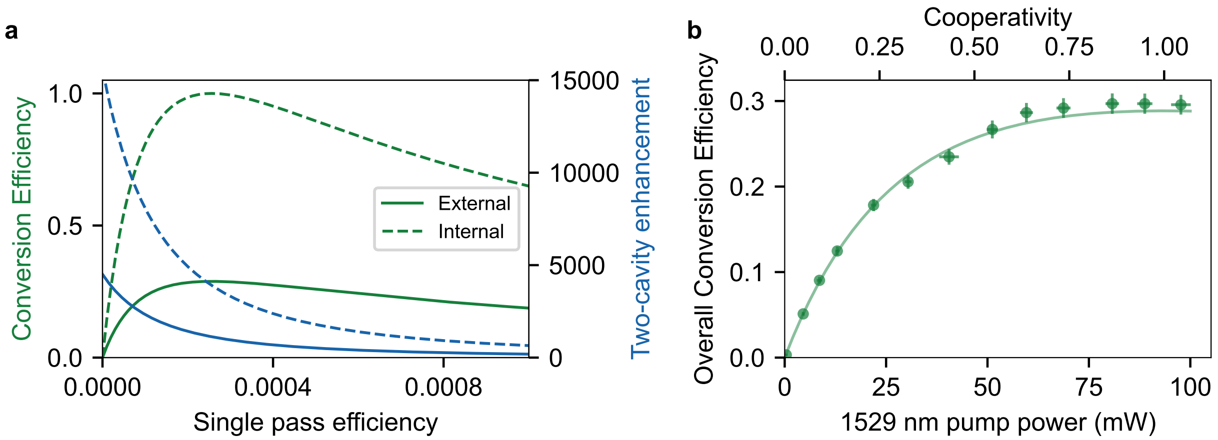

Figure 5.6: 780 nm → 516 nm end-to-end conversion efficiency. The cooperative enhancement at the input and output modes can be utilized for optical transduction. The maximum end to end conversion efficiency is measured to be 30(1)%. Shown is the numerical simulation (a) and data (b) with a one-parameter fit (Sec 5.3.3). The maximum external efficiency for fixed external and internal losses is reached when the internal efficiency reaches unity, at $\mathcal{C} = 1$. The major source of error in the experiment were drifts of the input laser power. Note that a higher transmission cavity outcoupler (details in text) was used in this measurement for better impedance matching, with $\{\kappa_{\mathrm{DF}}, \kappa_{\mathrm{SF}}\} = 2\pi \times \{5.3(2), 12.3(6)\}$ MHz. Also note that the data and theory here present the conversion efficiency when the input frequency is at bare DF resonance.

at perfect alignment should increase g. We did not characterize the alignment of our pump beam with respect to the crystal, but did observe a greater g for this section of the experiment for a given pump power ($\sim 2\pi \times 5$ MHz at ~ 100 mW compared to $\sim 2\pi \times 5$ MHz at ~ 200 mW for the avoided-crossing experiment). The powers at 780 nm and 516 nm are measured using a NIST/PTB calibrated Thorlabs S120C sensor after bandpass filters at the respective wavelengths.

The optical pump can be thought of as modulating the cavity's optical path length at $c/\lambda_{\mathrm{pump}} = 196$ THz, generating a frequency sideband at 516 nm. The crystal's periodic poling can be seen as a spatial analog of serrodyne [93] modulation, providing a frequency sideband on just one side of the carrier. More significantly, this cavity modulation and the consequent frequency shifting is Purcell- enhanced or suppressed by tuning the DF and SF frequencies into or out of resonance with the cavity modes using the pump frequency.

Figure 5.6 shows the measured conversion efficiency at different pump powers and values of $\mathcal{C}$, with a maximum conversion efficiency of 30(1)%. For fixed external and internal losses, the maximum efficiency is reached when $\mathcal{C} = 1$. In terms of cavity finesses $\mathcal{F} = \nu/\kappa$, $\mathcal{C}$ is equal to $4\epsilon\mathcal{F}_{\mathrm{DF}}\mathcal{F}_{\mathrm{SF}}$, demonstrating that the 'internal' conversion efficiency [53] $4\mathcal{C}/(1+\mathcal{C})^2$ quickly approaches unity because of the $\mathcal{O}(10^4)$ enhancement of the single-pass conversion efficiency ϵ by the two cavities. The external conversion efficiency stops increasing after $\mathcal{C}$ reaches one because the photon extraction rate, dependent on outcoupler transmission, fails to keep up with the increasing internal coupling rate. The latter manifests as the splitting in the spectrum because the occupation in the cavity modes begins to oscillate with frequency $2g$ as seen in Figs 5.4b and 5.5.

The data shown in figure 5.6 is fit to equation 5.4, using κ_i^{ext} values from mirror coating specifications and κ_i values from avoided-crossing data for the cavity with a higher transmission outcoupler. A single fit parameter was used to account for the frequency-dependent variation in single-pass conversion efficiency at equal pump powers (as discussed in Sec 5.4.1, figure 5.3(c)). The fit suggests an 84% difference in single-pass efficiency for a frequency difference of ~ 600 MHz, which is within the range of measurements shown in figure 5.3(c).

In the current experimental setup, the end-to-end conversion efficiency is limited by the spatial overlap of pump and cavity modes, our choice of coupling mirror specifications, and ultimately, the intrinsic losses of the cavity (excluding in- and out-coupling) at the two wavelengths, quantified by $\kappa_{\mathrm{DF}}^{\mathrm{int}}$ and $\kappa_{\mathrm{SF}}^{\mathrm{int}}$. We discuss estimated improvements later in the chapter.

5.7 Spatial-mode coupling across frequencies

The coupling g between two frequency modes includes a dependence on the spatial overlap of the pump and cavity modes $\int_{V_{\mathrm{crystal}}} E_{\mathrm{SF}}^{*}(\vec{r}) E_{\mathrm{pump}}(\vec{r}) E_{\mathrm{DF}}(\vec{r}) dV$ over the crystal volume. When the pump is not perfectly mode-matched due to suboptimal waists or misalignment, this can lead to overlap with, and hence, coupling to higher-order transverse modes of the cavity. However, the conversion to higher-order modes is Purcell suppressed via transverse mode non-degeneracy of the cavity, making the system more tolerant to small mismatches in mode-waists and misalignment of the pump. The reduction in coupling into the target mode can be offset via increased pump power.

In the presence of spatial overlap with higher order modes, the pump frequency can be varied to obtain cavity enhancement of coupling between different spatial modes at the sum- and difference- frequencies. Fig 5.7 shows the mode profile of some other converted higher order modes of the 516 nm cavity. As an example, Fig 5.8 demonstrates coherent coupling between a DF fundamental Gaussian (HG_{00}) mode and the spatially-orthogonal SF HG_{10} mode, achieved by tilting the pump beam with respect to the cavity axis and varying the pump frequency to be resonant with the SF HG_{10} mode. For higher coupling to targeted spatial modes, the pump can be beam shaped for more spatial overlap. The mode profile of the output is expected to be of high quality, as the output is spatially filtered by the cavity.

Figure 5.7: Coupling to higher order modes When the pump is not completely mode-matched, and the frequency of the pump is varied, we couple the fundamental Gaussian mode of the 780 cavity to higher-order modes of the 516 nm cavity.

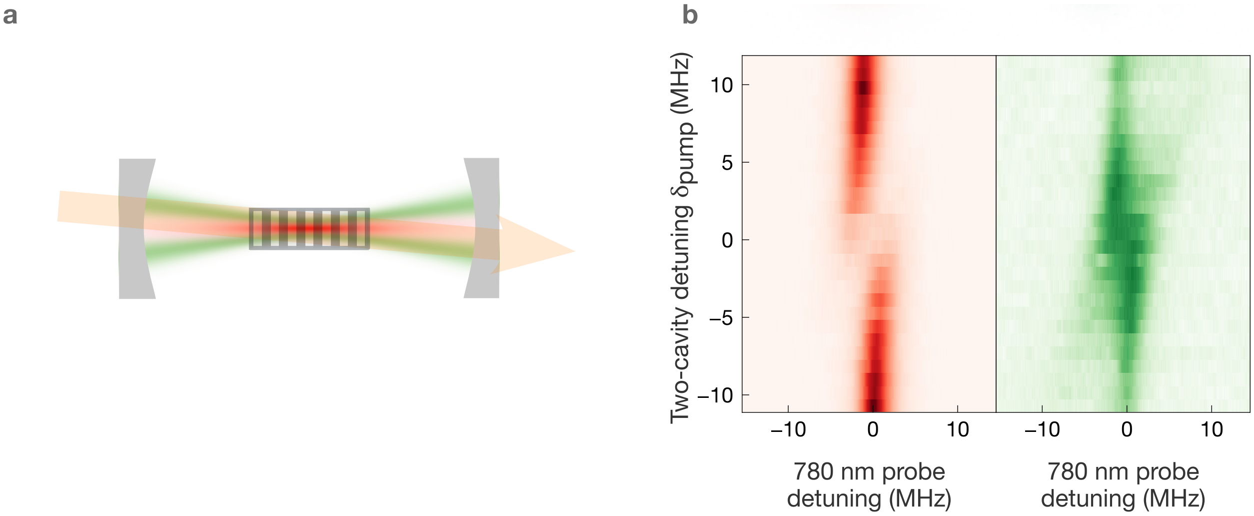

Figure 5.8: Coupling orthogonal spatial modes across frequencies. (a) The cavity length is stabilized to the DF HG_{00} mode and the pump frequency is set to be resonant with SF HG_{10} mode. The pump misalignment bridges the spatial orthogonality of the two modes. (b) Avoided crossing in the transmission spectrum at DF (left, red) and SF (right, green) when probed with DF, corresponding to $g = 2\pi \times 2.7(1)$ MHz at ∼200 mW of pump power. The coupling could be made stronger with spatial shaping of the pump.

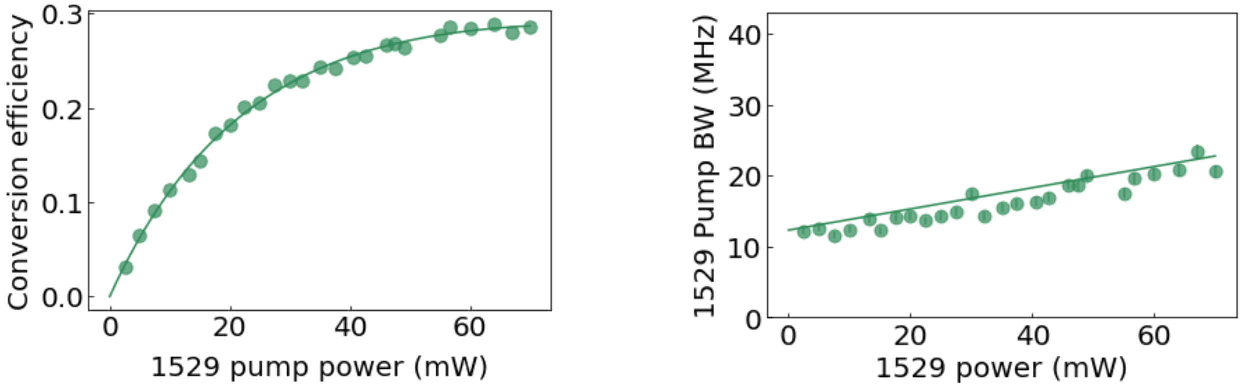

(a) (b)

Figure 5.9: Measurement of pump bandwidth (a) Conversion efficiency data corresponding to the pump bandwidth measurement. The fit has an additional fit parameter compared to Fig 5.6 corresponding to optical loss due to a lossy lens in this iteration of the experiment. (b) The pump bandwidth is deduced by scanning the pump frequency and fitting the converted 516 nm profile to a Lorentzian. The linear curve is a theory curve plotted using parameters derived from avoided crossing and conversion efficiency measurements.

5.8 Estimated improvements

A gain in cooperativity is expected from optimizing pump- and cavity waists at the crystal to increase the single-pass efficiency. From the model presented in appendix A.8, we find that the optimal point of operation is when $L_{\text{crystal}}/2z_R = 2.84$, where z_R is the Rayleigh range of the cavity mode/pump beam. This is consistent with the theoretical extension of the Boyd-Kleinman theory for non-resonant SFG by Guha et al [94], where the maximum spatial overlap between the pump and the input, and the maximum single pass efficiency is ensured at $L_{\text{crystal}}/2z_R = 2.84$ in the absence of walk-off. Optimizing the pump waist in our current setup to 20 μm and designing a running-wave cavity [95–97] or a small-waist cavity [32] (see chapter 7) with a waist of ~ 14 μm is expected to provide an enhancement of a factor of ~ 15 in the single-pass conversion efficiency (Figs 5.10(a) and 5.10(b)).

For frequency-conversion with the current internal cavity losses, increasing the outcoupler transmission and pump power can provide higher efficiencies (Fig 5.10(b)). In addition, exploring lower-loss nonlinear materials could be useful. Experiments with intracavity undoped

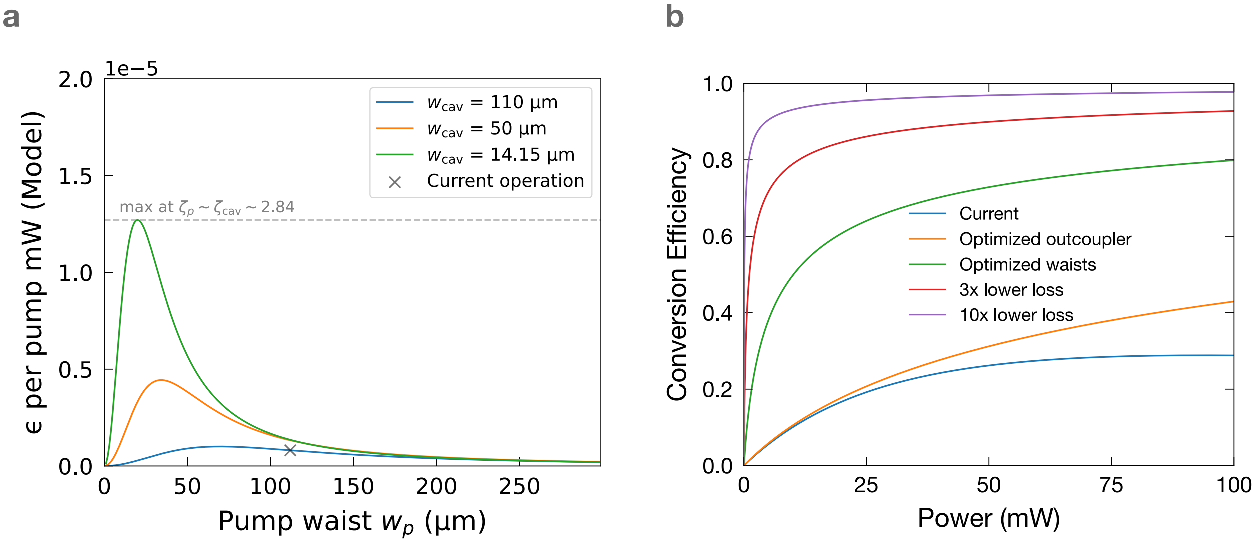

Figure 5.10: Expected improvements (a) Calculation for the single-pass efficiency per mW of pump power for the pump and input beam sizes for the current cavity design (with 780 nm cavity waist ∼110 μm at DF), intermediate waist (∼50 μm) and optimal waist (∼14 μm). The maximum is obtained when the parameters ζ of the cavity and the pump are equal to 2.84, where $\zeta = L_{\text{crystal}}/2z_R$ and z_R is the Rayleigh length of the pump and the cavity. The calculations are done for 1 mW of pump power. (b) Expected end-to-end conversion efficiency in different scenarios. Blue: fit corresponding to data in main text Fig 5.6b. Orange: with optimized outcouplers with the current crystal and cavity/pump waists. Green: with optimized waists and outcouplers with the current crystal. Red: with optimized waists and outcouplers and 3x lower losses at both SF and DF. Purple: with 10x lower losses at both SF and DF.

lithium niobate have provided limiting cavity finesse of 9900 (chapter 7). The crystal length was 3 mm (Manufacturer: Castech), suggesting an absorption loss of 0.001 per cm. Measurements of congruently grown lithium niobate suggest losses as low as 0.0004 per cm [98] at 780 nm, suggesting a 10x gain in cooperativity from lower losses at 780 nm. Moving to telecom wavelengths from 516 nm would provide a further gain in cooperativity due to lower losses in lithium niobate in the telecom frequency range. One possible combination is 1570 nm as the pump, and 1550 nm and 780 nm as the difference- and sum- frequencies.

Other crystals, such as potassium titanyl phosphate (KTP), exhibit lower absorption losses than lithium niobate (LN). However, due to their lower electro-optic coefficients (around half of LN for KTP), they require a longer interaction length. After accounting for the length, ppKTP should provide a factor of ∼7 improvement in loss over 5%-MgO doped LN at 780 nm, but evaluates to comparable overall losses as compared to congruent LN (Loss of ppKTP at 775 nm has been measured to be ∼127 ppm per cm [99], ∼3435 ppm per cm for 5%-MgO doped LN [100] and 400 ppm per cm for congruently grown LN [98]).

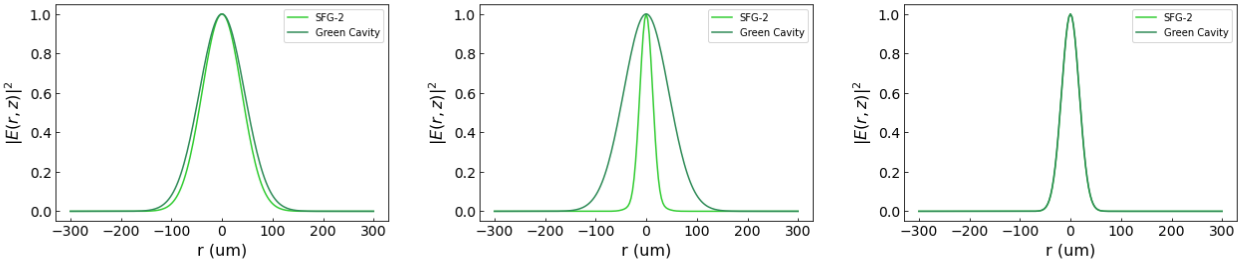

(a) (b) (c)

Figure 5.11: Comparing overlap of spatial mode profiles of the 516 nm cavity mode and the free space SFG output at 516 nm at different beam waist configurations at the output face of the crystal: (a) Current waist configuration. The mode profiles and hence the overlap stays the same throughout the length of the crystal because of a large waist/rayleigh range compared to the length of the crystal, (b) Waist configuration at the maxima of blue curve in figure 5.10a. The overlap and mode profiles vary significantly over the length of the crystal, and (c) optimal waist (peak of green curve in figure 5.10a). The spatial mode profile varies throughout the length of the crystal but the overlap is nearly equal to 1 throughout. The beam profiles are calculated based on the integrals provided in reference [94]

5.9 Discussion

In this work, we have demonstrated optically controlled, strong coupling between two cavity modes using an intracavity $\chi^{(2)}$ crystal, yielding Floquet eigenmodes that exist at two wavelengths simultaneously. Using the platform, we have presented a new approach to frequency conversion with low pump powers, reduced sensitivity to alignment and waist optimization, and negligible fiber-converter coupling losses due to near-perfect mode-matching of the input with the cavity mode. By misaligning the pump, we have also demonstrated coupling between near-orthogonal spatial modes at two frequencies, adding more versatility by extending control to the spatial dimension.

Looking ahead, we expect that improvements to the scheme such as utilizing lower-loss congruent ppLN [98, 100] for cavity coupling, and redesigning the cavity for optimal waists for the pump beam and the cavity modes, could increase the cooperativity $\mathcal{C}_{\max}$ by a factor of >50 (SI 5.8), enabling faster coupling between modes, yielding higher cooperativity and higher conversion efficiencies at lower pump powers.

More broadly, this work opens the door to cavity QED experiments with multiple atomic species [101, 102] for gate and memory architectures [103, 104], and developing quantum interconnects for atomic platforms [97, 105, 106]. In conjunction with experiments deploying cavities with small waists for readout of atoms and atom arrays [32, 95, 97], this platform could enable fast, optically-switchable readout to telecom wavelengths. The spatial control across frequencies could be useful for simultaneous trapping of ground state and Rydberg state atoms [107, 108], and increased channel capacity for communication through few-mode optical fibers [109] and free-space [109–113]. Beam-shaping of the pump can also enable fast, optically-generated local potentials for cavity photons [114]. Finally, the coupled mode cavity could enable new protocols for state preparation and transfer [115–117].

Coupling with atoms

Optically controlled tunable outcoupling

The improvement in single-pass conversion efficiency via pump and input cavity waist optimizations coupled with improvement in material losses should get us to a regime where we can use a singly resonant cavity at the input wavelength, and vary its outcoupling by varying the pump power. Figure 5.12 shows the variation in finesse (numerical simulation) depending on the single pass efficiency in the accessible regime at similar pump powers with optimized waists. This could enable direct readout to telecom wavelengths.

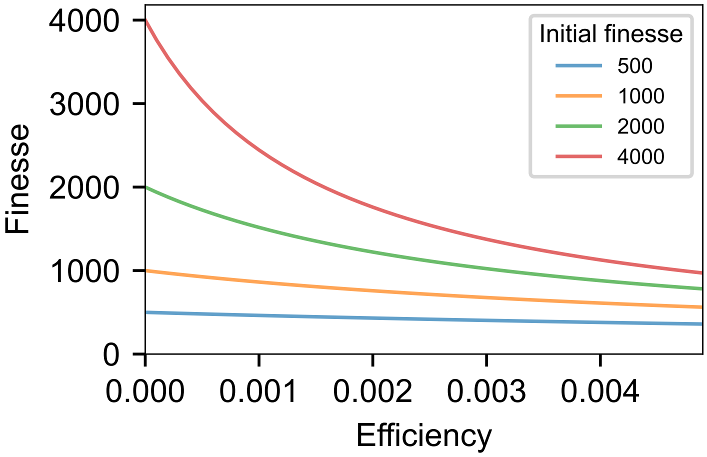

Figure 5.12: Tunable finesse in a singly resonant cavity

Figure 5.13 shows numerical simulations using master equations for the evolution of populations of the combined two-cavity and atomic states for different coupling and loss parameters. For Rubidium, for instance, the conversion to the other mode is mostly limited by the atomic lifetime, and the cavity losses seem to make a difference only at sufficiently high single atom cooperativities.

Taking inspiration from tunable finesse in coupled cavities from reference [90], we can also coupled the nonlinear crystal cavity to an atomic cavity and optically control the leakage of the atomic cavity for controllable readout.

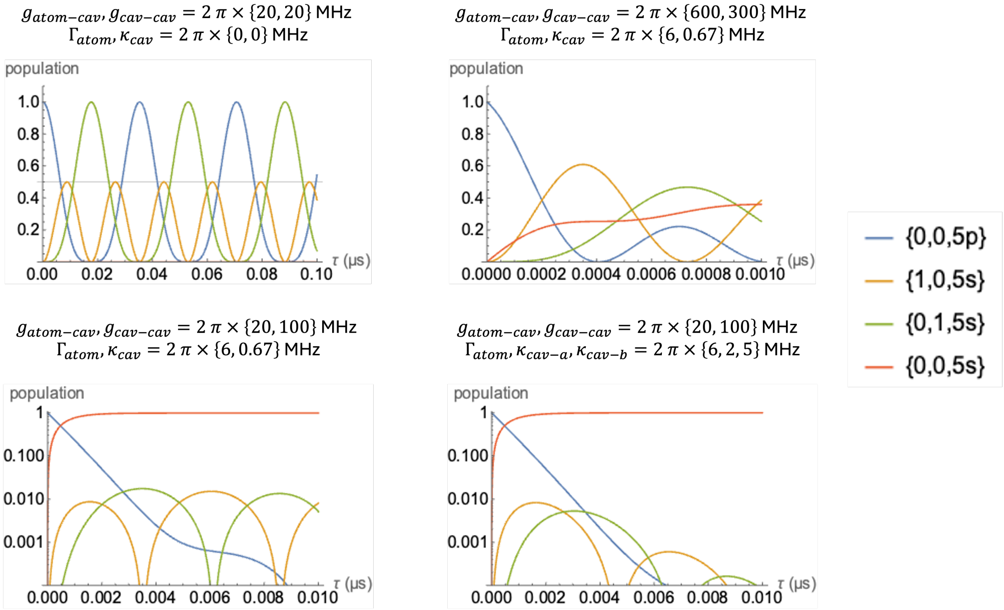

$g_{atom-cav}, g_{cav-cav} = 2\pi \times \{20, 20\}$ MHz
$\Gamma_{atom}, \kappa_{cav} = 2\pi \times \{0, 0\}$ MHz

$g_{atom-cav}, g_{cav-cav} = 2\pi \times \{600, 300\}$ MHz
$\Gamma_{atom}, \kappa_{cav} = 2\pi \times \{6, 0.67\}$ MHz

$g_{atom-cav}, g_{cav-cav} = 2\pi \times \{20, 100\}$ MHz
$\Gamma_{atom}, \kappa_{cav} = 2\pi \times \{6, 0.67\}$ MHz

$g_{atom-cav}, g_{cav-cav} = 2\pi \times \{20, 100\}$ MHz
$\Gamma_{atom}, \kappa_{cav-a}, \kappa_{cav-b} = 2\pi \times \{6, 2, 5\}$ MHz

Figure 5.13: Calculations with a single-atom inside the cavity. The states are defined as $\{n_1, n_2, s\}$, where n_1 is the number of photons in the 780 nm mode, n_2 is the number of photons in the 516 nm mode and 5s(5p) are the ground(excited) states of the atom. Note that the last two plots are on a log scale.

Chapter 6

Transduction with two cavities and a three-level mediator

6.1 Introduction

This chapter provides a brief comparison between the two transduction schemes discussed in Chapters 3, 4 and 5. It is worth noting that in the millimeter-wave-optical transduction scheme, the Rydberg dressing of the ground state with the 297 nm UV laser reduces the four-level system to an effective three-level system, allowing the atomic scheme to be modeled as transduction mediated by a three-level system coupled to two cavity modes.

Figure 6.1 illustrates a three-level system with ground state $|G\rangle$, intermediary excited state $|E\rangle$, and a second excited state $|R\rangle$. The transitions $|G\rangle \leftrightarrow |E\rangle$ and $|G\rangle \leftrightarrow |R\rangle$ are detuned from ω_{in} and ω_{out} by δ_E and δ_R, respectively. Two cavity modes, described by a and b, have detunings δ_a and δ_b relative to ω_{in} and ω_{out}. A classical pump with Rabi frequency Ω_{pump} couples the $|E\rangle$ and $|R\rangle$ states. The corresponding Hamiltonian is

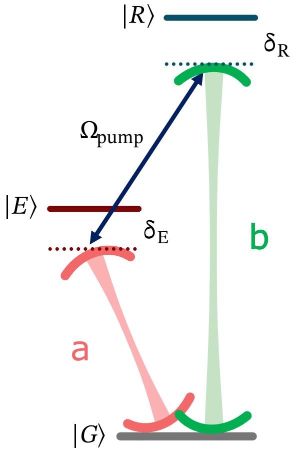

Figure 6.1: **Two cavities coupled to a three-level system.** In the millimeter-wave to optical transduction, the internal states involved are collective states of the entire participating atomic ensemble and the transduction occurs close to resonance to the transitions. For the nonlinear crystal, the states comprise the continuum of states of the crystal – operating far from resonance allows us to abstract out the exact levels and rely on macroscopic quantities like the $\chi^{(2)}$ coefficient to calculate the coupling rate of interest.

$$\begin{aligned} H &= H_o + H_{int} \\ H_o &= \delta_a a^\dagger a + \delta_b b^\dagger b + \delta_e E^\dagger E + \delta_r R^\dagger R \\ H_{int} &= G_a a E^\dagger + \Omega_p R^\dagger E + G_b b^\dagger R + h.c. \end{aligned} \tag{6.1}$$

Here, E and R are bosonic annihilation operators representing collective excitations of states $|E\rangle$ and $|R\rangle$, while G_a and G_b denote the collective coupling strengths of the atomic system to the cavity modes a and b, respectively. For the crystal scheme, the collective state is trivially constructed for one atom.

6.1.1 Resonant versus far off-resonant atomic interaction

During the operation of the millimeter-wave transducer, there is always some population in the excited Rydberg levels, making it a non-parametric process, ie, there is an active exchange of energy with the mediator. To a very good approximation, the transducer can be described by a beamsplitting Hamiltonian between the millimeter-wave cavity and the dark-polariton:

6.1.1.1 Near-resonant case in atomic scheme: Beamsplitter between dark polariton and mmwave cavity

The transducer when operated at two-photon Rydberg resonance operates at the dark polariton resonance. In the limit where the bright polaritons are well separated in energy from the dark polariton (when $C_{\text{opt}} \gg 1$), the millimeter-wave cavity couples only to the dark-polariton state. The operators a, E and R can be written in the polariton basis as

$$\begin{aligned} a &= \frac{1}{\sqrt{2}}(B_+ + B_-)\sin(\theta_D) + D\cos(\theta_D) \\ E &= \frac{1}{\sqrt{2}}(B_+ - B_-) \\ R &= \frac{1}{\sqrt{2}}(B_+ + B_-)\cos(\theta_D) - D\sin(\theta_D) \end{aligned} \tag{6.2}$$

where D and $B_\pm$ are the dark polariton and bright polariton destruction operators, and $\theta_D = \tan^{-1}(G_{opt}/\Omega)$. Substituting relations 6.2 in the linearized Hamiltonian for the transducer at resonance: $H_{lin} = g_{opt}\sqrt{N}\hat{a}E^\dagger + \Omega_b E R^\dagger + g_{mm}\frac{\sqrt{N}\Omega_{uv}}{\Delta}\hat{b}^\dagger R + h.c.$[1], and projecting the Hamiltonian onto the dark-polariton manifold to ignore the effect of the off-resonant bright polaritons, yields

$$P_D H_{lin} P_D = \left(-\sqrt{N} g_{mm}\sin\theta_D \frac{\Omega_{uv}}{\Delta} b^\dagger D + h.c.\right) \tag{6.3}$$

While in our operating regime we could observe a small effect of coupling to the bright polaritons, this approximate analysis highlights the active participation of the mediator in the transduction process. In this case, if we were to write an effective $\chi^{(2)}$ for the atomic transducer it would contain imaginary terms corresponding to absorption processes induced by the pump by excitation of lossy excited levels. It is noteworthy that despite the absorption

---

[1] We identify G_a in equations 6.1 with $g_{opt}\sqrt{N}$, Ω_{pump} with Ω_b, and G_b with $g_{mm}\frac{\sqrt{N}\Omega_{UV}}{\Delta}$.

term, it is possible to get high conversion efficiencies by making the good rates (pump Rabi frequency, G's of cavities) dominate the loss rates (Γ_R) such that the coupling/conversion occurs before the lossy absorption kicks in (impedance matching, discussed in chapter 3 and again in section 6.1.6).

6.1.1.2 Far off-resonant case in crystal cavity: Beamsplitter between two cavity modes

Here we derive the Hamiltonian for the $\chi^{(2)}$ crystal-coupled cavity modes starting from a three-level system. Invoking the Heisenberg-Langevin equations for the Hamiltonian in equation 6.1, we can write (similar to the derivation in chapter 3, equations 3.2):

$$\dot{a} = (i\delta_a - \frac{\kappa_a}{2})a - iG_aE + \sqrt{\kappa_a^{\text{ext}}}a_{in} \tag{6.4}$$

$$\dot{E} = (i\delta_E - \frac{\Gamma_E}{2})E - iG_aa - i\Omega_pR \tag{6.5}$$

$$\dot{R} = (i\delta_R - \frac{\Gamma_R}{2})R - i\Omega_pE - iG_bb \tag{6.6}$$

$$\dot{b} = (i\delta_b - \frac{\kappa_b}{2})b - iG_bR + \sqrt{\kappa_b^{\text{ext}}}b_{in} \tag{6.7}$$

Non-linear processes are typically far-detuned from the internal states of the crystal, allowing us to adiabatically eliminate the upper states of the mediator by setting equations 6.5 and 6.6 to 0. Using the expressions for E and R obtained from this step, we get an effective coupling between a and b reducing the Hamiltonian to

$$H_{int} = g(a^\dagger b + ab^\dagger) \tag{6.8}$$

$$\text{where } g = \frac{G_aG_b\Omega_p}{\delta_E\delta_R} \tag{6.9}$$

Thus, the crystal cavity, as we already saw in the previous chapter, can be described by a beamsplitting Hamiltonian between the two cavities. There is no active exchange of energy with the atoms, neither an occupation in the excited states of the atoms in the crystal. The $\chi^{(2)}$ is real and frequency insensitive in a large region and can be determined from a macroscopic measurement.

6.1.2 Losses

Low losses are desirable in any quantum platform. In transduction based applications, it is particularly critical to preserve as much quantum information encoded in single photons and prevent it from being read by the universe via loss channels.

Atomic scheme: Spontaneous emission from the excited states is the primary concern for loss. For the atomic scheme, the losses are overcome by using Rydberg states which have long lifetimes[2], and a cavity Rydberg electromagnetically induced transparency (EIT) scheme that interferometrically eliminates any population in a dissipative low-lying excited state.

Crystal scheme: For the crystal, the loss sources could be both spontaneous emission and other scattering losses arising out of the complex structure. In the crystal scheme, those losses are conveniently avoided by operating far from any resonances. The crystal cavities are more susceptible to losses owing to the presence of impurities in the macroscopic crystal, which impacts the cooperativity. Chapter 7 discusses losses with macroscopic intracavity optics in more detail.

6.1.3 Dipole selection rules

In a system with inversion symmetry, the $|R\rangle \rightarrow |G\rangle$ transition should be dipole forbidden if the two-photon transition $|G\rangle \rightarrow |E\rangle \rightarrow |R\rangle$ is dipole allowed, and vice versa. In the classical non-linear optics description, this is equivalent to saying that the second-order

---

[2] Combined with dephasing, the linewidth of collective Rydberg states still have an impact on the cooperativities as discussed previously.

nonlinear response (or $\chi^{(2)}$) vanishes in the presence of inversion symmetry ([72]). Both the platforms involve inversion symmetry breaking to allow for the dipole transition. In the case of ^{85}Rb atomic ensemble, the symmetry is broken by the UV dressing[3] which mixes state $|G = 5S\rangle$ with state $|35P\rangle$. In the case of the crystal, the inversion symmetry breaking comes from the arrangement of atoms in the crystal lattice.

6.1.4 Cooperative enhancement

The interaction of a cavity mode with an ensemble of atoms scales the coupling g by a factor of $\sqrt{N}$, where N is the number of atoms in the ensemble. This cooperative enhancement follows from the fact that the cavity mode couples with symmetric Dicke states of the entire ensemble, inducing a coherence across the atomic cloud (Appendix A.2). In the case of the near-resonant atomic transducer with $N \approx 600$, we get enhancement factors of $\sqrt{N \cos^2 \theta}$ and $\sqrt{N \sin^2 \theta}$ at the optical and millimeter-wave transition, where $\tan \theta$ is the UV dressing fraction.

A far off-resonant transduction scheme will typically require a much higher collective enhancement via a larger number of mediators due to weaker participation away from resonance. The macroscopic crystal employs on the order of 10^{23} atoms that interact non-uniformly with the cavity mode as they are spread over a macroscopic volume. The coupling g between the two modes is proportional to the total number of atoms N, which shows up through the $\chi^{(2)}$ coefficient in the single pass efficiency, or equivalently, through the product of individual cavity couplings when equation 6.9 is evaluated for all mediators within the crystal.

---

[3] The UV dressing is primarily required for energy and momentum conservation. The state mixing justifies modeling the transducer as a dipole-allowed three-wave mixer.

6.1.5 Phase matching

Due to the involvement of different wavelengths and wavelength-dependent refractive index of matter, the propagation length over which phase coherence is preserved between different fields is very short, leading to destructive interference of generated fields. In the atomic scheme, the cloud is sufficiently dilute to assume the refractive index to be unity at the wavelengths of interest. In the crystal, phase matching is ensured by periodic poling and fine-tuned (to some extent) via temperature and angle-tuning. The platform is robust to small mismatches as the cooperative enhancement can offset, at the cost of pump power, the decrease in single pass efficiency.

6.1.6 Impedance matching

The atomic and crystal schemes can be termed as stage-1 and stage-0 transduction schemes respectively, due to the number of internal couplings involved [53]. The requirement to matching different coupling rates in the system is key to getting high conversion efficiencies in an otherwise leaky system.

In the case of the atomic transducer, due to the active involvement of the atomic levels, impedance matching is required even in the absence of cavity losses to balance the three rates of coupling cavity photons to atoms, leading to the impedance matching condition of

$$C_a = C_b = \sqrt{1 + C_p} \tag{6.10}$$

The overall conversion efficiency is obtained by scaling the internal conversion efficiency by an additional factor of $\frac{\kappa_{\mathrm{a}}^{\mathrm{ext}}}{\kappa_{\mathrm{a}}}\frac{\kappa_{\mathrm{b}}^{\mathrm{ext}}}{\kappa_{\mathrm{b}}}$.

In the crystal cavity, in the absence of internal cavity losses, no rate matching is required – the external conversion efficiency ($\frac{\kappa_{\mathrm{a}}^{\mathrm{ext}}}{\kappa_{\mathrm{a}}}\frac{\kappa_{\mathrm{b}}^{\mathrm{ext}}}{\kappa_{\mathrm{b}}}\eta_{int}$) is equal to the internal conversion efficiency ($\eta_{int} = \frac{4C}{(C+1)^2}$) and a cooperativity of 1 ensures perfect conversion. However, in the presence

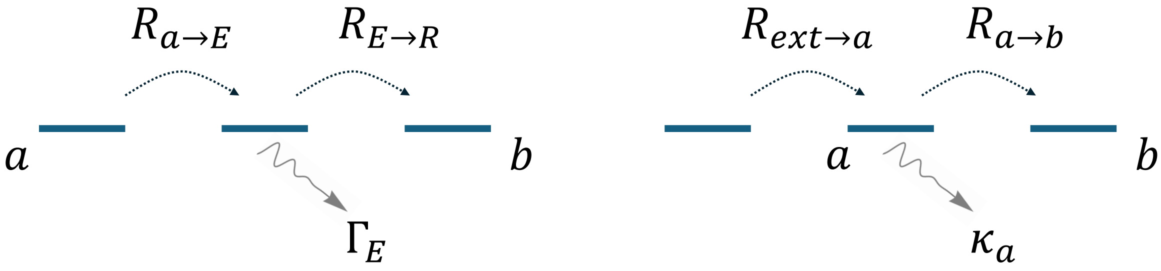

Figure 6.2: **Interpreting impedance matching conditions for a → b direction of transduction.** Left: Stage 1 impedance matching. Right: Stage 0 impedance matching

of losses, one has to match the rates of incoupling and outcoupling into the cavity to the rates of coupling to the other cavity, giving rise to impedance matching conditions very similar to the atomic transducer:

$$\frac{\kappa_{\mathrm{a}}^{\mathrm{ext}}}{\kappa_{\mathrm{a}}^{\mathrm{int}}} = \frac{\kappa_{\mathrm{b}}^{\mathrm{ext}}}{\kappa_{\mathrm{b}}^{\mathrm{int}}} = \sqrt{1+\mathcal{C}_{\mathrm{max}}}, \tag{6.11}$$

where $\mathcal{C}_{\mathrm{max}} = 4g^2/\kappa_{\mathrm{a}}^{\mathrm{int}}\kappa_{\mathrm{b}}^{\mathrm{int}}$, is the cooperativity in the absence of any leakage through the mirrors. The ratios of the external coupling and internal linewidths function in a manner similar to the millimeter-wave and optical cooperativities in equation 6.10 in the sense that they are the ratios of the good coupling rates to the bad coupling rates. Note that in the crystal based transduction scheme, the impedance-matching condition maximizes the *overall* conversion efficiency, while in the case of the atomic ensemble transduction, a similar condition maximizes the internal conversion efficiency.

Chapter 7

Intracavity optics

Introduction

As discussed in Chapter 2, the figure of merit for a cavity – the finesse $\mathcal{F}$ – scales inversely with the losses in the cavity. Inserting a macroscopic optical component within the cavity becomes a dangerous endeavour, as it can introduce large losses that can lower the finesse significantly. At the same time, these optics can make the cavities more versatile. We already saw a glimpse in Chapter 5, with the use of an intracavity ppLN to generate two-color cavity modes.

In this chapter, we will begin with an analysis of the limiting loss mechanisms – absorption, reflection, and scattering from surface irregularities – and discuss how material choice and coatings can mitigate these effects. We then explore cavity configurations that replace traditional curved mirrors with intracavity lenses, enabling astigmatism correction for non-planar cavity designs and small mode waists for high single-atom cooperativity. Then, we present a method for scaling to arrays of cavities via microlens arrays. We then discuss high-bandwidth modulation and stabilization of cavities using intracavity electro-optic crystals and RF techniques.

7.1 Loss considerations

Table 7.1 summarizes the limiting finesses enabled by intracavity optics in the discussed experiments. For intracavity optics, the major sources of loss are: (1) absorption, (2) surface reflection, and (3) scattering due to surface roughness.

Material	**Limiting finesse**	**Extracted round-trip loss**
Superpolished lenses (2x)	18000	<0.02% per optic
Lenses (2x)	11000	<0.03% per optic
Lenses (1x)	17000	<0.04%
Lithium niobate (3 mm)	9900	0.06%
5% MgO-doped Lithium niobate (10 mm)	1000	0.63%
Thorlabs microlens array (ML300-AR)	430	1.46%
Patterned end mirror	>1000	<0.63%

Table 7.1: A summary of approximate limiting finesses enabled by intracavity optics in experiments presented in the thesis.

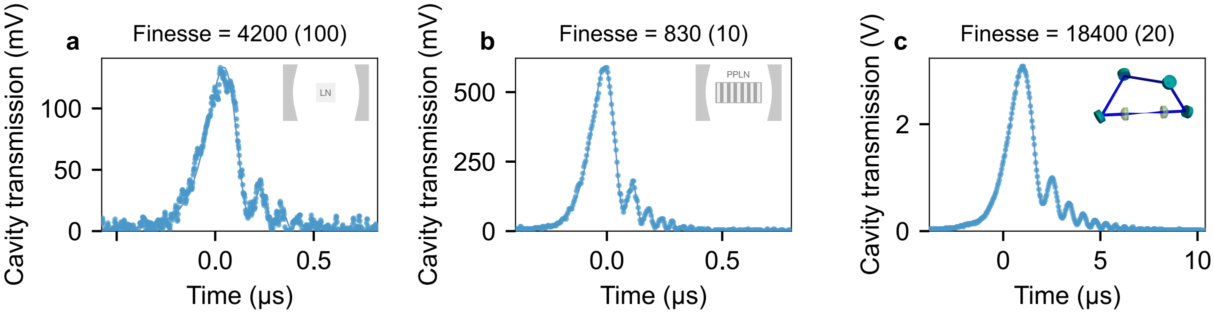

Figure 7.1: Ringdown measurements for cavity finesse [92] (a) A resonator with 3 mm long lithium niobate crystal with a finesse of 4200 (limiting finesse: 9900). (b) A loss-dominated resonator with a 10 mm long periodically poled lithium niobate (ppLN) with a finesse of 830 (limiting finesse: ∼1000). (c) A resonator with two lenses and a finesse of 18400 ([96])

7.1.1 Bulk absorption loss

Absorption losses in intracavity optical elements can originate from absorption from impurities and internal scattering. In glasses, internal scattering may arise from the glass matrix, or structural inhomogeneities such as the presence of bubbles. Among commonly used optical glasses, fused silica (FS) exhibits low absorption and scattering, enabling high finesse; for instance, a finesse of 18,400 was observed with two FS lenses (figure 7.1c). FS performs well across most of the visible and near-infrared spectrum, except for an hydroxyl (OH) absorption band near 1.4 µm. In contrast, N-BK7 is less suitable for high-finesse cavities due to an absorption loss of <0.002 per cm [118].

Losses in lithium niobate (LN) primarily arise from impurities and generally decrease from the visible (VIS) to the near-infrared (near-IR) [98, 100]. We measured a limiting finesse of 9900 for a 3 mm long congruent LN crystal and 1000 for a 10 mm long 5% MgO-doped periodically poled crystal. The optical losses in LN can vary significantly between samples, as neither doping nor periodic poling should, in principle, introduce additional loss mechanisms, although studies show that congruent lithium niobate performs better than doped lithium niobate [98, 100].

Other crystals, such as potassium titanyl phosphate (KTP), exhibit lower absorption losses than lithium niobate (LN). However, due to their lower electro-optic coefficients (around half of LN), they require a longer interaction length, which *might*[1] lead to comparable overall losses for typical applications.

7.1.2 Surface reflection loss

In a standing-wave cavity, any optical element introduces four additional surfaces, with reflections from each contributing to round-trip losses. The magnitude of these losses depends on the material's refractive index, as described by the Fresnel reflection coefficient:

$$R = \left(\frac{n-1}{n+1}\right)^2 . \tag{7.1}$$

---

[1] Loss of ppKTP at 775 nm is ~127 ppm per cm [99], ~3435 ppm per cm for 5%-MgO doped LN [100] and 300 ppm per cm for congruently grown LN [98]. The dielectric coefficient for KTP is about half of that of LN. The conversion efficiency is proportional to $(d_{\text{eff}})^2 \times L_{\text{crystal}}$ for conversion with Gaussian beams [94].

assuming normal incidence from air/vacuum. For high-index materials, reflection losses can be significant. For instance, lithium niobate (LN) ($n = 2.2$) results in approximately 14% loss per interface, while ultraviolet-grade fused silica (UVFS) ($n = 1.5$) incurs about 4% per interface. Such losses can severely impact cavity finesse and stability due to mode hybridization.

Ion-beam sputtering (IBS) coating processes enable high-quality anti-reflective (AR) coatings, achieving reflectivities as low as $R = 250$ ppm, with coating-induced losses below 10 ppm. Interestingly, we observed cavity finesses exceeding expectations based on coating specifications (250 ppm limits finesse to ~6000). Two possible explanations for this discrepancy are: (1) the coatings outperform their specified performance, or (2) reflected light is spatially mode-mismatched, hence Purcell-suppressed and forced to remain within the desired cavity mode. The latter mechanism, however, is not reliable; in the presence of mode-mismatched higher-order degenerate modes, it can lead to unwanted Purcell-enhanced coupling to those modes and resulting cavity instabilities.

For temperature-sensitive optics, such as periodically poled lithium niobate (ppLN), it is also essential to consider the temperature dependence of coating performance, as thermal variations may impact optical losses and cavity behavior.

7.1.3 Surface roughness

Surface irregularities in optical elements can scatter light out of the cavity, thereby reducing the achievable finesse. Various metrics are used to characterize surface irregularities at different spatial scales [119, 120], including the U.S. Navy's scratch-dig standard, which compares scratches to predefined reference sizes, wavefront deformation measurements relative to the optical wavelength, and root-mean-square (RMS) surface roughness, which captures small-scale irregularities.

While macroscopic defects impact the finesse on a coarse level, RMS roughness (σ) is crucial in determining scattering losses in high-finesse systems. The estimated scattering loss due to surface roughness is given by [119]:

$$R = R_0 \exp\left(-\frac{(4\pi\sigma)^2}{\lambda^2}\right), \tag{7.2}$$

where R_0 represents the initial reflectivity of the optical surface.

Magnetorheological finishing (MRF) can typically achieve surface roughness below 2 Å, and superpolished surfaces with roughness below 0.5 Å are also attainable. Notably, ion-beam sputtering (IBS) coatings preserve the RMS surface roughness of the underlying substrate, ensuring that the benefits of superpolishing are retained. With the currently available technologies, the surface roughness specification affects the finesse on a similar scale to AR coatings.

In addition to loss outside the cavity, both AR coatings and surface roughness can backscatter light into the cavity, leading to instabilities arising from hybridization of modes. This was analyzed in reference [121] where the Purcell backscatter suppression was observed in a twisted resonator with lenses from a combination of factors of image rotation, polarization and spatial mode matching. The suppression was to almost $10^6\times$ compared to the free space AR coating specification on the lens, but such suppression is not always available.

7.1.3.1 External Contamination

Accumulation of dust and other particulates due to environmental exposure can introduce significant optical losses and degrade cavity performance. One approach to mitigating this issue is the use of monolithic covered cavities, which minimize exposed surfaces and reduce contamination risks.

For removable optics, cleaning solutions such as First Contact can effectively remove surface contaminants. However, immediate ionization of the surface upon peeling off the protective layer can lead to rapid dust accumulation. Working within a laminar flow bench equipped with a (de)ionizing bar can help mitigate this effect to some extent by reducing electrostatic attraction of airborne particles.

7.2 Rethinking curved cavity mirrors: intracavity lenses

The curvature of cavity mirrors creates a trapping confinement for the cavity mode. A stable cavity configuration imposes constraints on both the curvature of the end mirrors and the overall cavity length [28]. Intracavity lenses can provide the same trapping as curved cavity mirrors. Mathematically, this equivalence can be demonstrated by

$$M_{\text{mirror}}(R = f) = M_{\text{lens}}(f) M_{\text{plane-mirror}} M_{\text{lens}(f)}, \tag{7.3}$$

where M_i represents the ABCD matrix of the corresponding optical element (Appendix A.1). In addition, the spacing between the lens and the plane mirror can be varied, giving more freedom in configuration.

The use of lenses in cavities has been discussed as early as 1965 [122, 123] and in the recent years [124] to improve laser stability and robustness to alignment, primarily using imaging properties of lenses via conjugate-concentric and cat-eye geometries.

Taking advantage of modern day polishing and coating advancements, we demonstrated deployment of lenses within high-finesse cavities for integration with cavity QED experiments. The first experiments with intracavity plano-convex lenses in high-finesse cavities[2] provided a limiting finesse of 11000 for one plano-convex lens (4 intracavity surfaces per round trip) and 17000 for two plano-convex lenses (8 intracavity surfaces per round trip). The lenses were AR coated for 780 nm with R $<$ 0.2% (Layertec, R $=$ 100 mm). They were placed inside a cavity formed of near-planar mirrors (Laseroptik, R $=$ 5000 mm plano-concave mirrors, limiting finesse: 7000). Note that 0.2% reflection per surface should limit

---

[2] Finesse in the range of a few thousand

the cavity finesse to about 800, but the higher finesse is likely due to the Purcell suppression of the backscattered light. Finesse measurement with a Thorlabs lens (LB4854-B, f=20 mm, R $<$ 0.25%) was measured to be $\sim$ 600. The difference is likely a combination of the AR coating and the surface roughness of the lens, as the substrate was fused silica in both cases.

7.2.1 Astigmatism correction in non-0 angle of incidence cavities

A twisted, non-planar cavity geometry supports Laguerre-Gaussian modes with well defined orbital angular momenta (OAM), that are well-suited to study topological effects in light-matter interactions such as in [125, 126]. The cavities mentioned in these references could not operate at complete degeneracy because of quadratic astigmatism introduced by the non-zero angle of incidence on the curved mirrors, which would couple every second OAM mode.

When a ray hits a curved mirror at a non-zero angle of incidence, it experiences different radii of curvature along the two principal axes, given by

$$R_{\text{eff}} = R\cos\theta, R_{\text{eff}} = \frac{R}{\cos\theta} \tag{7.4}$$

in the plane of reflection (tangential) and orthogonal to the plane of reflection (sagittal), respectively [28]. In cavities where the cavity axis meets the curved mirror at an angle, this leads to symmetry-breaking for the modes in the sagittal and transverse planes as they accumulate different Gouy phases and have different resonance frequencies. To suppress the quadratic astigmatism, previous experiments operated at s = 3 degeneracy [126], such that every third eigenmode was degenerate, but the cavity still remained sensitive to cubic astigmatism which couples every third OAM mode.

When curved mirrors are replaced by lenses and plane mirrors, the cavity axis meets the curved surfaces at a normal angle of incidence, preserving the symmetry and eliminating the need for custom elliptical or off-axis parabolic mirrors. Figure 7.2 illustrates the cavity setup built with lenses in the lab by Jaffe et al [96], showing the cavity schematic and the resulting mode degeneracy breakdown. In the absence of cubic and quadratic astigmatism, the remaining degeneracy is limited to quartic terms arising from spherical aberration and non-paraxial propagation, as depicted in the figure.

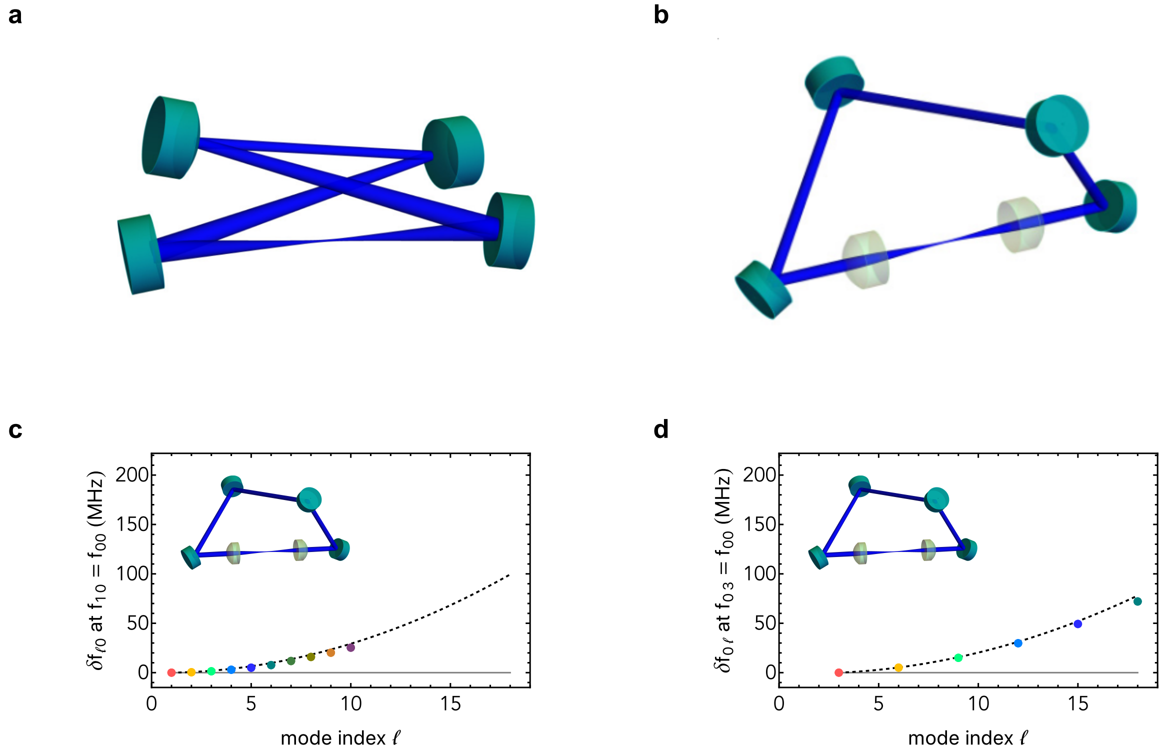

Figure 7.2: Suppression of quadratic and cubic astigmatism in twisted lens cavities. Figures from [96]. (a)-(b) Curved mirrors in a twisted resonator can be replaced by plane mirrors and lenses, eliminating astigmatism arising from off-axis incidence on the curved mirrors. Figures (c)-(d) show mode frequencies of consecutive LG modes supported by the twisted resonator relative to the $l = 0$ (zero OAM) mode. If the resonator were perfectly degenerate, the points would have all been at zero, but they miss degeneracy due to aberrations. The aberration contribution to the spectrum is proportional to l^2, as expected for a quartic perturbation in the absence of quadratic and cubic astigmatism.

7.2.2 Degenerate cavities

A degenerate cavity is defined as one in which a ray of light exactly retraces its path after one round trip inside the cavity. Spectroscopically, at degeneracy, all higher-order spatial modes of the cavity have the same resonance frequency as the lowest-order mode. In such cavities, any spatial input is resonant with the cavity, it does not have to be mode-matched to the distinct spatial modes of the cavity. While the concentric configuration (L = 2R) of a two-curved-mirror cavity should in principle support a degenerate cavity, it is very sensitive to alignments and supports only very small waists with large beam sizes at the end mirrors.

Figure 7.3 shows the round-trip Gouy phases and waists of a cavity mode in the case of a two-curved-mirror cavity and a two-lens cavity. Complete degeneracy is achieved when the round-trip Gouy phase is 0 or an integral multiple of 2π. It can be seen that for the lens cavity, at the 4-f configuration with the lenses, the Gouy phase reaches zero with a non-diminishing waist size and a wide stability region. Such a nearly-degenerate 4-f cavity with two plano-convex lenses was built in the lab to perform cavity Floquet Hamiltonian experiments and is discussed further in chapter 8.

It will be interesting to explore other self-imaging lens systems inside a cavity, such as the conjugate-concentric configuration [123, 127]. With intracavity GRIN lenses, the Maxwell fish-eye or Luneberg lens configurations can be achieved for completely degenerate cavities, although the absorption loss from GRIN material will be a limiting factor.

7.2.3 High-NA cavity QED

As discussed in chapter 2, the cooperativity of a cavity can be enhanced by building a smaller waist cavity. Figure 7.3e shows a typical waist diagram for a two-mirror cavity. One can obtain a small waist by either going to the near-planar regime ($L \to 0$) [40] or near-concentric regime ($L \to 2R$) [24, 128] as shown in figure 7.3e. The former provides very limited optical access and the latter is extremely sensitive to alignment. A route to

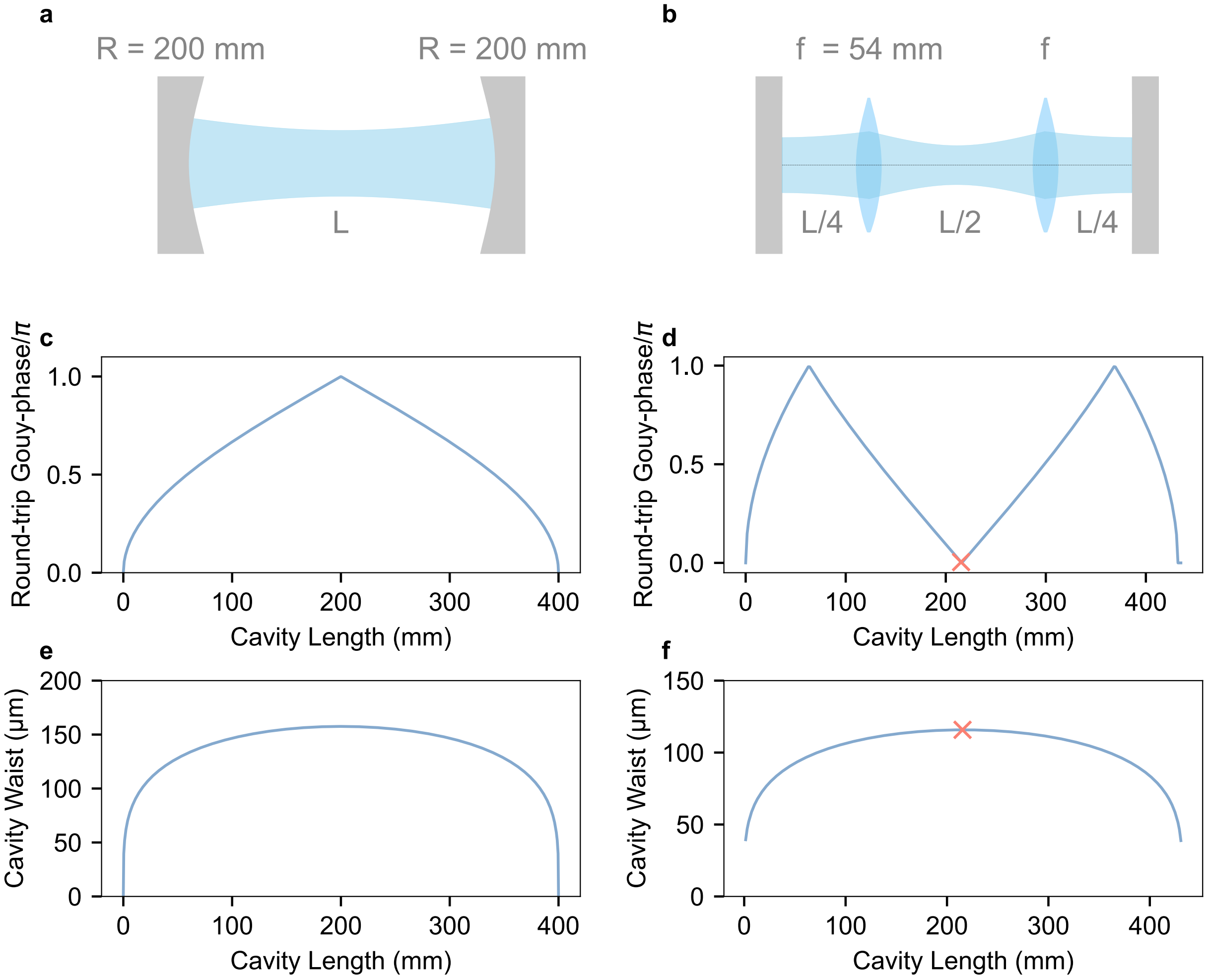

Figure 7.3: Degeneracy in a two-lens cavity with non-diminishing mode waist (a) A cavity of length L with two curved mirrors with radii of curvature R. (b) A cavity with two lenses and plane mirrors. (c), (e) Accumulated round-trip Gouy phase and cavity mode waist as a function of cavity length for the cavity shown in (a). Degeneracy is achieved when the Gouy phase is 0 at the edge of stability, when the waists also reach 0. Such degenerate cavities are hard to construct because of sensitivity to alignment and very large mode sizes at the end-mirrors. (d), (f) Accumulated round-trip Gouy phase and cavity mode waist as a function of cavity length L for the cavity shown in (b). Degeneracy is achieved at the 4-f configuration, with a non-diminishing waist size at the center of the stability diagram.

yet tinier waists is to explore running-wave cavities such as bow-tie cavities [95] and twisted non-planar geometries [96, 125, 126] that can go down below 10 microns (Fig 7.2a,b).

For simple two-mirror cavities, intracavity lenses can add additional degree of freedom allowing a broader configuration space to get close to smaller waists. We consider the cavity built in the lab by Shadmany et al [32] in figure 7.4a by incorporating an asphere with focal length $f = 1.45$ mm. By changing the length of the longer arm L1 with respect to the shorter arm L2, one can get to sub-micron waists (figure 7.4b) and degeneracy, with a more forgiving stability range of a few microns. The cooperative enhancement from the small waist ($\mathcal{C} = 1.6(2)$) enabled a strong coupling regime with a single atom, evident from the splitting in the cavity spectrum, even at very low finesses (<50) (figure 7.4c).

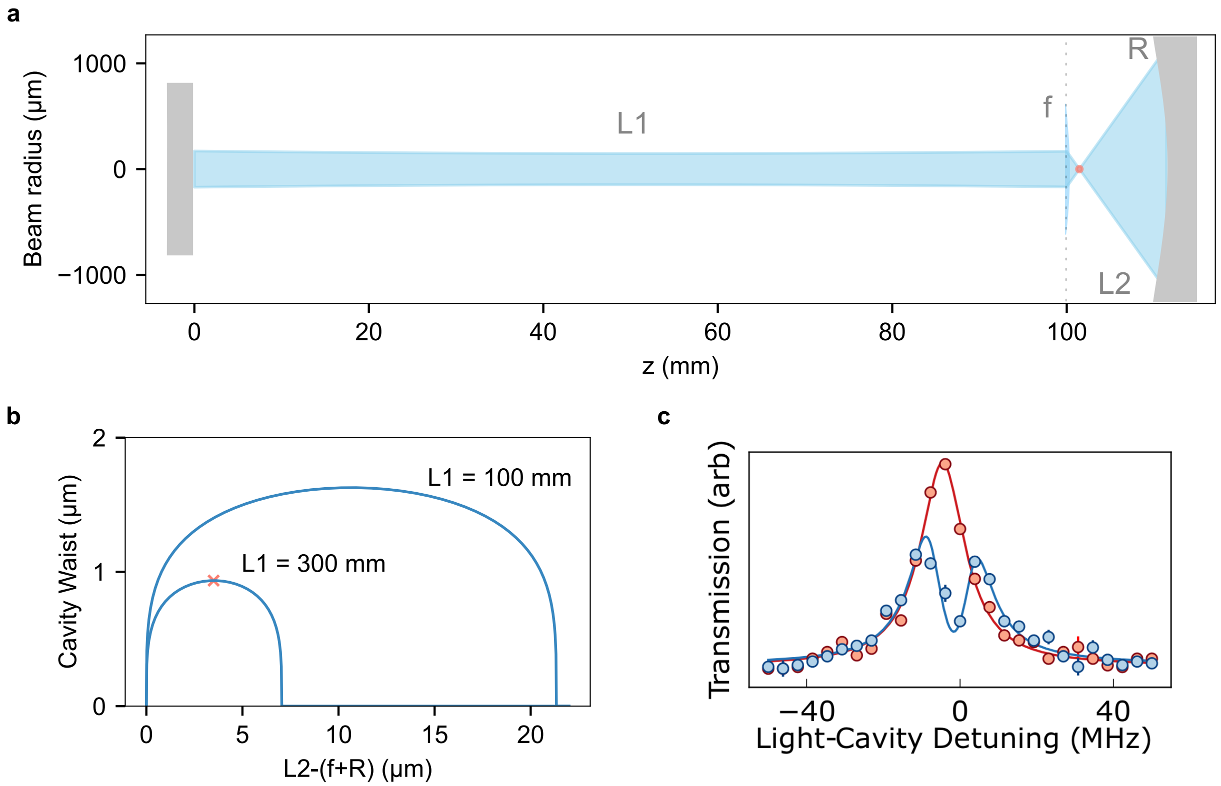

Figure 7.4: Strong single-atom-cavity coupling with a lens cavity. (a) A single-lens cavity with a long arm and a short arm. A curved end-mirror is used to offset the waist from the end-mirror to enable access for atoms. (b) Waist profiles for different lengths of the short arm (L2) and long arm (L1) (c) Bare cavity transmission (red), cavity transmission with one atom loaded (blue) corresponding to a cooperativity $\mathcal{C} = 1.6(2)$ achieved through a sub-micron cavity waist in a very low-finesse (<50) cavity. Figure from [32].

7.3 Scaling to a cavity array: intracavity microlens arrays

We build an approximately 30×30 cavity array by mounting a microlens array (Thorlabs ML300-AR) between two plane mirrors. The setup is shown in figure 7.5. The microlens array is 1 cm x 1 cm in size. Each microlens is a square, parabolic lens and has a pitch of 300 μm. The focal length of the lenses is 18.6 mm. Each of the mirror-microlens-mirror module behaves like a single cavity, thus giving an array of cavities. To excite the array

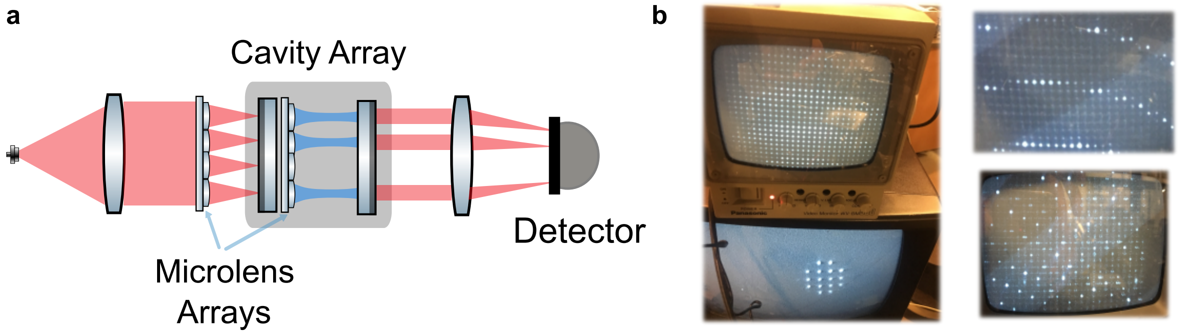

Figure 7.5: A cavity array (a) is made by mounting a microlens array between two mirrors separated by 9.8 mm. The output of the cavity is imaged onto a detector. (b) An approximately 30×30 array is imaged onto a camera. The pictures show different modes of operation when all the cavities are driven by an input with a fast (left) and slow (right, top) frequency sweep, and when the cavity length is changed away from a confocal degeneracy configuration to reveal higher-order spatial modes in individual cavities (right, bottom).

simultaneously, beam telescope was set up using two lenses to collimate and magnify the beam diameter to 1 cm.

The finesse of one of the cavities was measured to be 84.4. Mirrors used in the cavity array had a reflection coefficient $R \sim 0.97$, implying that the limiting finesse of the array is ~ 430. Figure 7.6 shows a 4x4 non-degenerate set of cavities, and the corresponding 16 resonant peaks on the oscilloscope as the laser is quickly swept over a range of frequencies. The frequency spacing between the cavities is around 500 MHz. We also demonstrated proof-of-concept arbitrary cavity control by choosing a non-degenerate set of cavities in the array and sending particular tones onto the array using an EOM. The array is locked via a side-of-fringe lock on a single cavity.

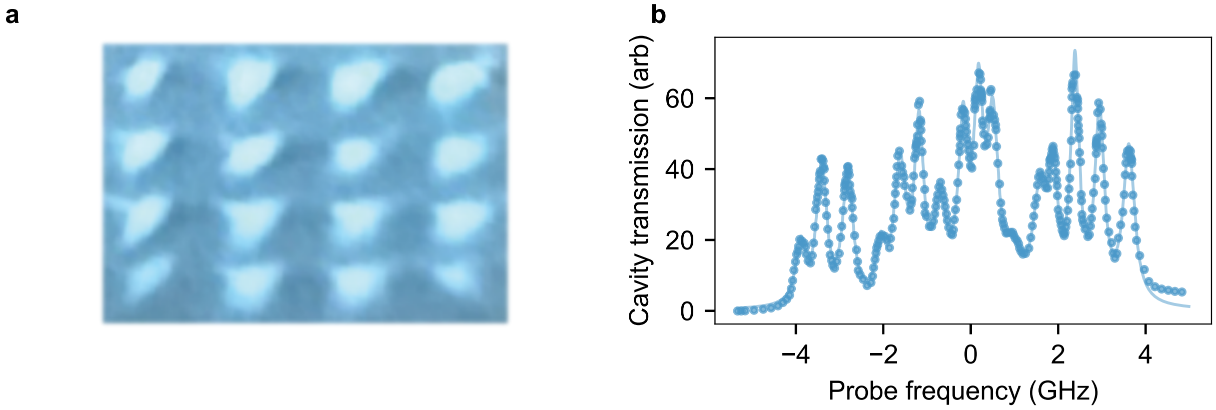

Figure 7.6: Isolated set of 4 × 4 cavities (a) A set of 4 x 4 cavities isolated for the experiment. The laser frequency is swept fast so that they appear to light up simultaneously. (b) The 16 transmission peaks corresponding to the 16 cavities, fitted to a sum of 16 Lorentzian profiles.

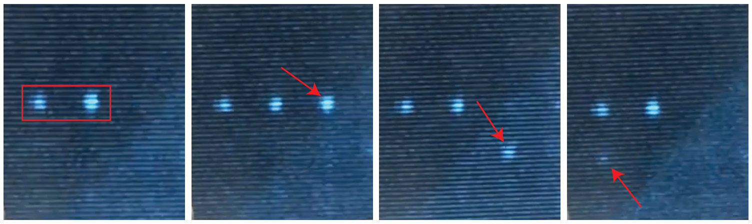

0 GHz 1.0 GHz 1.5 GHz 2.5 GHz

Figure 7.7: Individual cavity control. The laser carrier is locked to the cavities boxed in red. The arrows point at the cavities resonating with the sidebands introduced by the EOM. The frequency shown at the bottom of each image is the EOM modulation frequency for that frame.

7.4 RF and optical modulation of cavities: intracavity $\chi^{(2)}$ crystals

7.4.1 Modulation of the Optical Path Length with an EOM

Electro-optic modulators (EOMs) change the optical path length of light propagating through a crystal by altering the refractive index when a voltage is applied. In essence, the phase accumulated by light traveling through a crystal of length L depends on the optical path length (OPL), given by nL, where n is the refractive index. When a voltage V is applied across the crystal, an electric field E = V/d is generated between the electrodes (with d being the spacing between them), which changes the refractive index via the linear electro-optic (Pockels) effect.

The change in refractive index is

$$\Delta n = -\frac{1}{2} n^3 r_{\text{eff}} \frac{V}{d}, \tag{7.5}$$

where n is the unperturbed refractive index and r_{eff} is the effective electro-optic coefficient. For lithium niobate, the highest r_{eff} is typically around 30 pm/V.

The phase shift $\Delta\phi$ experienced by the light is related to the change in optical path length by

$$\Delta\phi = \frac{2\pi}{\lambda} \Delta(\text{OPL}) = -\frac{\pi}{\lambda} L n^3 r_{\text{eff}} \frac{V}{d}. \tag{7.6}$$

This mechanism underlies high-bandwidth tuning and stabilization of cavities by rapidly adjusting the phase shift experienced by the mode without the need for mechanical movement of the cavity mirrors.

7.4.2 High bandwidth modulation and stabilization of high-finesse cavities

High-finesse optical cavities use piezoelectric transducers (PZTs) to adjust the mirror spacing for tuning and stabilization. The mechanical motion of bulk material under the piezoelectric effect slows down the response time. The operational bandwidth is further reduced (typically up to a few hundreds of kilohertz) due to factors such as mechanical resonances at low frequencies and additional mechanical loads such as big mirrors[3].

Integrating an electro-optic crystal such as lithium niobate inside the cavity replaces mirror displacement with an electrically induced change in refractive index, thereby modifying the optical path length and effectively changing the length of the cavity. Since the electrooptic response is much faster compared to piezoelectric response, this approach can enable modulation over a much broader frequency range from DC up to few GHz, facilitating rapid tuning and modulation.

For the experiments, we utilized a 3 mm long crystal (figure 7.8a) with transverse dimensions of $2{\times}2\text{mm}^2$, and achieved a limiting finesse of 9900 (Figure 7.1a). Figure 7.8b shows cavity spectra when the intracavity crystal is modulated at 20 MHz. The sidebands appear because the cavity optical path *length* is being modulated at 20 MHz. At modulation frequencies $\omega_m \ll$ cavity FSR, the sideband transmission amplitude can be approximately described by Bessel functions as in the case of laser modulation. Figure 7.8c shows high-bandwidth stabilization of the cavity in action when the measured photodiode signal of the cavity transmission is fed back to the intracavity crystal (after being amplified using a gain = 2) while the drive laser is swept across resonance.

Figure 7.8d shows the network analyzer (NA) measurement of the cavity transmission as a function of frequency of the output of the NA, which is sent as a perturbation to the cavity through the crystal. The crystal also receives the output photodiode cavity signal and feeds back to the cavity accordingly. The measurement is done when the laser is loosely locked to the cavity for stabilizing slow drifts . A fall-off at around 1 MHz is observed. The 50Ω RC bandwidth of the EOM drive circuit is calculated to be 4 GHz, which suggests that our stabilization was limited by the cavity linewidth ($\sim$811 kHz), and the bandwidth of the intracavity EOM lock was larger than the cavity linewidth.

---

[3] There have been demonstrations of high bandwidth piezoelectric actuator performance: for instance, see Reference [129].

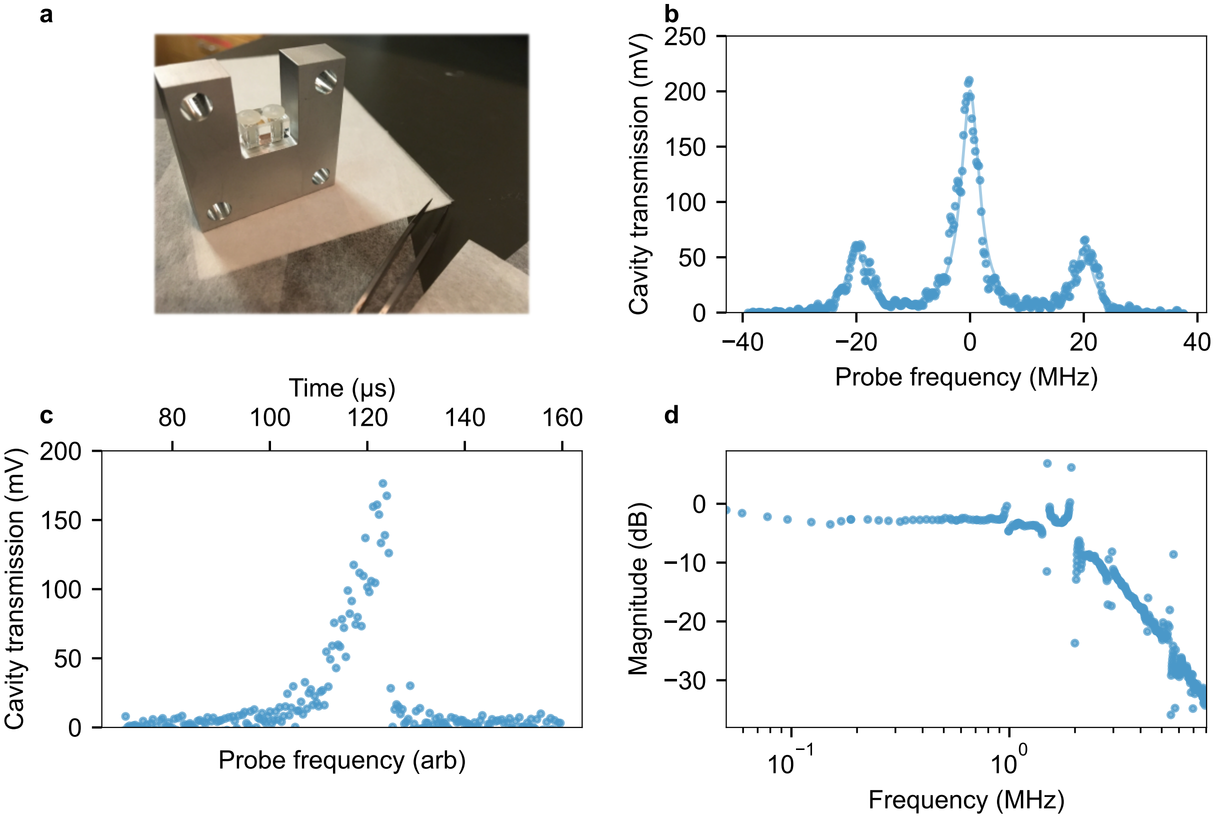

Figure 7.8: High-bandwidth intracavity modulation and stabilization. (a) Mount for the intracavity lithium niobate crystal. The 2 mm × 2 mm × 3 mm crystal is clamped to the surface of the aluminum mount with the acrylic piece. The aluminum mount acts as the ground. The top gold-plate surface of the crystal is placed in surface contact with a copper strip for the other voltage terminal. (b) Modulation of the cavity length by the intracavity EOM at 20 MHz. (c) Demonstration of feedback to the cavity length via the crystal. The rising edge corresponds to positive feedback, hence it is lengthened, the falling edge corresponds to negative feedback (desired). (d) Measurement of the cavity response when the laser is lightly locked to the cavity and the crystal actively feeds back to the cavity. The fall-off happens at about 1.1 MHz, around the linewidth of the cavity. The 50Ω RC-limited bandwidth of the crystal is 4 GHz, suggesting a lock bandwidth higher than 1 MHz for the intracavity EOM lock.

7.4.3 Home-built high-frequency EOM

The cavity modulation is Purcell-suppressed as the frequency of the modulation is increased, requiring higher power at higher frequency drives. However, if the frequency corresponds to the transverse mode spacing, or the FSR of the cavity, the Purcell enhancement is expected to boost the modulation even at lower powers. This requires building an EOM that can be driven at higher frequencies, corresponding to typical free spectral ranges of macroscopic optical cavities – it is difficult to do so with a conductive contact with the crystal because all of the power will be reflected at high frequencies without intentional impedance matching, so we built a resonant EOM. Following Reference [130], we build an in-house resonant EOM

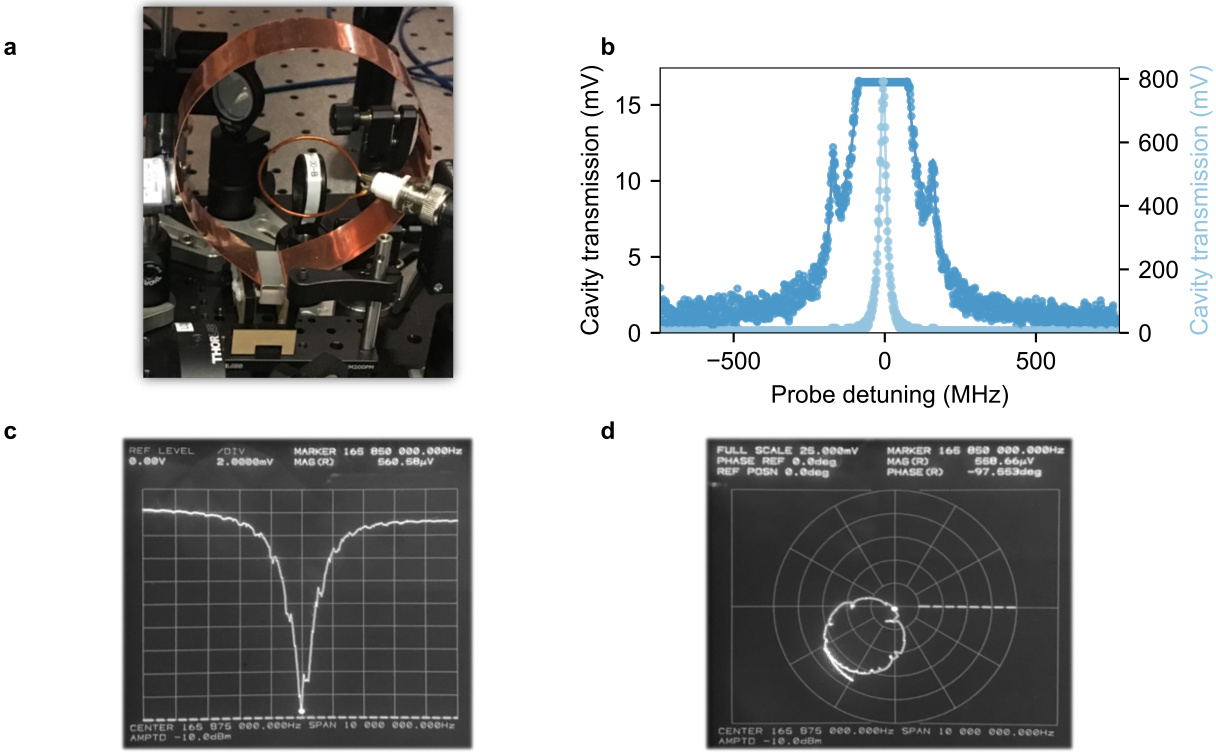

Figure 7.9: Resonant EOM at 166 MHz. (a) The crystal is shown with the copper sheet-coil and the driving coil inductively coupled to the copper-sheet + crystal LC circuit. (b) 1.5% laser sidebands at 166 MHz measured via cavity spectroscopy. Note that this EOM is outside the cavity. (c), (d) Impedance-matching of the driving coil to the EOM circuit characterized by measuring the reflection into the driving coil as a function of drive frequency on a network analyzer.

at 166 MHz (Figure 7.9). To construct the EOM, a copper sheet was sheared into a 12 in x 1 in piece, and formed into a single coil-like shape with a diameter of 3.7 in (Figure 7.9a). The edges of the coil were bent at around 1 cm to create flaps to hold the 26 mm x 9 mm x 9 mm lithium niobate crystal with the help of an acrylic mount made by laser cutting. Acrylic works as an insulator, preventing any electrical loss to the mount by isolating the EOM. The coupling coil was a single loop of copper wire, plugged into a Mini circuits ZHL-1-2W-S+ amplifier, that was in fed by a Programmed Test Source at the resonant frequency. The maximum power input to the EOM was 36 dBm (around 4 W).

The system is designed to be critically coupled as can be seen by the zero reflection at the driving coil at the resonance frequency in the trace shown in figure 7.9c: all the power going into the inductive coil is transferred completely to the EOM with no reflections. This condition was reached at by moving the inductive coil relative to the EOM coil to achieve perfect impedance matching. The quality factor Q (= resonant frequency/FWHM) of the resonator was measured to be 167.

Calculations estimate a power of around 8% in the first order sideband with an input power of 36 dBm. Figure 7.9b shows the first order sidebands obtained at a resonant frequency of 165.85 MHz at the same input power. The sideband intensity is almost $\sim 1.5\%$ of the total intensity. Some reasons for this deviation could be imperfect coupling, piezoelectric resonances and losses to surroundings. Observation of noise at 165.85 MHz on other lab electronics support the latter. Some possible improvements include using more input power, a smaller crystal or making a higher Q resonator. We could not put this crystal inside a cavity because it was not AR coated.

7.5 Discussion

Aberration engineering with intracavity optics

Cavities in the recent years have tried to become high-finesse, near-degenerate and small-waisted in an effort to increase the cooperativity. The paraxial ABCD description is not complete in these extremes and non-paraxial corrections and aberrations from optics need to be taken into account. Using the theory developed in [96] and utilizing techniques to shape the profile of intracavity optics such as phase plates can help correct for these factors as required.

Cavity atom array

Integrating a cavity array with aspheres will provide an array of cavities with high single-atom cooperativities and is a direction now being pursued in the lab. The atom-cavity array can be used to implement site-specific fast gates and high-rate readout.

Fast tunability of finesse for on-demand cavity readout

Beyond high bandwidth stabilization, intracavity EOMs in high-finesse cavities can be utilized for fast control of cavity finesses. Reference [90] demonstrates tunable finesse by using a second cavity as a mirror whose transmission can be changed by changing the length of the cavity. Incorporating an EOM in the second cavity will enable fast tuning of the length of the second cavity, and hence fast control of the finesse of the first cavity. Similar to the optical coupling, this could be useful for fast switching of on-demand readout of atoms from cavities.

Spatial phase profiling in a cavity array

Figure 7.10 depicts one possible implementation of spatial phase profiling using an electrooptic crystal to obtain a range of almost $\lambda/4$ phase shift at 780 nm across the crystal with an applied voltage range of -300 to 300 V. Such a capability can be useful for individually stabilizing cavities in a cavity array, correcting the cavity frequencies for inhomogeneous Stark shifts across the array, or fast individual site addressing of cavities.

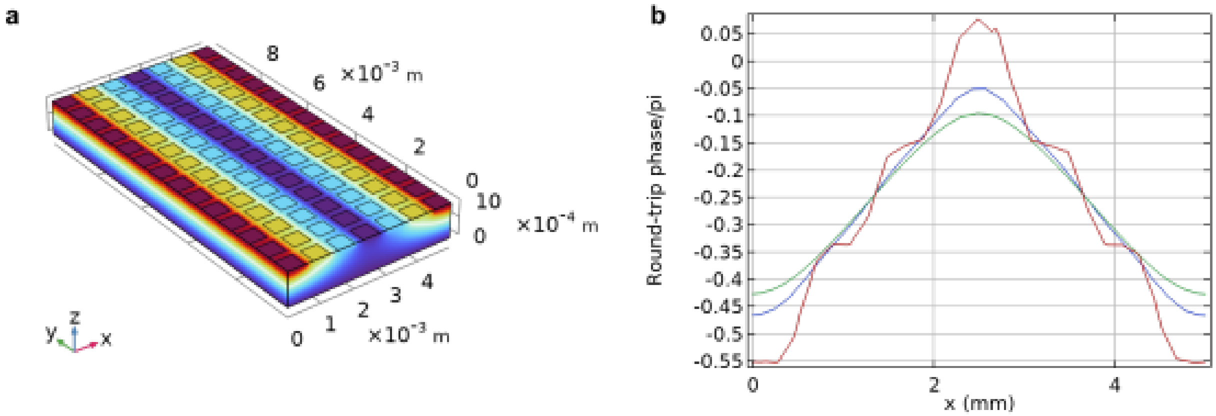

Figure 7.10: Spatial phase profiling with an intracavity EOM. Instead of having one uniform conducting plate for providing voltage to the crystal, one could use multiple conducting pads with individual potentials (for example, by designing a PCB). (a) and (b) show a simulation with such a design when there is a gradient of voltage along the columns of pads. The different curves correspond to the profiles for round-trip phase shift along line cuts at y = 0.6 × length and z = 0.25 (green), 0.5 (blue), 0.75 (red) × height. The simulation is done on COMSOL Multiphysics. (Thanks to Oguz Tolga Celik for helping me get started with the software.)

Chapter 8

Floquet Hamiltonians for light in lens cavities

Building on one application of degenerate cavities with intracavity lenses, this chapter will discuss engineering Floquet Hamiltonian dynamics in cavities. After a brief introduction of the cavity Floquet formalism, section 8.1 will discuss the dynamics of a synthetic, massive light wavepacket in 1D harmonic and 2D harmonic potentials in cavities, including dynamics with a barrier in a 2D harmonic well. Section 8.2 will discuss preliminary results demonstrating non-local Hamiltonian dynamics and Section 8.3 will discuss design considerations for simulating a non-local Hamiltonian for fast transport of the light particle across a cavity plane. Towards the end, the chapter will briefly mention potential improvements to the platform design and applications in studying particle dynamics in non-trivial geometries.

Introduction

A ray trapped inside the cavity is transformed in exactly the same manner every cavity round trip time $2L_{\text{cav}}/c$. Much like in a solid-state crystal, where an electron experiences a periodic potential and Bloch theory can be used to simplify the analysis, a Floquet Hamiltonian

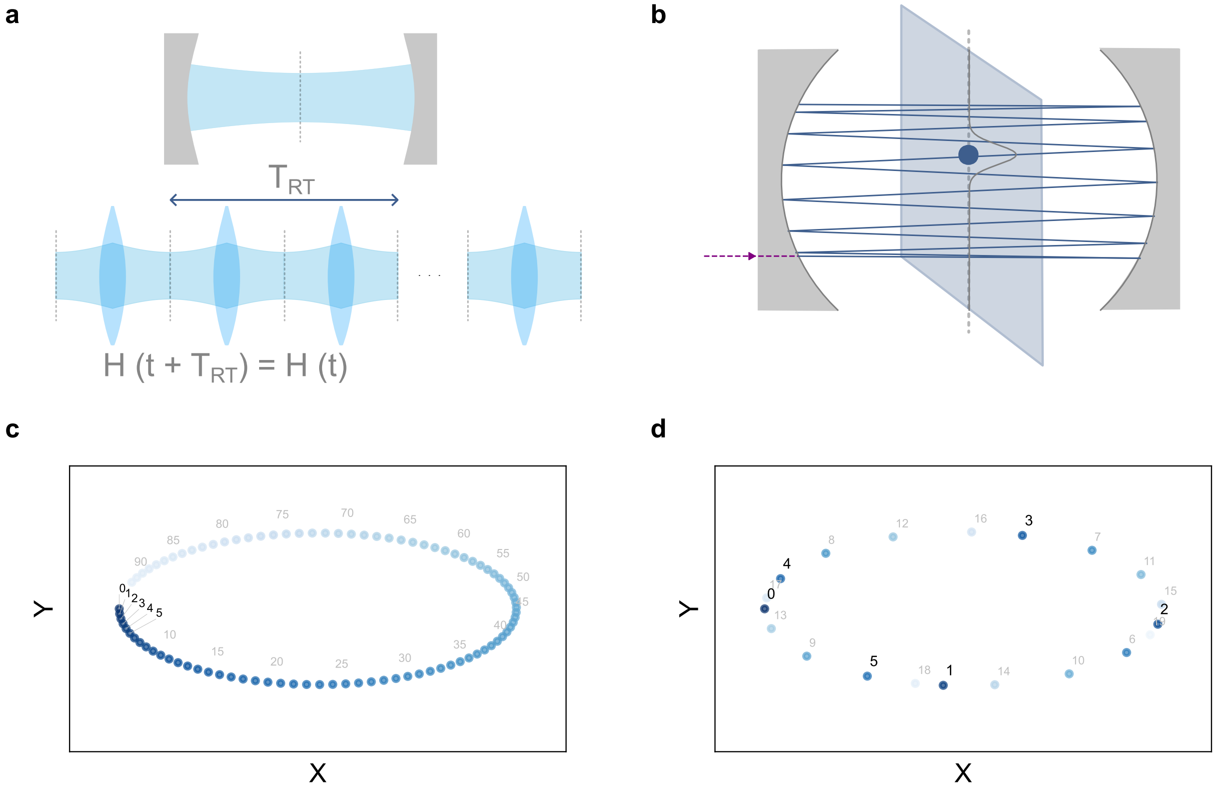

Figure 8.1: Cavity Floquet Hamiltonian engineering. (a) If we unfold a cavity into a series of periodically repeating optical elements, it is simpler to see how a ray (or mode) inside a cavity experiences a periodic evolution in time. This periodicity enables a Floquet Hamiltonian formalism for cavity modes in a plane. (b) The curvature of the mirrors or lenses in the cavity provide a restraining potential for light. If the position of the ray is observed every round trip along a line in a 1D near-degenerate cavity, it follows an evolution equivalent to that of a massive particle in a harmonic potential. (c), (d) The position of a ray every round-trip in one plane of a 2D cavity is traced for a nearly-degenerate cavity (c) and non-degenerate cavity (d). A later round trip has a lighter shade of blue. As we get closer to degeneracy, the stroboscopic evolution approaches a continuous evolution. We operate in the near-degenerate configuration to simulate the Hamiltonians using synthetic massive light particles in the following sections.

formalism can be devised for cavities, with system periodicity in time instead of space. The analogy doesn't go too far: the former results in quasimomenta and the latter in quasienergies as c-numbers.

The full derivation of the formalism is described in Ref [131]. A transverse intracavity plane is selected with the corresponding round-trip ABCD matrix, and a continuous Hamiltonian is found such that it replicates the stroboscopic evolution of the ray in the plane. In the limit that the transverse plane dynamics are much slower than the longitudinal dynamics, the stroboscopic evolution approaches the continuous evolution limit. This limit requires the cavity condition that transverse mode-spacing (TMS) $\ll$ free-spectral range.

For the simplest case of a two-mirror resonator at near-degeneracy, the equivalent Hamiltonian is that of a 2D harmonic oscillator (Fig 8.1), with the trap frequency ω_{trap} corresponding to $2\pi\times$TMS. The picture checks with the Hermite-Gaussian eigenmodes of the cavity, which are also the eigenmodes for a quantum harmonic oscillator. It is worth emphasizing that the cavity dynamics are entirely classical, it just so happens that both systems follow identical differential equations that yield identical eigenmodes and dynamics thereafter.

8.1 Local harmonic potentials

8.1.1 1D harmonic oscillator: three mirror cavity

In a three-mirror cavity tuned to confocal degeneracy [28], the electric field gets flipped after each round trip in the plane of reflection due to an odd number of mirrors (figure 8.2a and b). This is equivalent to observing that the eigenmodes along the cavity plane acquire an additional π phase, which results in a complete degeneracy condition for that axis versus a confocal half-degeneracy condition for the orthogonal axis. The additional degree of freedom offered by the addition of a third mirror for controlling different arm lengths also allows one to minimize the region of unstable confocality, that arises in a two-mirror cavity with slight differences in the radii of curvature, thus allowing one to obtain a more nearly-degenerate cavity along one of the axes.

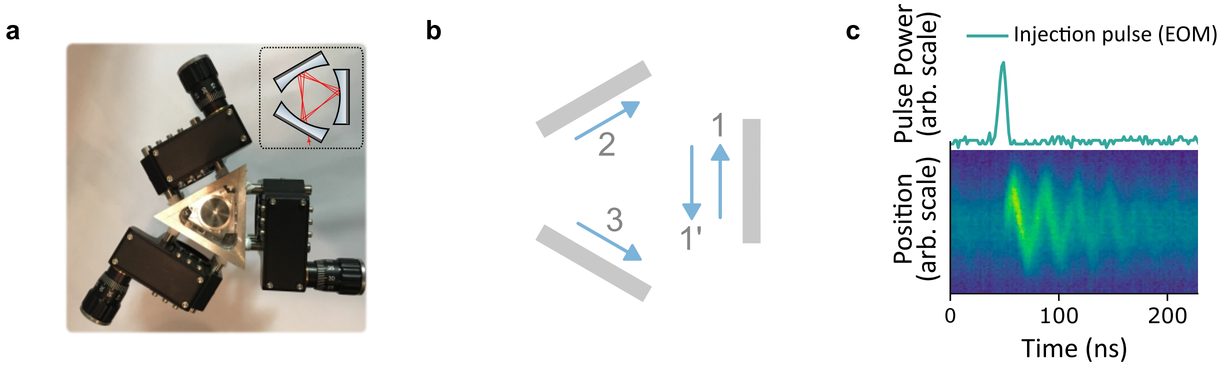

Figure 8.2: 1D harmonic oscillation of a synthetic light particle in a three-mirror cavity. (a) The three-mirror running wave cavity is made of three concave mirrors at 120 degrees to each other and is stably nearly-degenerate along the cavity plane axis. One running-wave mode is used for measuring dynamics and the backward mode is used for stabilizing the cavity to the laser. (b) Due to image rotation, cavity eigenmodes in the plane of the cavity acquire an additional π phase which shifts the confocal point to the fully degenerate point for those eigenmodes. The control on the individual length segments via mirror translation stages help to move away from the unstable point for a confocal cavity. (c) Injected pulse's temporal profile (RF input to the EOM on the optical input) and the measured sinusoidal oscillator dynamics. Spatially, the particle is injected by displacing a spatially Gaussian input from the cavity axis (equivalent to initially exciting a pendulum by releasing it from a point away from its resting position). The displaced Gaussian is a superposition of higher-order HG eigenmodes of the cavity, with weights equal to those of a coherent state. Temporally, the injection of the particle is done by generating a short pulse with an RF-switch and an EOM such that it is resonant with all the spatial modes around the mean mode index of the coherent state. The output is imaged on an avalanche photodiode with 400 MHz bandwidth and a small aperture, such that its imagining resolution is finer than the amplitude of oscillation. At each location, a time trace is taken and later the data is reshaped to obtain the spatio-temporal dynamics shown in the figure. The dynamics correspond to a transverse mode spacing of about 30 MHz, at a free-spectral range of about 2.5 GHz.

Such a cavity is shown in Fig 8.2a. The parameters of the cavity were determined using a ray-tracing code ensuring that the rays in the mode return to their original position and slope after one round-trip in the cavity. The cavity spacer was machined in the GCIS machine shop. To excite the cavity with a coherent state, an off-axis Gaussian is injected into the cavity. Spectroscopically, the input should be wide-enough to cover the frequencies of the required spatial modes[1] in the near-degenerate manifold.

Fig 8.2c shows the injected pulse profile and the sinusoidal oscillator dynamics measured by a photodiode mounted on a 2-axes translation stage.

8.1.2 2D harmonic oscillator: lens cavities

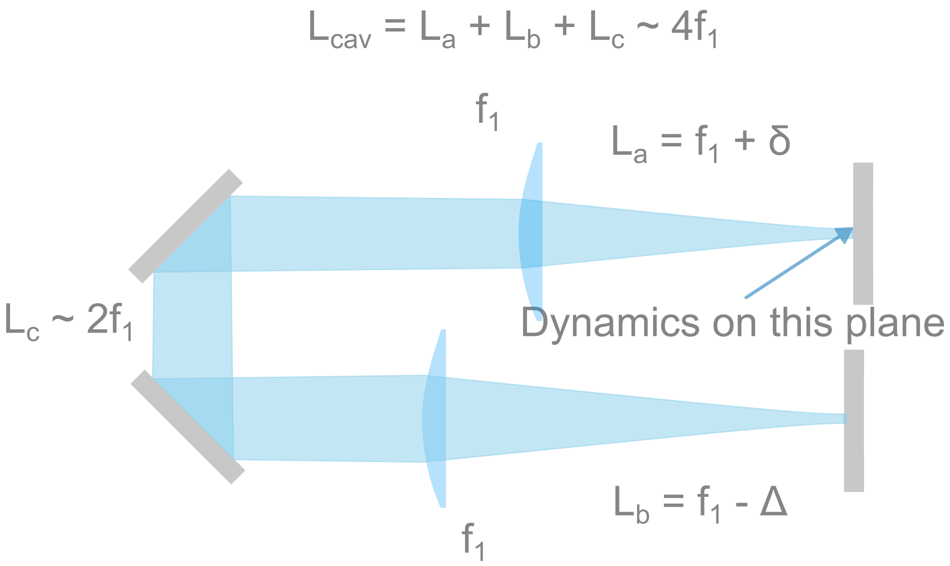

Figure 8.3: Cavity for the 2D harmonic potential using two lenses and plane mirrors. As discussed in the previous chapter, this configuration enables a nearly-degenerate cavity without going to the edges of the stability diagram with very tiny waists. The cavity is folded to enable adequate optical access for input, locking and coupling to other cavities in the latter sections. $f_1 = 54$ mm, $\delta \sim \Delta \sim 6$ mm. The transverse mode spacing can be tuned by changing δ. We operated around 4 MHz for the transverse mode spacing. The dynamics are shown in figure 8.4.

To explore Floquet engineering further, we design a near-degenerate cavity, now in 2D, using two lenses in a 4f configuration. This configuration allows us to approach degeneracy at a finite waist as shown in the previous chapter. Another added advantage is that the

---

[1] Ideally, the spectral width should include all the spatial modes supported by the cavity. Experimentally, the number of modes can be determined by the maximum initial displacement of the input beam, and lower number of modes allows us to have longer pulse durations.

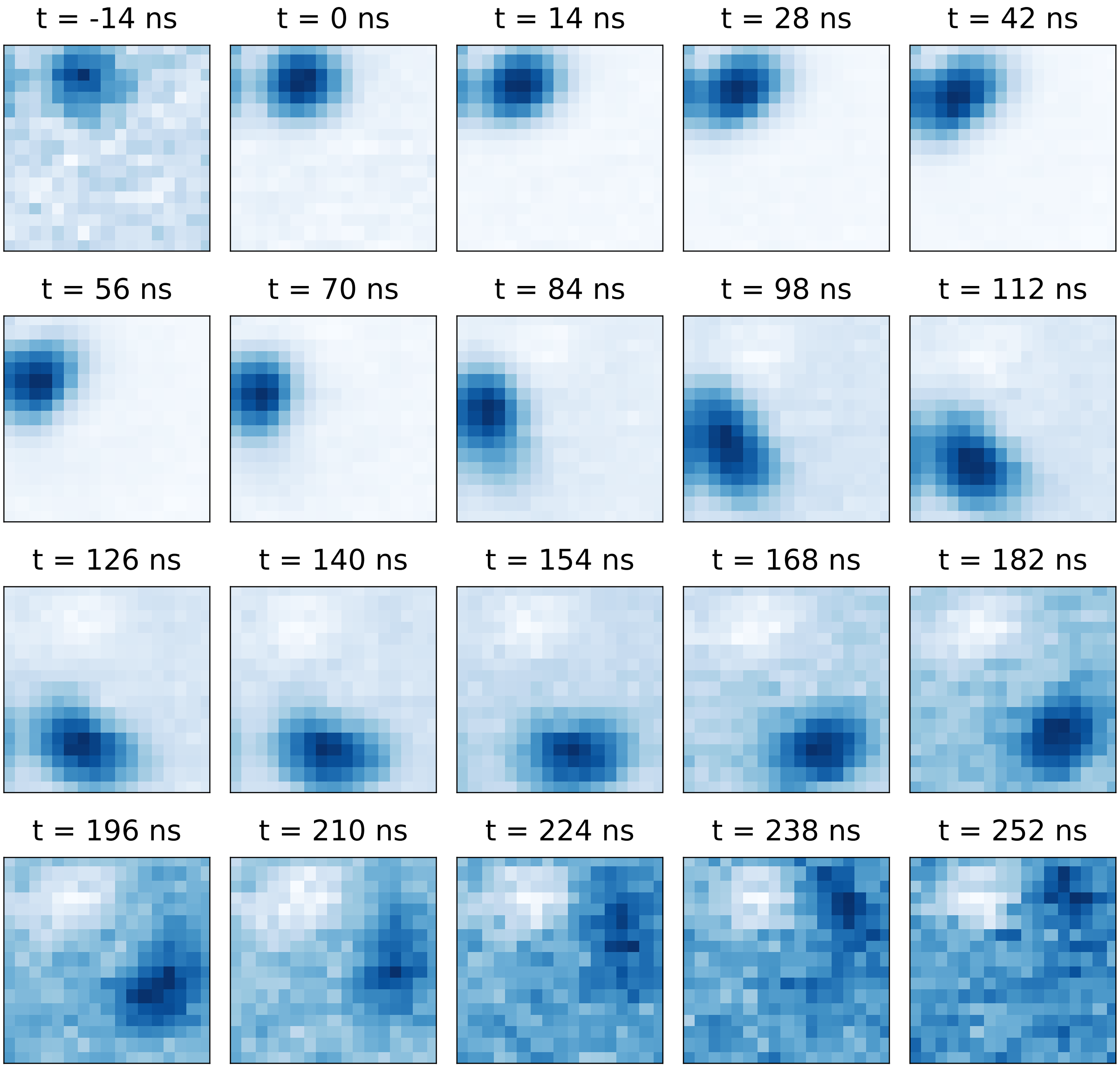

Figure 8.4: 2D harmonic oscillation of a synthetic light particle in a two-lens cavity. A two-lens cavity in a 4f-configuration provides a nearly-degenerate cavity along both axes, proving a 2D (Floquet) harmonic potential. The particle is injected in a similar manner as the three-mirror cavity (figure 8.2) and the measurement photodiode is translated along both the x and y axis. The particle follows an anticlockwise trajectory. Each frame has been renormalized in intensity for visibility. In actuality, the intensity decays as light is lost from the cavity. The white spot in the later frames is an artefact of background subtraction, but gives a reference for the initial injected pulse. For the measurement, we lock the cavity to the HG_{00} mode as it is spatially separated from the dynamics region and the output is subtracted from the data frames shown here.

waist of the cavity lies on the end plane mirrors, which we also choose as the imaging plane[2]. This is also helpful in later stages when we couple to another cavity.

Using the same method as before, we confirm the 2D harmonic oscillator behavior of an injected wavepacket in the cavity as shown in Fig 8.4. Because of the low-finesse of the cavity[3] and limited available laser power, we are only able to capture a part of the cycle before the intracavity light is completely lost.

8.1.3 Reflection off a barrier in a harmonic potential

Next, we use an end mirror with a rectangular deformation (figure 8.11a) to emulate a barrier in the harmonic oscillator potential. The deformation is achieved by having an extra deposition of the substrate on the mirror in a localized region, such that it imparts a local phase-shift of about 0.42π to the modes in the region. The details of the process are discussed in the figure description. The dynamics can be numerically simulated using the more general method discussed in section 8.3.1.1. The Hamiltonian according to which the wavepacket evolves is:

$$H = \frac{\vec{p}^2}{2m} + \frac{1}{2}m^2\omega^2\vec{x}^2 + U(\vec{x}) \tag{8.1}$$

where $U(x)$ is a step-function potential. In figure 8.5, we can see the expected effect on the synthetic particle as it gets reflected once it encounters the barrier.

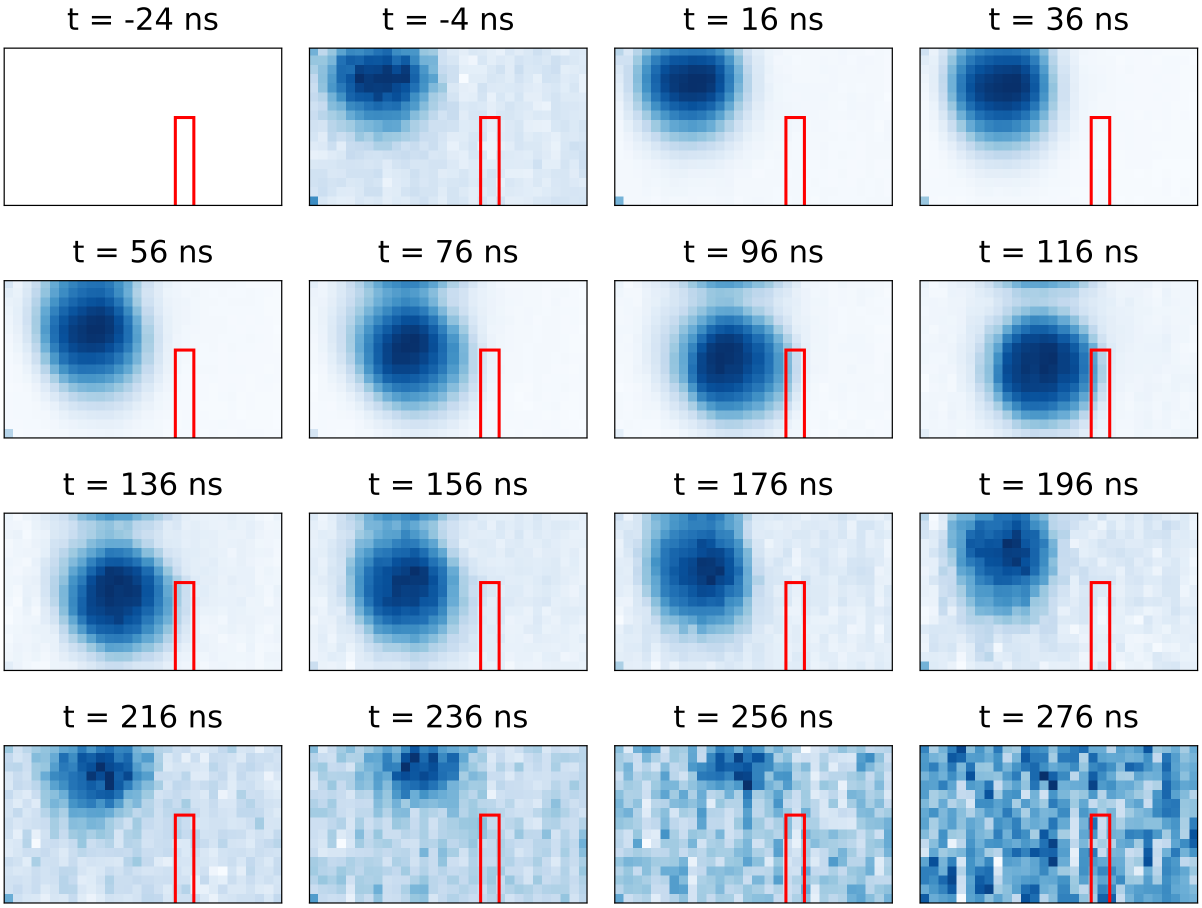

Figure 8.5: Dynamics in a 2D harmonic potential well with a barrier. The red rectangle marks the approximate position of a “barrier” in the 2D harmonic potential well, implemented by using an end-mirror which has an extra deposition such that it imparts a phase shift of about 0.42π to the cavity modes in that region (figure 8.11a). The injected particle is seen to follow an anticlockwise trajectory until it hits the barrier and is reflected, much like a massive particle in a potential well with a barrier.

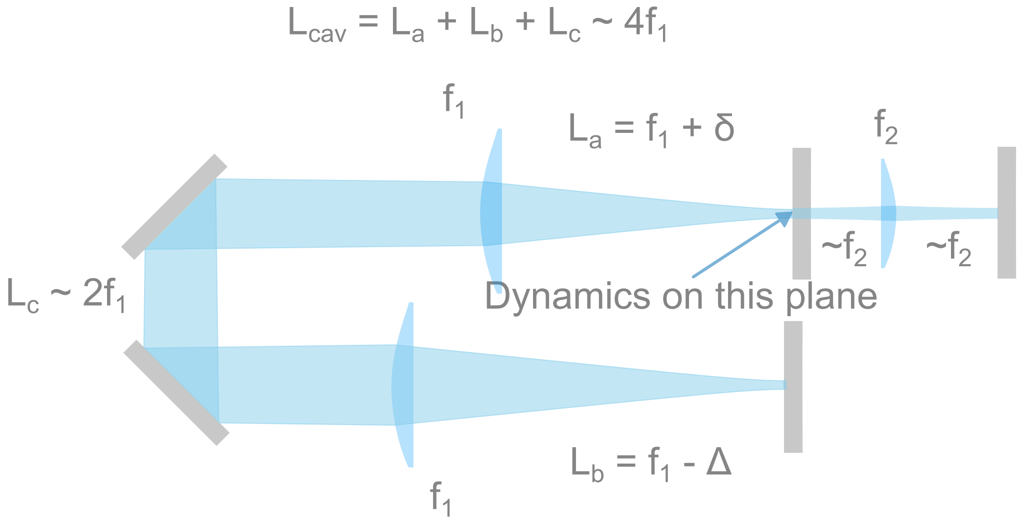

Figure 8.6: Cavities for the non-local coupling in a 2D harmonic well. The primary (nearly-degenerate) 'science' cavity is off-resonantly coupled to a degenerate confocal cavity to break the odd-even symmetry of the science cavity. The coupling strength between spatial modes a and b of the two cavities respectively is $g/2\pi = \sqrt{T\ FSR_{\text{science}}\ FSR_{\text{confocal}}}\Phi(a,b)/2\pi$, where $\Phi(a,b)$ is the spatial overlap between the two modes and T is the transmission coefficient of the shared end-mirror. The cavity parameters are $\{f_1, f_2\} = \{54, 22\}$ mm, $\delta \sim \Delta \sim 6$ mm. The dynamics are shown in figure 8.7.

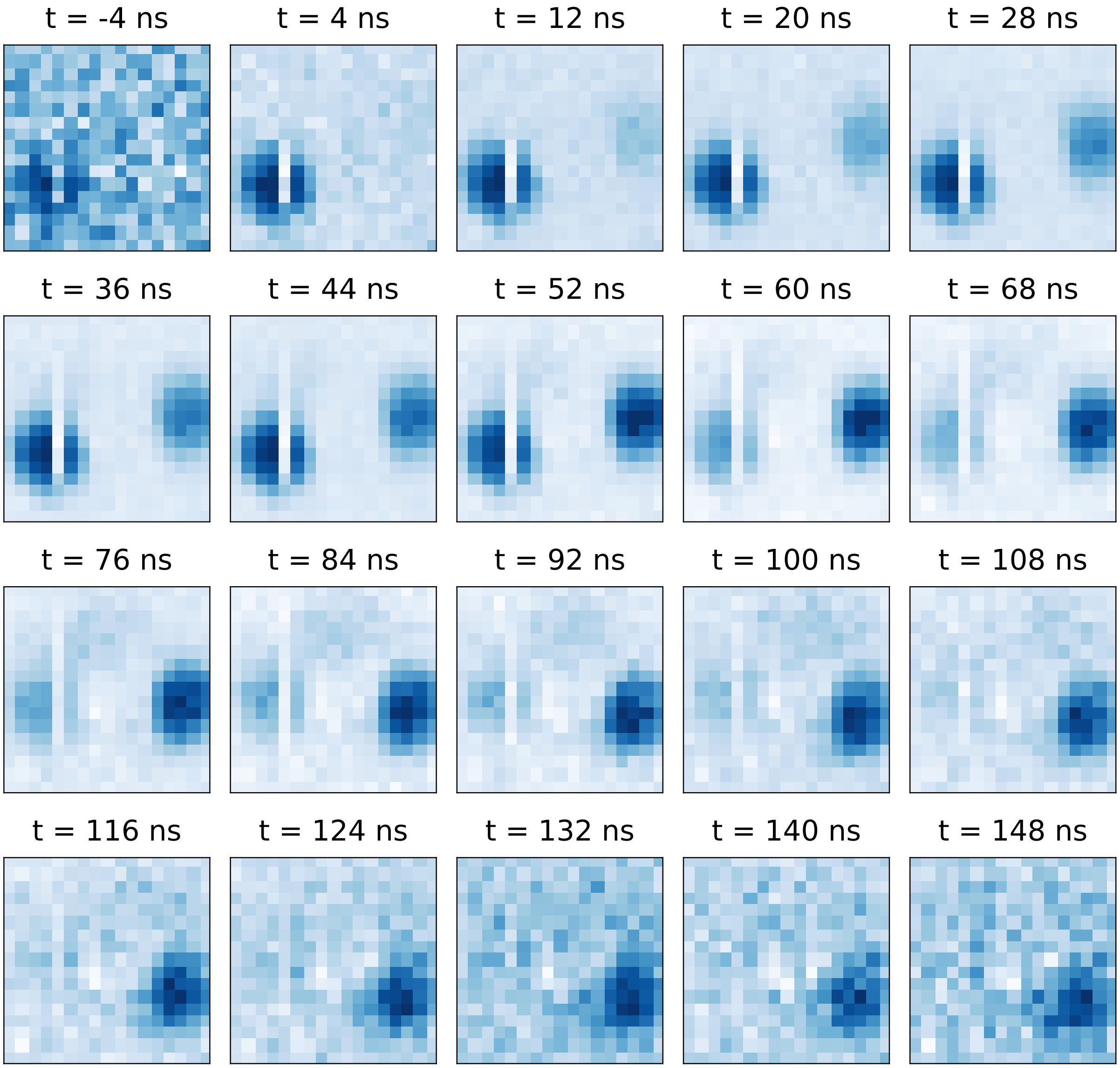

Figure 8.7: Implementing a non-local Floquet hamiltonian. The 2D oscillator 'science' cavity is coupled to a second degenerate confocal cavity (figure 8.6). The detunings are set such that the confocal cavity can be adiabatically eliminated, leading to Rabi-like oscillations of the particle in the 2D plane of interest. The rate of oscillation is set by the coupling rate of the cavities g (figure 8.6) and $\Delta/2\pi$, the detuning of the science cavity with respect to the confocal cavity odd/even manifolds, set to be equal to 0.25 FSR of the confocal cavity. The particle follows an anticlockwise trajectory, gets transported to the diametrically opposite end, and continues the anticlockwise motion. The vertical white stripe is a lock failure during the course of the data run.

8.2 Non-local potentials

8.2.1 Coupling to a confocal cavity

We implement a special class of non-local potentials of the form $V(\vec{x}, -\vec{x})$ by coupling the near-degenerate "science" cavity with a degenerate confocal cavity. In the limit that the detuning of the confocal cavity from the science cavity is $\gg$ TMS of the science cavity, the coupling introduces a dispersive shift in the science cavity, given by

$$H' = \sum_{n_{even}=0,2,4..}^{\infty} \frac{g^2}{\Delta} |n_{even}\rangle \langle n_{even}| - \sum_{n_{odd}=1,3,5..}^{\infty} \frac{g^2}{\Delta} |n_{odd}\rangle \langle n_{odd}| \tag{8.2}$$

where $g/2\pi = \sqrt{T \ \mathrm{FSR_{science}} \ \mathrm{FSR_{confocal}}}/2\pi$ and $\Delta/2\pi = \mathrm{FSR_{confocal}}/4$ is the detuning of the confocal cavity chosen such that the science modes lie equidistant in energy from the odd and even manifolds of the confocal cavity. In the position basis, the perturbation can be written as

$$H' = \frac{g^2}{\Delta} \int_A d^2\vec{x} \, (|\vec{x}\rangle \langle -\vec{x}| + |\vec{x}\rangle \langle -\vec{x}|) \tag{8.3}$$

showing the non-local potential in the science cavity implemented by the off-resonant coupling. In the limit that the rate $g^2/(\Delta) > \omega_{trap}$, an injected particle smoothly oscillates between $\vec{x}$ and diametrically opposite $-\vec{x}$ multiple times as it performs a 2D harmonic oscillation motion. This can be interpreted as a *spatial* Rabi oscillation between the two points. We could see the first half of a cycle in our experiment as shown in Fig 8.7, limited by the finesse of our science cavity.

---

2. It is interesting to note that any transverse plane of the cavity will show oscillator dynamics. The momenta in different planes are related via gauge transformations [131]

3. The finesse for this experiment is limited by the environmental dust conditions. Operating in a clean environment such as a flow bench would have improved the lifetime.

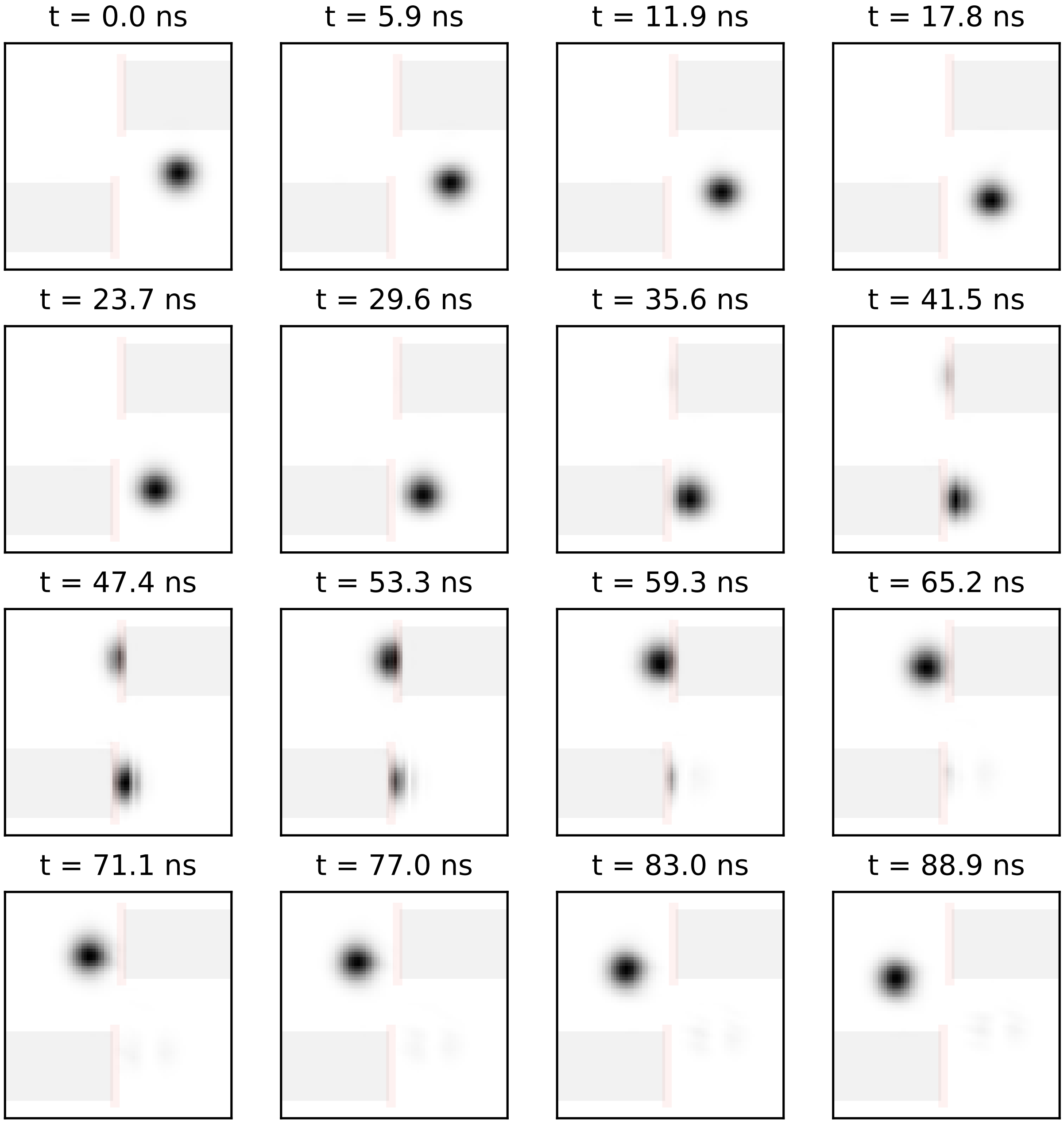

Figure 8.8: Simulation: creating a handle in space using setup shown in figure 8.9. The particle continues in a clockwise trajectory in the 2D harmonic well until it reaches a location where it couples to the confocal cavity and near-instantly (unlike the gradual Rabi-like-transfer in the previous figure) appears on the diametrically opposite end. The dynamics can be explained via constructive and destructive interferences as discussed in figure 8.10. The method of simulation is described in section 8.3.1.1 and the code is available at [132].

8.3 Future work

8.3.1 Near-instantaneous transfer of a synthetic light particle

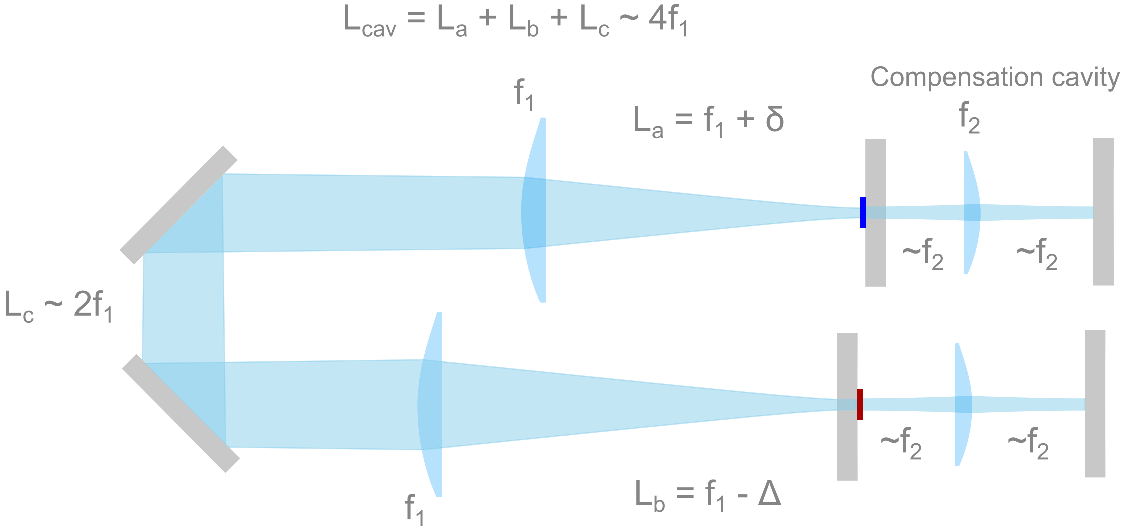

Figure 8.9: Cavities for designing a handle in 2D space. A localized phase-shift (figure 8.11b) is introduced in the main cavity to provide a local potential, and another localized phase-shift (figure 8.11c) is added to the confocal cavity. Together, the coupling and the phase-shifts break the odd-even symmetry of the science cavity in a way that the particle in the 2D plane appears to transfer through the localized region instantly (figure 8.8 and 8.10). A second compensation confocal cavity is added to *remove* the Rabi-like oscillations seen in figure 8.7, by detuning the science cavity in the other direction with respect to the odd and even modes of the second confocal cavity as compared to the first confocal cavity.

Finally, we would like to demonstrate near-instantaneous transfer of the particle to another point in the 2D plane when it reaches a particular point. The simulation is shown in figure 8.8. The goal of the experiment is to effectively change the geometry of the 2D space by creating a direct connection between two spatially well-separated points, and explore the dynamics of a massive particle on the new space. It requires a combination of ingredients (figure 8.9): the primary nearly-2D-degenerate cavity with a local phase-shift, a confocal cavity with a local phase-shift, and another compensation confocal cavity. The specific pattern of phase shifts is shown in figures 8.11, 8.12 and 8.13. The coupling to the

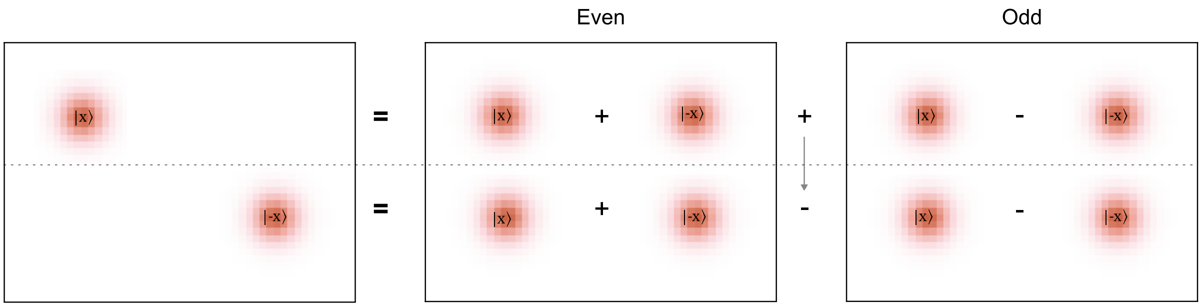

Figure 8.10: Building intuition for the nonlocal transport of the particle. We can decompose the science spatial wavepacket into superpositions of odd and even wavepackets. The coupling to the confocal cavity in the localized region makes the odd component reflect from the local potential with a different phase in the science cavity with respect to the even component, leading to a destructive *spatial* interference in the initial quadrant and a constructive *spatial* interference in the opposite quadrant, thus quickly transporting the particle across the space.

confocal cavity with the deposition breaks the odd-even symmetry of science cavity making the odd part of the wavepacket reflect with a $\sim \pi$ phase-shift with respect to the even part. This leads to a destructive interference in the initial location of the wavepacket and a constructive interference at the opposite point in space (figure 8.10), leading to a greater than 95% transfer of the wavepacket across space. The transfer happens almost instantaneously during the time of reflection.

8.3.1.1 Method of numerical simulation

The unperturbed Hamiltonian H_{sc} for the science cavity resembles that of a quantum harmonic oscillator with the diagonal terms $= (n+m) \times \omega_{\text{trap}}$, where $\omega_{\text{trap}} = 2\pi\times$ cavity transverse-mode spacing (TMS) is the trap frequency. The Hamiltonian $H_{\text{con, }1/2}$ for the confocal cavities is a diagonal matrix with two blocks, with identical diagonal elements within each block, corresponding to the energies of the odd and even modes. The effect of the deposition within individual cavities is modeled by calculating the spatial overlap of each of the spatial modes with the phase-shift profile $V(\vec{x})$: $\int_{-\infty}^{\infty} d^2\vec{x}\ \psi_a^*(\vec{x})V(\vec{x})\psi_b(\vec{x})$, where a and b are HG mode indices of modes of the *same* cavity. These terms are added to the off-diagonal terms of the unperturbed Hamiltonians H_{sc} and $H_{\mathrm{con,\ 1}}$. To couple these cavities, a super-Hamiltonian on the Hilbert space of all three cavities is constructed which has 3 blocks consisting of $H_{\mathrm{sc,\ p}}$, $H_{\mathrm{con,\ 1,\ p}}$ and $H_{\mathrm{con,\ 1}}$, where the subscript p implies that these Hamiltonians are perturbed by the depositions. The relative energies of the three cavities are set. The off-diagonal terms of the super-Hamiltonian are calculated via $g \int_{-\infty}^{\infty} d^2\vec{x}\ \psi_a^*(\vec{x})\psi_b(\vec{x})$, where a and b are now modes of *different* cavities. The integrals are calculated using `scipy` with C integration for faster evaluations. Once the super-Hamiltonian is ready, it is diagonalized to calculate the eigenvalues and eigenvectors. The initial injection, a displaced Gaussian formed by the superposition of higher-order modes, is calculated in the new eigenbasis and is evolved according to the new eigenenergies, to provide the dynamics shown in figure 8.8. The code is available at [132].

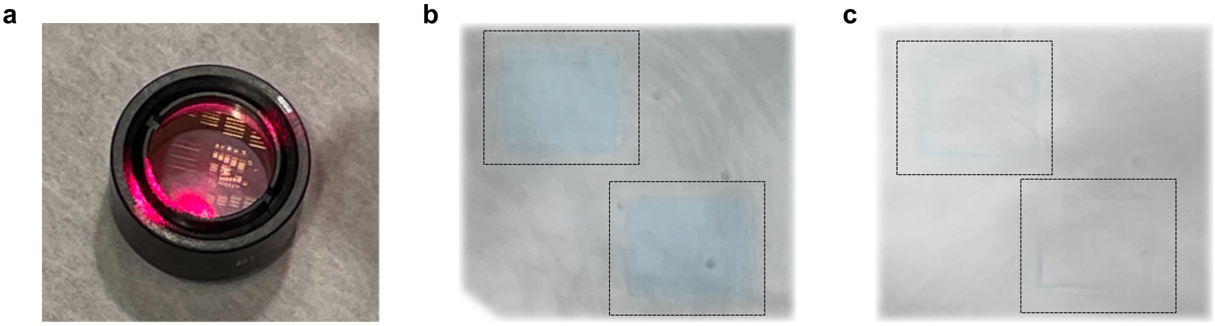

Figure 8.11: Mirror depositions. (a) Test mirror with the 1951 USAF resolution test chart patterned onto the substrate. The process involves (1) PR coating (2) photoresist pattern deposition (3) coating phase adjusting spacer (4) stripping photoresist. The pattern deposition was performed by Opto-line and the substrates and coating were provided by FiveNinesOptics. This mirror was used for local potential experiment shown in figure 8.5. (b) and (c) patterned mirrors for the planned experiment in section 8.3.1. The specifications for (b) and (c) are provided in figures 8.12 and 8.13 respectively.

8.3.1.2 Progress and potential improvements

While constructing the system, we ran into difficulties stabilizing the three cavities together due to mechanical vibrations in our setup which used optical components mounted on in-

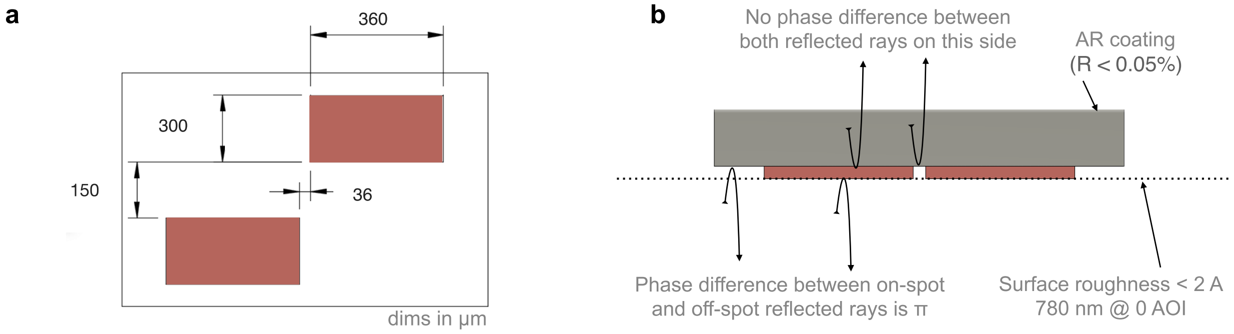

Figure 8.12: Specifications for local potential deposition shown in figure 8.11b for science cavity mirror.

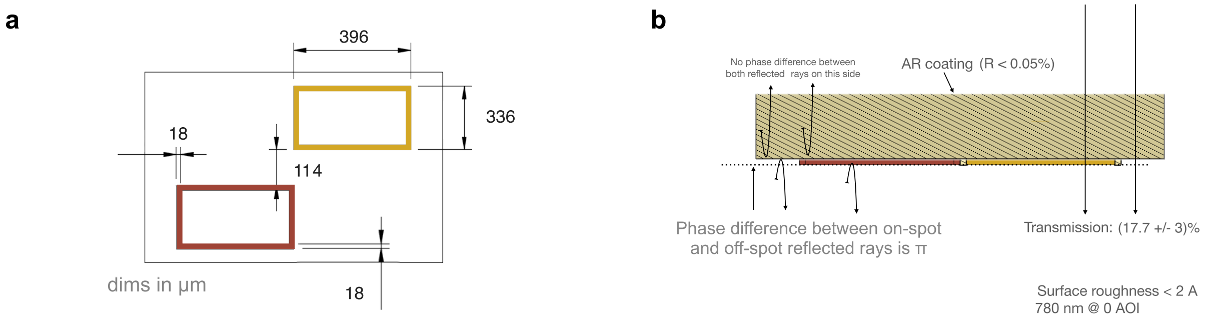

Figure 8.13: Specifications for nonlocal potential deposition shown in figure 8.11c for confocal cavity mirror.

dependent mounts and stages. Going forward, it will be helpful to design a monolithic structure for the cavities such that the parts don't vibrate independently and degrees of freedom can be restricted simplifying the alignment procedures. One possible pathway is to design a metallic platform with 3-axis flexure piezo-actuated mounts [32] to control the tip-tilt and cavity-axis-translation degrees of freedom for the intracavity lenses and tip-tilt control for the mirrors, with the flexure mounts screwed into the metallic platform to ensure coarse alignment and monolithicity. The design can be further improved by using mirrors and lenses coated for at least two more wavelengths, such that the other wavelengths can be used to lock the three cavities (In our current setup, we see interference effects despite using different polarizations). To observe the dynamics for longer time periods, we will need to operate in cleaner environment conditions to preserve the finesse of the cavities. Shorter cavities can also lead to more stable designs and faster dynamics. On the imaging front, it will be useful to have a two-dimensional detection scheme such as using a focusing lens and a fiber-array for simultaneously collecting data at multiple spatial locations.

8.3.2 Discussion

Exploring these geometries and observing the behaviour of synthetic matter therein can be helpful for understanding physical aspects of topology [125]. It will be interesting to observe the dynamics of a polariton – an atom or an atomic ensemble entangled with a cavity photon – in a nonlocal potential such as the one demonstrated in figure 8.7. Furthermore, the platform suggests a unique two-dimensional topology in the cavity plane that merits deeper theoretical investigation, such as the potential for non-trivial pathways connecting distant points [133], which could significantly influence our understanding of spatial connectivity within such systems.

Chapter 9

Outlook

The thesis began by discussing the cooperative enhancement of atom-field interactions through cavities and atomic ensembles, finding that (1) emission and absorption of light by an emitter such as an atom requires interaction with surrounding electromagnetic environment, (2) cavities, by confining the electromagnetic modes in space and frequency, significantly enhance this interaction, leading to stronger absorption from and emission into a mode compared to free-space. In Chapters 3-6, we explored how this feature of cavities can be used to effectively couple light with different frequencies. We explored two frequency regimes and two different mediators, an atomic ensemble and a non-linear crystal. Technologically, these two schemes combined can potentially cover a vast breadth of potentially integrable quantum systems, ranging from superconducting qubits to optical matter-based qubits such as atoms, ions, molecules and diamond centers.

In Chapter 7-8, we introduced more macroscopic intracavity optics, ranging from lenses, to lens arrays to phase modulating nonlinear crystals. Combined with low-to-moderate finesse, high-cooperativity cavities, these tools can be combined to enable a wide range of capabilities for information readout from quantum systems and its transfer in the form of photons.

Networking at telecom wavelengths: Efficient networking with photons requires minimizing transmission loss, and optical fiber attenuation is one of the key limiting factors. Figure 9.1 depicts the typical dependence of fiber attenuation on wavelength, showing the advantage of operating in the telecom regime. The most favorable region for long-distance quantum communication is the telecom C-band (around 1550 nm), where fiber attenuation is at its lowest and where existing classical communication infrastructure is already well established.

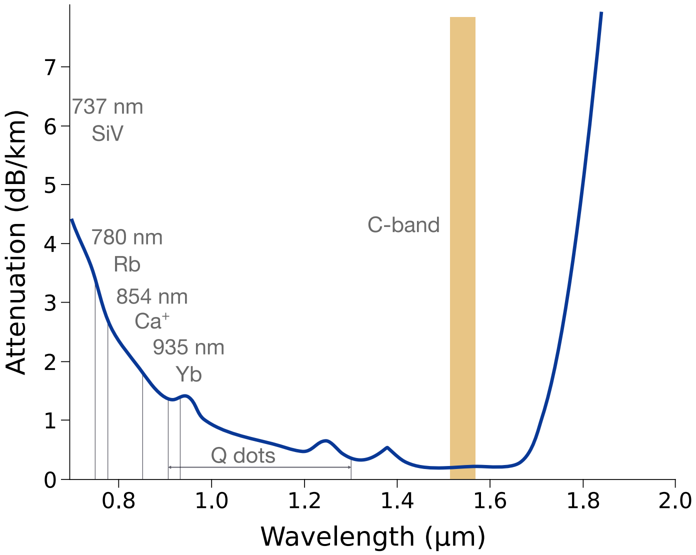

Figure 9.1: Fiber attenuation at different optical wavelengths. Curve adapted from [134].

The nonlinear crystal-coupled optical cavity, when designed and optimized for coupling between the telecom band and the emitter wavelength, can not only be used for efficient conversion, but can potentially also leverage the enhancement of emitter emission into a cavity mode directly into the telecom-band. Furthermore, coherent control over spatial modes can be explored for increasing information channel capacity through additional modes for encoding information. For the microwave transducer to convert into the telecom-band, one could consider using atoms with telecom transitions [135] or use the transducer in tandem with the optical transducer.

Tunable outcoupling: An etalon or a cavity can be used as a cavity-end-mirror with a tunable reflection coefficient [90]. The effect can be achieved by varying the length of the cavity and tuning it into or out of resonance with the frequency of interest. Varying the length via temperature or mechanical piezo-electric transducers is slow. In contrast, using nonlinear crystals with either RF- or optical modulation can enable much faster tunability of the outcoupler via the power and frequency of the RF- or optical- pumps. Such a capability already exists for superconducting qubits [136, 137] and can be utilized for tunable incoupling and outcoupling of a photon from an intracavity qubit, coupling two qubits, and performing quantum simulation experiments with multiple qubits [138].

Cavity atom arrays: Over the past decade, advances in controlling and manipulating arrays of individual atoms trapped in optical tweezers have established this platform as a strong contender for scalable quantum computing. Recently, a few works [20, 23, 97] have demonstrated the integration of an entire atom array within a single optical cavity, aiming to enable high-fidelity readout of atoms via the cavity and modular computing architectures. Combining high-NA resonator designs with microlens-array cavities could allow for individual cavity readout for each atom in the array, enabling greater control, speed and scalability. This is a very promising direction currently being pursued in the lab. The high-NA resonator also relaxes constraints on intracavity loss, making it feasible to introduce an intracavity $\chi^{(2)}$ crystal for tunable, site-selective outcoupling. These schemes could potentially offer a powerful approach to modular computing with neutral atom arrays.

Hybrid quantum systems: Coupled cavities offer interesting avenues for connecting disparate quantum platforms, enabling functionalities that are otherwise challenging to achieve. For instance, microwave-to-optical coupling scheme can bridge superconducting qubits and Rydberg atom arrays, leveraging the long coherence times of atomic states for quantum memory [139] while maintaining fast superconducting qubit processing. Similarly, the optical-to-optical coupling scheme can interface atomic arrays of different species [101] for midcircuit ancilla qubits or different platforms such atom arrays and diamond centers for processing and quantum memory.

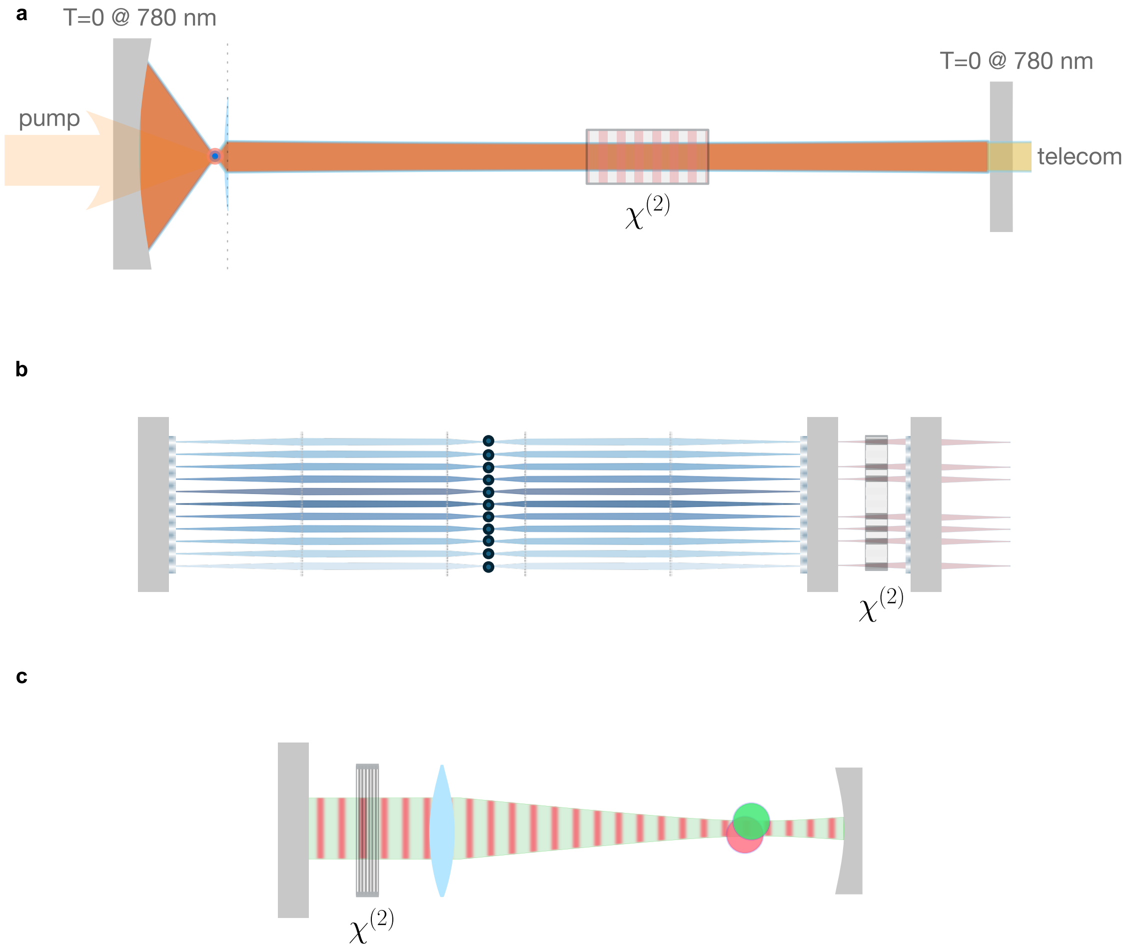

Figure 9.2: Envisioning cross-modality quantum interconnects. Cartoon representations for potential schemes (a) Integration of intracavity nonlinear crystal with high-NA resonator to readout at telecom wavelengths (b) Integration of microlens array with small waist cavity modes. Spatial patterning of applied voltage on a nonlinear crystal in a coupled cavity could enable site-selective, tunable outcoupler for the array. (c) Coupled doubly-resonant cavity for interactions with two atomic species.

Beyond these potential applications as quantum interconnects, the strengths of the diverse set of platforms could be useful for

1. **Metrology**: In addition to transduction, the demonstrated coupling between the millimeter-wave cavity and atoms opens avenues for constructing quantum-enhanced metrological states via spin-squeezing[1] and single-mmwave photon detectors for astronomy and dark-matter searches [140].

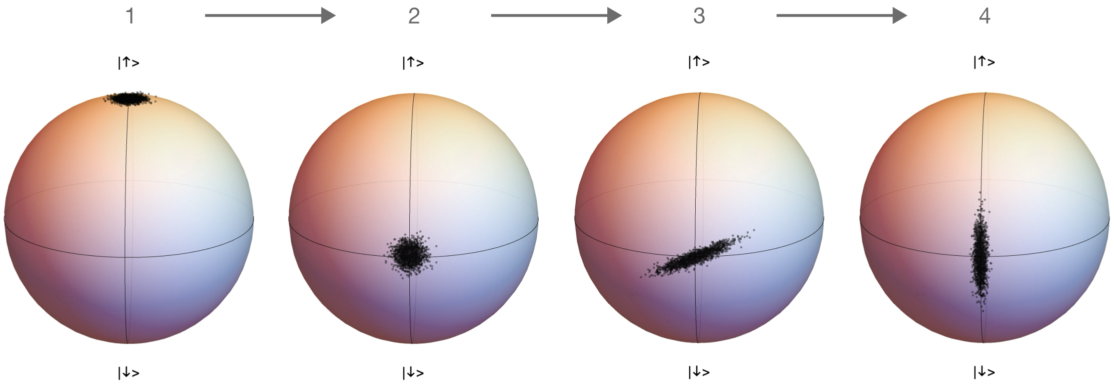

Figure 9.3: Semi-classical simulation of one-axis twisting of a coherent spin state of an atomic ensemble.

2. **Quantum simulation**: The degenerate twisted resonator is very promising for studies of the fractional quantum hall effect with light. Exploring coupled cavities and mirror perturbations add extra dimensions of versatility to cavity Floquet Hamiltonian engineering. Instead of a physical deposition on a mirror to induce a perturbation in the Floquet cavity Hamiltonian, one could also consider beam-shaping the optical pump beam in the coupled cavity resonator to create a perturbation. Beyond simulating these Hamiltonians, coupling of different longitudinal and transverse modes via RF modulation of cavities can lead to interesting simulation experiments in a synthetic

---

[1] This is a direction being pursued in the lab, using the hyperfine ground states of Rubidium as the clock states. The upper state can be Rydberg-dressed to the 35P state with the UV drive, and utilize the strong single-atom coupling at the millimeter-wave cavity to implement a one-axis-twisting Hamiltonian for the ensemble. A challenge has been getting a spatially uniform frozen magnetic field inside the superconducting cavity across the atomic cloud for high-fidelity Raman transitions between the ground-state clock states.

frequency dimension. Inducing coupling between disparate cavities in a lens-array cavity via spatially varying phases or a confocal configuration could be explored for lattice physics. Quantum simulation with dual-species atomic ensembles in coupled cavity modes will also be an interesting direction to explore.

With all these prospects, there remain key challenges such as addressing material losses, controlling and stabilizing complex systems, integrating with existing technologies, testing entanglement generation rates for networking and ensuring scalability. Nonetheless, the progress demonstrated in these prototypical experiments paves an optimistic exploration path for the future.

Appendix

A.1 ABCD matrices

A Gaussian mode can be described by the q-parameter [28], related to the beam waist w_0 and the Rayleigh range z_R as $q(z) = z + iz_R$. The beam waist w_0 is the minimum waist of the beam, and the Rayleigh range z_R is the distance over which the beam waist increases by a factor of $\sqrt{2}$ and is related to the waist by $z_R = \pi w_0^2/\lambda$. The radius of curvature $R(z)$ of the wavefront and the beam-size $w(z)$ can be extracted from $q(z)$ via the following relations

$$\begin{aligned} \frac{1}{q(z)} &= \frac{1}{R(z)} - \frac{i\lambda}{\pi n w(z)^2} \\ R(z) &= \frac{1}{\mathrm{Re}(q(z)^{-1})}, w(z) = \sqrt{-\frac{1}{\mathrm{Im}(q(z)^{-1})}\frac{\lambda}{\pi n}} \end{aligned} \tag{.1}$$

By definition, the cavity mode at a cavity plane with Gaussian parameter q, after a round-trip propagation through the cavity, should return to the same plane with the same Gaussian parameter up to a phase factor. This condition is satisfied by the ABCD matrix of the cavity, which is obtained by multiplying the ABCD matrices of individual components in the cavity including propagation. As an example, the ABCD matrix of a typical two-mirror cavity would be written as $M_{\mathrm{cav}} = M_{\mathrm{prop}}(L/2)M_{\mathrm{mir}}(R_2)M_{\mathrm{prop}}(L)M_{\mathrm{mir}}(R_1)M_{\mathrm{prop}}(L/2)$, where M_{mir} is the ABCD matrix for a mirror with radius of curvature R and $M_{\mathrm{prop}}(d)$ is the ABCD matrix for propagation over distance d. A list of commonly used ABCD matrices is provided in Appendix A.1.

The eigenmodes of the cavity are the solutions to the equation $M_{\text{cav}} \begin{pmatrix} q \\ 1 \end{pmatrix} = \alpha \begin{pmatrix} q \\ 1 \end{pmatrix}$. For a stable cavity, the eigenvalue α is of the form $e^{i\phi}$, where ϕ is the Gouy phase. The Gouy phase can be used to calculate the transverse mode spacing for the cavity as discussed in chapter 2. The cavity mode-size can be extracted from elements of $M_{\text{cav}} = \begin{pmatrix} A & B \\ C & D \end{pmatrix}$ as $w = \sqrt{\frac{|B|\lambda}{\pi}\sqrt{\frac{1}{1-(\frac{A+D}{2})^2}}}$. Note that this mode-size is at the plane M_{cav} is referenced to. So to calculate the mode-size for a two-mirror cavity at the end-mirror with radius of curvature R_1, the round-trip matrix should be calculated as $M_{\text{cav}} = M_{\text{prop}}(L)M_{\text{mir}}(R_2)M_{\text{prop}}(L)M_{\text{mir}}(R_1)$.

Matrix	**Description**
$\begin{pmatrix} 1 & d \\ 0 & 1 \end{pmatrix}$	Propagation over distance d
$\begin{pmatrix} 1 & 0 \\ -2/R & 1 \end{pmatrix}$	Reflection from a mirror with radius R, $R > 0$ for concave
$\begin{pmatrix} 1 & 0 \\ -1/f & 1 \end{pmatrix}$	Thin lens with focal length f
$\begin{pmatrix} 1 & 0 \\ \frac{n_1-n_2}{R\cdot n_2} & \frac{n_1}{n_2} \end{pmatrix}$	Refraction from medium with n_1 to n_2, $R \to \infty$ for plane interface, $R > 0$ for convex (center of curvature after interface)

Table A.1: Commonly used ABCD matrices.

A.2 Collective states

The operator algebra for a two-level atom is equivalent to that for a spin-1/2 particle with $j = 1/2$ once we make the identification $|g\rangle \equiv |1/2, -1/2\rangle$ and $|e\rangle \equiv |1/2, 1/2\rangle$. The angular orbital momentum operators are typically written using the Pauli-spin operators with $\{\hat{l}_x, \hat{l}_y, \hat{l}_z\} \equiv \hbar/2\{\hat{\sigma}_x, \hat{\sigma}_y, \hat{\sigma}_z\}$. They follow the commutation relations $[\hat{\sigma}_i, \hat{\sigma}_j] = 2i\epsilon_{ijk}\hat{\sigma}_k$. The anti-commutation relation $\{\hat{\sigma}_i, \hat{\sigma}_j\} = 2\delta_{ij}$ restrict the eigenvalues of $\hat{\sigma}_z$ to ± 1. The raising and lowering operators are defined as $\hat{\sigma}_{\pm} = \hat{\sigma}_x \pm i\hat{\sigma}_y$ and satisfy the anti-commutation relation $\{\hat{\sigma}_+, \hat{\sigma}_-\} = 1$. For an ensemble of N identical two-level atoms, the number of possible states is 2^N. Collective spin operators J's can be used to represent the internal state of the N atoms, with

$$\begin{aligned} \hat{J}_i &= \frac{1}{2}\sum_{j=1}^{N} \hat{\sigma}_i^{(j)}, with \\ \hat{J}^2 &= \hat{J}_x^2 + \hat{J}_y^2 + \hat{J}_z^2 \\ [\hat{J}_i, \hat{J}_j] &= i\epsilon_{ijk}\hat{J}_k \\ \hat{J}_{\pm} &= \hat{J}_x \pm i\hat{J}_y \\ [\hat{J}_+, \hat{J}_-] &= 2\hat{J}_z \end{aligned} \tag{.2}$$

Working in the J^2 and J_z basis, the collective states are $|J, M\rangle$ with $J = N/2, N/2 - 1, \ldots, 0$ and $M = -J, -J+1, \ldots, J$. However, only $J = N/2$ states form the $(N+1)$-sized fully symmetric subspace[1] And if we assume that the cavity field is completely uniform across the atomic ensemble (including phase), any interaction with the cavity field will move the internal state only in the symmetric subspace.

The Holstein-Primakoff transformation maps the collective spin operators to bosonic operators, where the spin operators, in terms of bosonic operators $a, a^\dagger$ can be defined as

$$\begin{aligned} \hat{J}_+ &= \hbar\sqrt{2 \times \frac{N}{2}}\sqrt{1 - \frac{\hat{a}^\dagger\hat{a}}{2 \times \frac{N}{2}}}\,\hat{a} \xrightarrow{N\to\infty} \hbar\sqrt{N}\,\hat{a} \\ \hat{J}_- &= \hbar\sqrt{2 \times \frac{N}{2}}\sqrt{1 - \frac{\hat{a}^\dagger\hat{a}}{2 \times \frac{N}{2}}}\,\hat{a}^\dagger \xrightarrow{N\to\infty} \hbar\sqrt{N}\,\hat{a}^\dagger \\ \hat{J}_z &= \hbar\left(\frac{N}{2} - \hat{a}^\dagger\hat{a}\right) \end{aligned} \tag{.3}$$

such that a state $|J = N/2, M\rangle$ can be written as $|J, M\rangle \to \frac{1}{\sqrt{J!}}(\hat{a}^\dagger)^{J-M}\,|0\rangle_B{}^2$, where $|0\rangle_B$

---

[1] For N identical spins, there can only be $N+1$ symmetric states, and repeatedly applying the symmetric lowering operator on the maximally symmetric state $|J = N/2, J_z = N/2\rangle$ gives $N+1$ symmetric states.

[2] The mapping can be done for $J \neq N/2$ subspace as well, but it should be an irreducible subspace

is the vacuum state of the bosonic operators.

In the limit of large N relative to the number of excitations, there is an exact one-to-one mapping between the bosonic operator and the collective spin operator, allowing us to write the collective states $|G\rangle = |gg\dots g\rangle \equiv |N/2\rangle_B$ and $|E\rangle = \frac{1}{\sqrt{N}}\sum_{i=1}^{N} |gg\dots e_i \dots gg\rangle \equiv |N/2-1\rangle_B$, as mentioned in the chapters. The symmetric collective states thus form a truncated harmonic oscillator ladder with $N+1$ levels, corresponding to the allowed excitations of the spin-$N/2$ system. The $\sqrt{N}$ collective enhancement in atom–cavity coupling is also evident from this calculation, where the term $\sum_{i=1}^{N} g_i\,|gg\dots e_i \dots gg\rangle$ in the multi-atom Jaynes–Cummings Hamiltonian can be replaced by $g\sqrt{N}\,|E\rangle$ when all atoms experience identical coupling to the cavity.

Note that for multilevel atomic ensembles, we can define this bosonic operators for each of the transitions, as we do for incorporating collective states $|R\rangle$ and $|F\rangle$.

A.3 Effect of ensemble temperature and 297 nm drive waist on Rabi frequency variation

We numerically simulated the effect of cloud temperature and UV beam size on UV Rabi oscillations between 5S and 35P state. We sample the Rabi frequency of atoms by sampling their positions in a 2D Gaussian cloud (atoms at different places will see a different UV field) and sample the detuning of atoms by sampling their velocities from a 1D Maxwell-Boltzmann distribution. We then calculate the generalized Rabi frequencies from these samples, and then average the excited state probabilities at a particular instant to get the overall ensemble population variation.

The numerics suggested (Fig A.1) that we are limited much more by inhomogeneous spread in Rabi frequencies than Doppler broadening. The flopping rate is mainly determined by bare Ω at resonance, which is significantly faster than Doppler broadening (maximum

Rabi frequency is about 1 MHz, and at 10 μK, the doppler shift distribution's FWHM is about 150 kHz around 0 kHz). This can also be seen from the generalized Rabi frequency expression ($\sqrt{\Omega^2 + \Delta^2}$) in the limit of $\Omega \gg \Delta$.

The effect of the UV beam waist on the Rabi oscillations is shown in figure A.2.

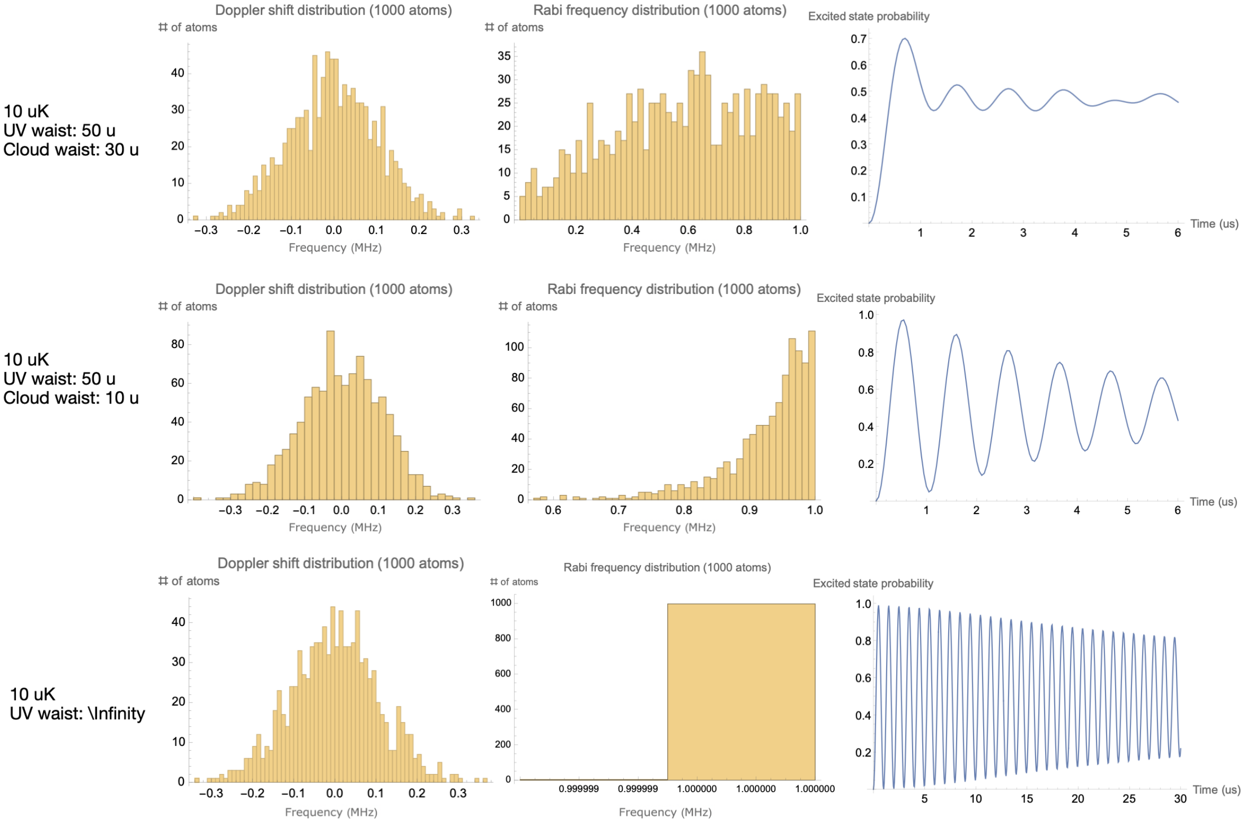

Figure A.1: Effect of ensemble temperature and 297 nm drive beam waist on Rydberg Rabi oscillations.

A.4 Intracavity 785 nm lattice

We tested a 785 nm cavity mode, co-resonant with the atomic resonance frequency at 780 nm, to form an intracavity standing-wave lattice and attempt to compress the atomic cloud for better contrast in UV Rabi oscillations. The maximum depth of the intracavity lattice was about 1 MHz, measured from an off-resonant vacuum Rabi splitting due to Stark shift of the

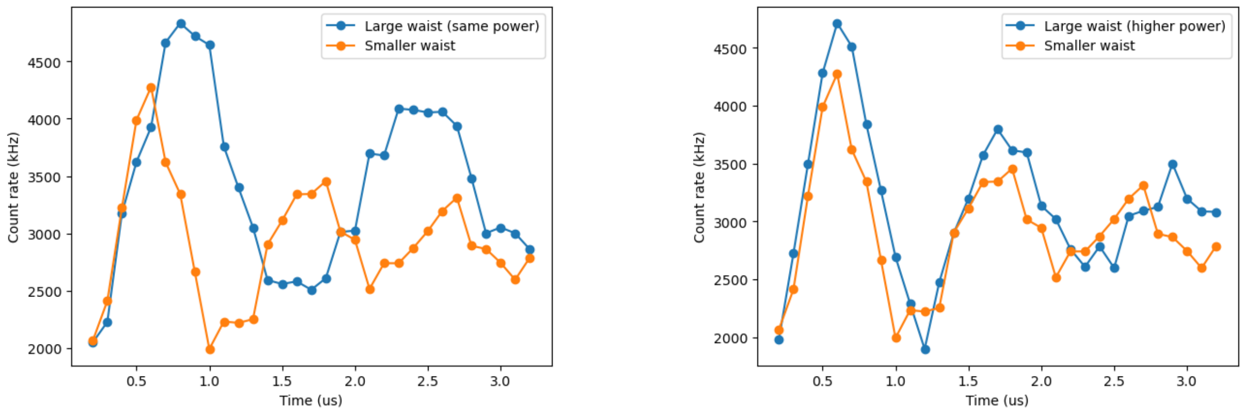

(a) (b)

Figure A.2: Effect of beam waist on Rabi oscillation contrast. Comparing oscillations at two waists with (a) equal drive power (b) unequal drive power.

atomic transition by the lattice.

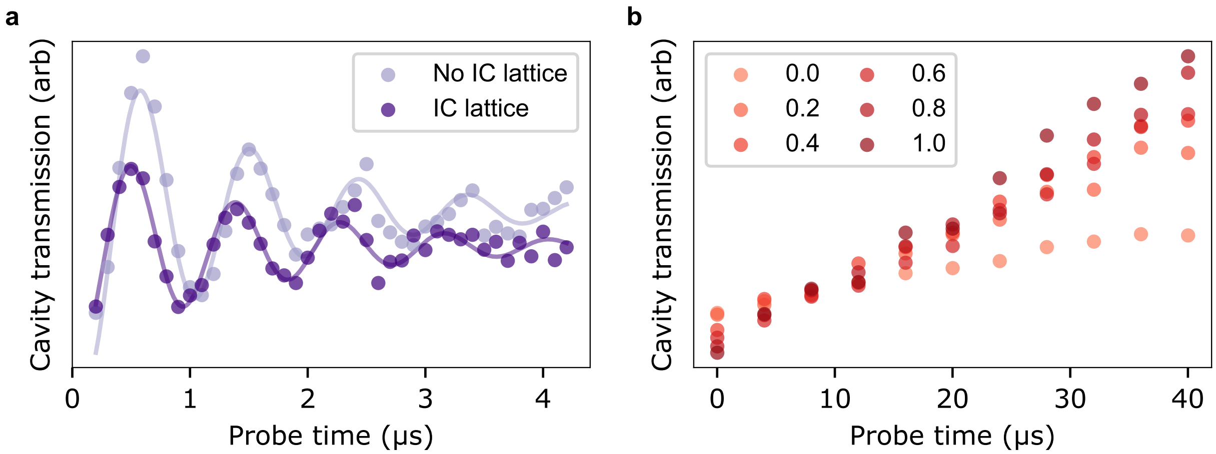

Figure A.3: Intracavity 785 nm lattice. (a) The lattice offers a slight improvement in Rabi oscillation contrast but due to high-frequency noise, heats atoms away quickly (b) especially as powers get higher

A.5 Coarse spectroscopy for Rydberg transitions

Blue: Following coarse tuning using a wavemeter to approximate the frequency predicted by the Python library `arc` [141], the blue frequency corresponding to the Rydberg transition is identified using free-space EIT spectroscopy A.4. A 780 nm laser locked to a reference laser, with frequency corresponding to the 5S1/2 to 5P3/2 transition, is directed into a Rubidium vapor cell and its frequency is swept across the broad resonance, with the transmitted light being collected to reveal an absorption dip around the resonance. A single-frequency 481 nm laser beam is counterpropagated into the vapor cell, and the laser's frequency is finely tuned. A small peak emerges when the two-photon resonance condition is satisfied. The frequency corresponding to this feature is then used to set the appropriate 962 nm lock feature on the transfer cavity.

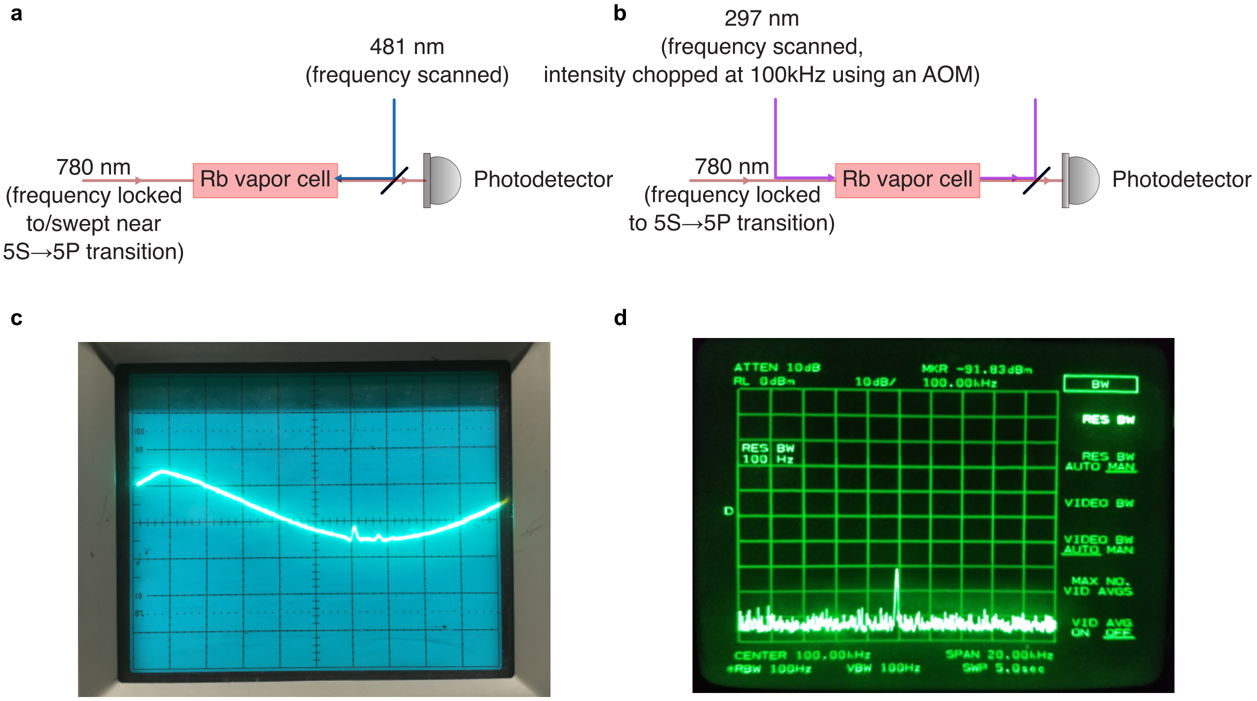

Figure A.4: Vapor cell spectroscopy for Rydberg transitions

UV: A depletion spectroscopy technique is applied for the UV transition by exploiting the shorter lifetime of the 5P3/2 state compared to the Rydberg state A.4. Under simultaneous excitation of 5S atoms to the 5P state and the Rydberg state, atoms reside predominantly in the Rydberg state, resulting in higher transmission of resonant 780 nm light through the vapor cell. Because the signal is small due to weak coupling, lock-in detection is employed: the UV beam is modulated at 100 kHz with an AOM TTL signal, and the 780 nm transmission is recorded on a spectrum analyzer as the UV laser current/voltage is tuned. The 780 nm intensity is maintained below saturation. The photodiode signal is demodulated to reveal a peak versus the UV frequency, aiding in locating the correct sideband on the 1188 nm transfer cavity transmission.

A.6 Thermal photon state and coherent state statistics

We begin by expressing the photon creation and annihilation operators in terms of the photon operators of N individual atoms with uncorrelated phases ϕ_i:

$$\hat{a}^\dagger = \frac{1}{\sqrt{N}} \sum_{i=1}^{N} \hat{a}_i^\dagger e^{-i\phi_i}, \quad \hat{a} = \frac{1}{\sqrt{N}} \sum_{i=1}^{N} \hat{a}_i e^{i\phi_i}.$$

We now calculate the expectation value of $(\hat{a}^\dagger)^k \hat{a}^l$ to help us calculate the correlation function $g^{(2)}(0) = \frac{\langle (\hat{a}^\dagger)^2 \hat{a}^2 \rangle}{\langle \hat{a}^\dagger \hat{a} \rangle^2}$ later:

$$\langle (\hat{a}^\dagger)^k \hat{a}^l \rangle = \frac{1}{\sqrt{N}^{l+k}} \sum_{i_1,\ldots,i_k=1}^{N} \sum_{j_1,\ldots,j_l=1}^{N} \langle \hat{a}_{i_1}^\dagger e^{-i\phi_{i_1}} \ldots \hat{a}_{i_k}^\dagger e^{-i\phi_{i_k}} \hat{a}_{j_1} e^{i\phi_{j_1}} \ldots \hat{a}_{j_l} e^{i\phi_{j_l}} \rangle.$$

We average over many realizations of the phases ϕ_i. Since the phases are uncorrelated, the only nonzero terms in the sum arise when for each $e^{i\phi_i}$ there is a conjugate $e^{-i\phi_i}$ from the same atom/source, so the annihilation operators correspond to the same atoms as the creation operators, even though they might be ordered differently. Also, in each realization, a single atom emits only a single photon, disallowing terms with more than one creation/annihilation operator from the same atom. This reduces the summation to a counting problem: there are $\frac{N!}{(N-k)!}$ ways for choosing an arranging k creation operators out of N operators, and then for each of those ways, $k!$ ways of arranging the annihilation operators corresponding to the chosen creation operators/atoms. Assuming that the expectation values for individual photons are the same across all atoms, each average term can be separated for individual atoms and with $\langle \hat{a}_i^\dagger \hat{a}_i \rangle = \bar{n}$ and the discussion earlier, the previous expression can be simplified to

$$\langle (\hat{a}^\dagger)^k \hat{a}^l \rangle = \delta_{kl} \frac{1}{N^k} \cdot \frac{N!}{(N-k)!} k! \bar{n}^k.$$

Applying Stirling's approximation $\frac{N!}{(N-k)!} \approx N^k$ for large N simplifies the expectation value to:

$$\langle (\hat{a}^\dagger)^k \hat{a}^l \rangle = \delta_{kl} k! \bar{n}^k.$$

giving

$$g_{th}^{(2)}(0) = \frac{\langle (a^\dagger)^2 a^2 \rangle}{\langle a^\dagger a \rangle^2} = \frac{2\bar{n}^2}{\bar{n}^2} = 2$$

For coherent states, the mean number of photons $\langle n \rangle$ is equal to the variance $= \langle n^2 \rangle - \langle n \rangle^2$. Using the commutation relation $[a^\dagger, a] = 1$ and $\langle a^\dagger a \rangle = \langle n \rangle$, $\langle (a^\dagger)^2 a^2 \rangle$ simplifies to $\langle n^2 \rangle - \langle n \rangle$, and we can write for a coherent state

$$g_{coh}^{(2)}(0) = \frac{\langle (a^\dagger)^2 a^2 \rangle}{\langle a^\dagger a \rangle^2} = \frac{\langle n^2 \rangle - \langle n \rangle}{\langle n \rangle^2} = 1$$

The expression for a coherently displaced thermal state is calculated in the main text.

A.7 Cavity Rydberg EIT at higher Rydberg levels

Figure A.5 show cavity Rydberg EIT with higher Rydberg states, with the corresponding fit parameters shown in table A.2.

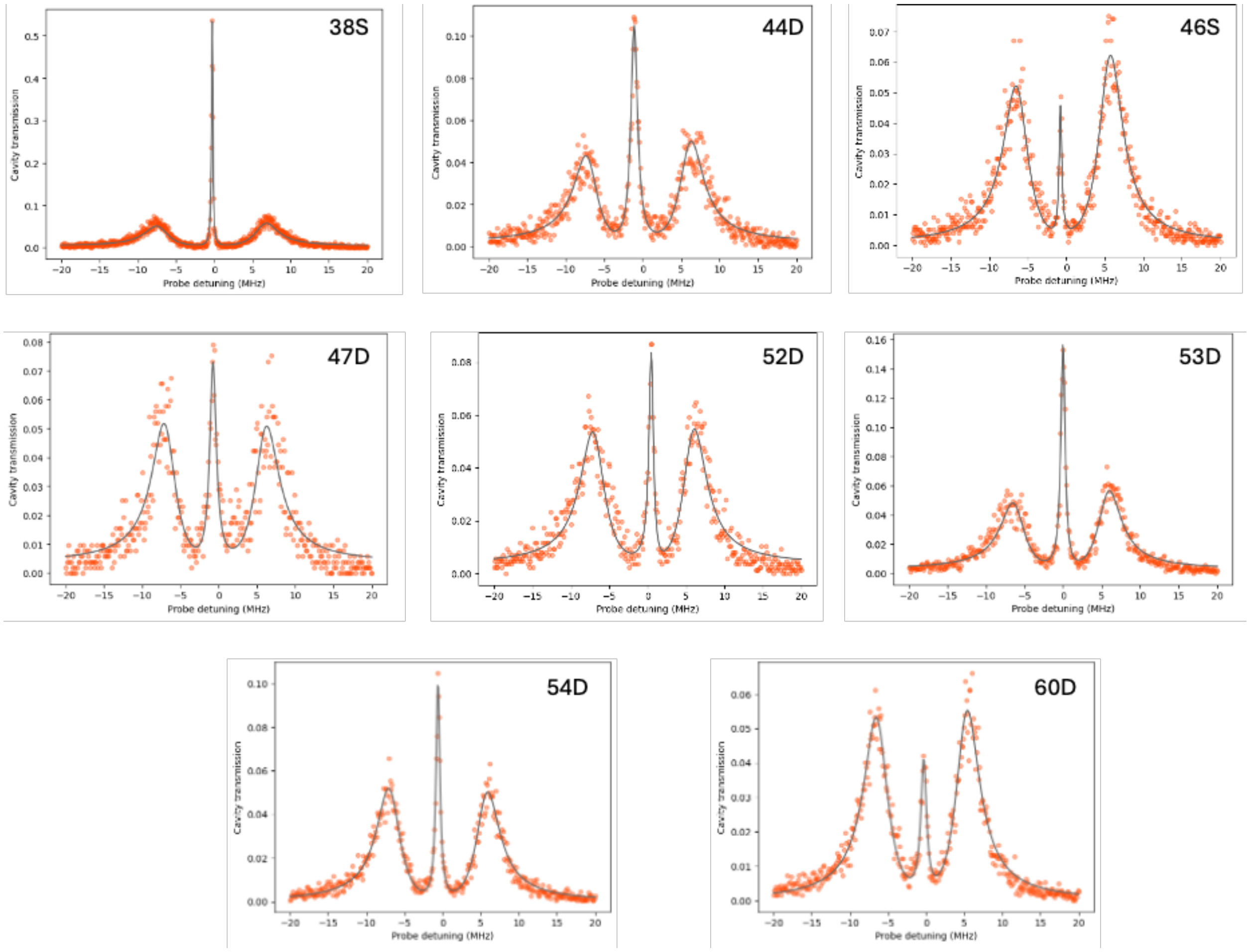

Figure A.5: EIT scan for higher Rydberg levels. The x-axis corresponds to the 780 nm probe frequency around the bare cavity resonance, and the y-axis corresponds to the cavity transmission. The fitted parameters are displayed in table A.2.

Rydberg state	$\{G_{opt}, \Omega_b, \Gamma_r\}$
38S	$2\pi \times \{6.7, 2.1, 0.063\}$ MHz
44D	$2\pi \times \{6.0, 2.8, 0.897\}$ MHz
46S	$2\pi \times \{5.9, 1.2, 0.367\}$ MHz
47D	$2\pi \times \{6.1, 2.4, 0.926\}$ MHz
52D	$2\pi \times \{6.1, 2.0, 0.576\}$ MHz
53D	$2\pi \times \{5.6, 2.3, 0.495\}$ MHz
54D	$2\pi \times \{6.0, 2.1, 0.499\}$ MHz
60D	$2\pi \times \{5.6, 1.7, 0.840\}$ MHz

Table A.2: Fitted $G_{opt}, \Omega_b, \Gamma_r$ for Rydberg EIT with higher Rydberg levels.

A.8 Calculating two-cavity-mode coupling strength g

It is assumed that $\delta_E, \delta_R \gg \Omega_p, \Gamma_R, \Gamma_E$. For an atom at r_i, the coupling terms in the Hamiltonian for crystal-coupled cavities can be written as

$$\begin{aligned} G_\alpha(\vec{r}_i) &= \frac{\mu_\alpha}{\hbar}\sqrt{\frac{\hbar\omega_\alpha}{2\epsilon_0 A_\alpha L}} f_\alpha(\vec{r}_i) \\ \Omega_p(\vec{r}_i) &= \frac{\mu_p E_{pump}}{\hbar} \end{aligned}$$

where A_α is the effective mode area for a travelling wave mode, L is the length of the cavity, and $f_\alpha(r)$ incorporates the spatial variation of the mode. Summing over all the atoms in the crystal volume and identifying the expression for the second-order susceptibility $\chi^{(2)}$ [72],

$$\begin{aligned} g = &\left(\chi^{(2)} \frac{\sqrt{\omega_a\omega_b}}{c\sqrt{n_a n_b}} L_{\text{crystal}} |E_{pump}|\right) \\ &\left(\frac{\sqrt{n_a n_b}}{L_{\text{crystal}}\sqrt{A_a A_b}} \int_{V_{\text{crystal}}} dV f_a(\vec{r}) f_b(\vec{r}) f_{pump}(\vec{r})\right) \frac{c}{2L} \end{aligned}$$

where the integral includes the phase matching factor. Identifying the free-spectral range leaves us with

$$g = \sqrt{\epsilon' \Phi^2}\ \frac{c}{2L} = \sqrt{\epsilon}\ \nu \tag{.4}$$

where ϵ can be interpreted as the single-pass conversion efficiency of the crystal ϵ' [72] modified by the spatial overlap factor Φ, and ν is the cavity free-spectral range. Note: (1) This model assumes that the crystal does not significantly modify the cavity mode field amplitude. The predicted values from this model for our platform are within a factor of 3 of the value observed in experiments. For a more accurate analysis, the mode volumes should be calculated for the part-dielectric cavity, which will scale g accordingly. This model provides an upper bound on the absolute value but captures the dependence of coupling on beam waists which affect both the conversion efficiency (by affecting pump field strength at a given power) and the spatial overlap (Figure 5.10a and Sec 5.8). (2) For a more accurate modeling of the crystal $\chi^{(2)}$, other permutations of atomic levels need to be included [72]. It does not affect the final expression for g.

A.9 Spatial overlap factor for single-pass conversion efficiency using Gaussian modes with arbitrary waists

Reference [94] theoretically analyzes the conversion efficiency for SFG processes with Gaussian beams. The spatial overlap factor h, for single-pass conversion (no cavity) is

$$\begin{aligned} h &= \frac{1}{4\xi_4} I \\ I &= \int_0^1 \int_0^1 dz_1 dz_2 \frac{\exp[i\Delta k(z_1 - z_2)]}{(z_1 - A_1)(z_2 - A_1^*) + C_1} \end{aligned} \tag{.5}$$

$$k_i = \frac{2\pi n_i}{\lambda_i}, \quad b_i = w_{oi} k_i, \quad k = \frac{k_1}{k_2} \tag{.6}$$

$$\xi_1 = \frac{l}{b_1}, \quad \xi_2 = \frac{l}{b_2}, \quad \xi_3 = \frac{\xi_1 \xi_2 (1+k)}{\xi_2 + k\xi_1}, \quad \xi_4 = \frac{\xi_1 + k\xi_2}{1+k}, \tag{.7}$$

$$A_1 = \frac{1}{2} + \frac{i}{4}\left(\frac{1}{\xi_3} + \frac{1}{\xi_4}\right), \quad C_1 = -\frac{1}{16}\left(\frac{1}{\xi_3} - \frac{1}{\xi_4}\right)^2 \tag{.8}$$

Bibliography

[1] C. A. Kocher and E. D. Commins, “Polarization Correlation of Photons Emitted in an Atomic Cascade”, Physical Review Letters **18**, 575–577 (1967) (cited on p. 1).

[2] A. Aspect, P. Grangier, and G. Roger, “Experimental Realization of Einstein-Podolsky-Rosen-Bohm Gedankenexperiment: A New Violation of Bell’s Inequalities”, Physical Review Letters **49**, 91–94 (1982) (cited on p. 1).

[3] S. J. Freedman and J. F. Clauser, “Experimental Test of Local Hidden-Variable Theories”, Physical Review Letters **28**, 938–941 (1972) (cited on p. 1).

[4] S. Haroche, “Nobel Lecture: Controlling photons in a box and exploring the quantum to classical boundary”, Reviews of Modern Physics **85**, 1083–1102 (2013) (cited on pp. 1, 3).

[5] A. Ashkin, “Acceleration and Trapping of Particles by Radiation Pressure”, Physical Review Letters **24**, 156–159 (1970) (cited on p. 1).

[6] P. W. H. Pinkse, T. Fischer, P. Maunz, and G. Rempe, “Trapping an atom with single photons”, Nature **404**, 365–368 (2000) (cited on p. 1).

[7] A. M. Kaufman, B. J. Lester, and C. A. Regal, “Cooling a Single Atom in an Optical Tweezer to Its Quantum Ground State”, Physical Review X **2**, 041014 (2012) (cited on p. 1).

[8] S. Chu, J. E. Bjorkholm, A. Ashkin, and A. Cable, “Experimental Observation of Optically Trapped Atoms”, Physical Review Letters **57**, 314–317 (1986) (cited on p. 1).

[9] D. Awschalom, K. K. Berggren, H. Bernien, S. Bhave, L. D. Carr, P. Davids, S. E. Economou, D. Englund, A. Faraon, M. Fejer, S. Guha, M. V. Gustafsson, E. Hu, L. Jiang, J. Kim, B. Korzh, P. Kumar, P. G. Kwiat, M. Lončar, M. D. Lukin, D. A. Miller, C. Monroe, S. W. Nam, P. Narang, J. S. Orcutt, M. G. Raymer, A. H. Safavi-Naeini, M. Spiropulu, K. Srinivasan, S. Sun, J. Vučković, E. Waks, R. Walsworth, A. M. Weiner, and Z. Zhang, “Development of Quantum Interconnects (QuICs) for Next-Generation Information Technologies”, PRX Quantum **2**, 017002 (2021) (cited on p. 1).

[10] L. Ding, M. Hays, Y. Sung, B. Kannan, J. An, A. Di Paolo, A. H. Karamlou, T. M. Hazard, K. Azar, D. K. Kim, B. M. Niedzielski, A. Melville, M. E. Schwartz, J. L. Yoder, T. P. Orlando, S. Gustavsson, J. A. Grover, K. Serniak, and W. D. Oliver, “High-Fidelity, Frequency-Flexible Two-Qubit Fluxonium Gates with a Transmon Coupler”, Physical Review X **13**, 031035 (2023) (cited on p. 2).

[11] C. E. Bradley, J. Randall, M. H. Abobeih, R. C. Berrevoets, M. J. Degen, M. A. Bakker, M. Markham, D. J. Twitchen, and T. H. Taminiau, “A Ten-Qubit Solid-State Spin Register with Quantum Memory up to One Minute”, Physical Review X **9**, 031045 (2019) (cited on p. 2).

[12] F. Adler, M. J. Thorpe, K. C. Cossel, and J. Ye, “Cavity-Enhanced Direct Frequency Comb Spectroscopy: Technology and Applications”, Annual Review of Analytical Chemistry **3**, 175–205 (2010) (cited on p. 3).

[13] A. Karpf, Y. Qiao, and G. N. Rao, “Ultrasensitive, real-time trace gas detection using a high-power, multimode diode laser and cavity ringdown spectroscopy”, Applied Optics **55**, 4497–4504 (2016) (cited on p. 3).

[14] M. H. Schleier-Smith, “Cavity-enabled spin squeezing for a quantum-enhanced atomic clock”, Thesis (Massachusetts Institute of Technology, 2011) (cited on p. 3).

[15] G. P. Greve, C. Luo, B. Wu, and J. K. Thompson, “Entanglement-enhanced matter-wave interferometry in a high-finesse cavity”, Nature **610**, 472–477 (2022) (cited on p. 3).

[16] Z. Li, S. Colombo, C. Shu, G. Velez, S. Pilatowsky-Cameo, R. Schmied, S. Choi, M. Lukin, E. Pedrozo-Peñafiel, and V. Vuletić, “Improving metrology with quantum scrambling”, Science **380**, 1381–1384 (2023) (cited on p. 3).

[17] C. D. Panda, M. Tao, J. Egelhoff, M. Ceja, V. Xu, and H. Müller, “Coherence limits in lattice atom interferometry at the one-minute scale”, Nature Physics **20**, 1234–1239 (2024) (cited on p. 3).

[18] S. Welte, B. Hacker, S. Daiss, S. Ritter, and G. Rempe, “Photon-Mediated Quantum Gate between Two Neutral Atoms in an Optical Cavity”, Physical Review X **8**, 011018 (2018) (cited on p. 3).

[19] C. K. Law and H. J. Kimble, “Deterministic generation of a bit-stream of single-photon pulses”, Journal of Modern Optics **44**, 2067–2074 (1997) (cited on p. 3).

[20] B. Grinkemeyer, E. Guardado-Sanchez, I. Dimitrova, D. Shchepanovich, G. E. Mandopoulou, J. Borregaard, V. Vuletić, and M. D. Lukin, *Error-Detected Quantum Operations with Neutral Atoms Mediated by an Optical Cavity*, Oct. 2024 (cited on pp. 3, 17, 135).

[21] Z. Yan, J. Ho, Y.-H. Lu, S. J. Masson, A. Asenjo-Garcia, and D. M. Stamper-Kurn, “Superradiant and Subradiant Cavity Scattering by Atom Arrays”, Physical Review Letters **131**, 253603 (2023) (cited on p. 3).

[22] Y. Liu, Z. Wang, P. Yang, Q. Wang, Q. Fan, S. Guan, G. Li, P. Zhang, and T. Zhang, "Realization of Strong Coupling between Deterministic Single-Atom Arrays and a High-Finesse Miniature Optical Cavity", Physical Review Letters **130**, 173601 (2023) (cited on p. 3).

[23] B. Hu, J. Sinclair, E. Bytyqi, M. Chong, A. Rudelis, J. Ramette, Z. Vendeiro, and V. Vuletić, *Site-selective cavity readout and classical error correction of a 5-bit atomic register*, Sept. 2024 (cited on pp. 3, 17, 135).

[24] E. Deist, Y.-H. Lu, J. Ho, M. K. Pasha, J. Zeiher, Z. Yan, and D. M. Stamper-Kurn, "Mid-Circuit Cavity Measurement in a Neutral Atom Array", Physical Review Letters **129**, 203602 (2022) (cited on pp. 3, 103).

[25] A. Kumar, A. Suleymanzade, M. Stone, L. Taneja, A. Anferov, D. I. Schuster, and J. Simon, "Quantum-enabled millimetre wave to optical transduction using neutral atoms", Nature **615**, 614–619 (2023) (cited on pp. 3, 18, 23, 24, 51).

[26] L. Taneja, D. I. Schuster, and J. Simon, *Light-controlled strong coupling of optical cavity modes spaced by 200 THz*, Mar. 2025 (cited on pp. 4, 64).

[27] *Atom—Photon Interactions* (John Wiley & Sons, Ltd, 1998) (cited on p. 6).

[28] A. E. Siegman, *Lasers* (University Science Books, 1986) (cited on pp. 6, 7, 100, 101, 118, 139).

[29] *Photons and Atoms* (John Wiley & Sons, Ltd, 1997) (cited on p. 6).

[30] D. Steck, *Quantum and Atom Optics* (available online) (cited on pp. 6, 9, 13, 68, 69).

[31] J. Simon, "Cavity QED with atomic ensembles", PhD thesis (Harvard University, Massachusetts, Jan. 2010) (cited on p. 15).

[32] D. Shadmany, A. Kumar, A. Soper, L. Palm, C. Yin, H. Ando, B. Li, L. Taneja, M. Jaffe, S. David, and J. Simon, "Cavity QED in a high NA resonator", Science Advances **11**, eads8171 (2025) (cited on pp. 15, 17, 81, 84, 105, 106, 132).

[33] H. Tanji-Suzuki, I. D. Leroux, M. H. Schleier-Smith, M. Cetina, A. T. Grier, J. Simon, and V. Vuletić, "Chapter 4 - Interaction between Atomic Ensembles and Optical Resonators: Classical Description", in *Advances In Atomic, Molecular, and Optical Physics*, Vol. 60, edited by E. Arimondo, P. R. Berman, and C. C. Lin, Advances in Atomic, Molecular, and Optical Physics (Academic Press, Jan. 2011), pp. 201–237 (cited on p. 16).

[34] P. Bertet, A. Auffeves, P. Maioli, S. Osnaghi, T. Meunier, M. Brune, J. M. Raimond, and S. Haroche, "Direct Measurement of the Wigner Function of a One-Photon Fock State in a Cavity", Physical Review Letters **89**, 200402 (2002) (cited on p. 17).

[35] A. Suleymanzade, A. Anferov, M. Stone, R. K. Naik, A. Oriani, J. Simon, and D. Schuster, "A tunable high-Q millimeter wave cavity for hybrid circuit and cavity QED experiments", Applied Physics Letters **116**, 104001 (2020) (cited on p. 17).

[36] G. Rempe, R. J. Thompson, H. J. Kimble, and R. Lalezari, "Measurement of ultralow losses in an optical interferometer", Optics Letters **17**, 363–365 (1992) (cited on p. 17).

[37] R. J. Thompson, G. Rempe, and H. J. Kimble, "Observation of normal-mode splitting for an atom in an optical cavity", Physical Review Letters **68**, 1132–1135 (1992) (cited on p. 17).

[38] C. J. Hood, H. J. Kimble, and J. Ye, "Characterization of high-finesse mirrors: Loss, phase shifts, and mode structure in an optical cavity", Physical Review A **64**, 033804 (2001) (cited on p. 17).

[39] K. Durak, C. H. Nguyen, V. Leong, S. Straupe, and C. Kurtsiefer, "Diffraction-limited Fabry–Perot cavity in the near concentric regime", New Journal of Physics **16**, 103002 (2014) (cited on p. 17).

[40] D. Hunger, T. Steinmetz, Y. Colombe, C. Deutsch, T. W. Hänsch, and J. Reichel, "A fiber Fabry–Perot cavity with high finesse", New Journal of Physics **12**, 065038 (2010) (cited on pp. 17, 103).

[41] J. C. Bardin, D. H. Slichter, and D. J. Reilly, "Microwaves in quantum computing", IEEE Journal of Microwaves **1**, 403–427 (2021) (cited on p. 18).

[42] Z.-L. Xiang, M. Zhang, L. Jiang, and P. Rabl, "Intracity Quantum Communication via Thermal Microwave Networks", Physical Review X **7**, 011035 (2017) (cited on p. 18).

[43] F. Fesquet, F. Kronowetter, M. Renger, W. K. Yam, S. Gandorfer, K. Inomata, Y. Nakamura, A. Marx, R. Gross, and K. G. Fedorov, "Demonstration of microwave single-shot quantum key distribution", Nature Communications **15**, 7544 (2024) (cited on p. 18).

[44] Z.-L. Xiang, S. Ashhab, J. Q. You, and F. Nori, "Hybrid quantum circuits: Superconducting circuits interacting with other quantum systems", Reviews of Modern Physics **85**, 623–653 (2013) (cited on p. 19).

[45] R. W. Andrews, R. W. Peterson, T. P. Purdy, K. Cicak, R. W. Simmonds, C. A. Regal, and K. W. Lehnert, "Bidirectional and efficient conversion between microwave and optical light", Nature Physics **10**, 321–326 (2014) (cited on pp. 19, 64).

[46] A. P. Higginbotham, P. S. Burns, M. D. Urmey, R. W. Peterson, N. S. Kampel, B. M. Brubaker, G. Smith, K. W. Lehnert, and C. A. Regal, "Harnessing electro-optic correlations in an efficient mechanical converter", Nature Physics **14**, 1038–1042 (2018) (cited on p. 19).

[47] T. Bagci, A. Simonsen, S. Schmid, L. G. Villanueva, E. Zeuthen, J. Appel, J. M. Taylor, A. Sørensen, K. Usami, A. Schliesser, and E. S. Polzik, "Optical detection of radio waves through a nanomechanical transducer", Nature **507**, 81–85 (2014) (cited on p. 19).

[48] N. J. Lambert, A. Rueda, F. Sedlmeir, and H. G. L. Schwefel, “Coherent conversion between microwave and optical photons – an overview of physical implementations”, Advanced Quantum Technologies **3**, 1900077 (2020) (cited on p. 19).

[49] R. Sahu, W. Hease, A. Rueda, G. Arnold, L. Qiu, and J. M. Fink, “Quantum-enabled operation of a microwave-optical interface”, Nature Communications **13**, 1276 (2022) (cited on p. 19).

[50] M. Mirhosseini, A. Sipahigil, M. Kalaee, and O. Painter, “Superconducting qubit to optical photon transduction”, Nature **588**, 599–603 (2020) (cited on p. 19).

[51] A. Suleymanzade, “Millimeter Wave Photons For Hybrid Quantum Systems”, PhD thesis (The University of Chicago, 2021) (cited on pp. 21, 31, 62).

[52] M. Stone, “Hybrid Cavity QED with Rydberg Atoms”, PhD thesis (The University of Chicago, 2021) (cited on pp. 21, 35, 46).

[53] C.-H. Wang, M. Zhang, and L. Jiang, “Generalized matching condition for unity efficiency quantum transduction”, Physical Review Research **4**, L042023 (2022) (cited on pp. 25, 78, 93).

[54] Y. Zhu, D. J. Gauthier, S. E. Morin, Q. Wu, H. J. Carmichael, and T. W. Mossberg, “Vacuum Rabi splitting as a feature of linear-dispersion theory: Analysis and experimental observations”, Physical Review Letters **64**, 2499–2502 (1990) (cited on p. 27).

[55] Z. Chen, “Breaking Quantum Limits with Collective Cavity-QED: Generation of Spin Squeezed States via Quantum Non-Demolition Measurements”, PhD thesis (CU Boulder, 2011) (cited on p. 31).

[56] J. Ningyuan, A. Georgakopoulos, A. Ryou, N. Schine, A. Sommer, and J. Simon, “Observation and characterization of cavity Rydberg polaritons”, Physical Review A **93**, 041802 (2016) (cited on p. 28).

[57] N. Jia, N. Schine, A. Georgakopoulos, A. Ryou, L. W. Clark, A. Sommer, and J. Simon, "A strongly interacting polaritonic quantum dot", Nature Physics **14**, 550–554 (2018) (cited on p. 28).

[58] M. D. Lukin, M. Fleischhauer, M. O. Scully, and V. L. Velichansky, "Intracavity electromagnetically induced transparency", Optics Letters **23**, 295–297 (1998) (cited on p. 28).

[59] M. D. Lukin, "*Colloquium* : Trapping and manipulating photon states in atomic ensembles", Reviews of Modern Physics **75**, 457–472 (2003) (cited on p. 28).

[60] M. Fleischhauer, A. Imamoglu, and J. P. Marangos, "Electromagnetically induced transparency: Optics in coherent media", Reviews of Modern Physics **77**, 633–673 (2005) (cited on p. 28).

[61] R. Loudon, *The quantum theory of light* (OUP Oxford, 2000) Chap. 6, p. 249 (cited on p. 49).

[62] E. Zeuthen, A. Schliesser, A. S. Sørensen, and J. M. Taylor, "Figures of merit for quantum transducers", Quantum Science and Technology **5**, 034009 (2020) (cited on p. 60).

[63] B. M. Brubaker, J. M. Kindem, M. D. Urmey, S. Mittal, R. D. Delaney, P. S. Burns, M. R. Vissers, K. W. Lehnert, and C. A. Regal, "Optomechanical Ground-State Cooling in a Continuous and Efficient Electro-Optic Transducer", Physical Review X **12**, 021062 (2022) (cited on p. 60).

[64] M. Pechal and A. H. Safavi-Naeini, "Millimeter-wave interconnects for microwave-frequency quantum machines", Physical Review A **96**, 042305 (2017) (cited on p. 62).

[65] A. W. Bruch, X. Liu, J. B. Surya, C.-L. Zou, and H. X. Tang, "On-chip $\chi^{(2)}$ microring optical parametric oscillator", Optica **6**, 1361–1366 (2019) (cited on p. 64).

[66] A. R. Wade, G. L. Mansell, S. S. Y. Chua, R. L. Ward, B. J. J. Slagmolen, D. A. Shaddock, and D. E. McClelland, “A squeezed light source operated under high vacuum”, Scientific Reports **5**, 18052 (2015) (cited on p. 64).

[67] S. F. Pereira, M. Xiao, H. J. Kimble, and J. L. Hall, “Generation of squeezed light by intracavity frequency doubling”, Physical Review A **38**, 4931–4934 (1988) (cited on p. 64).

[68] A. Ahlrichs, “Triply-Resonant Cavity-Enhanced Spontaneous Parametric Down-Conversion”, PhD thesis (Mathematisch-Naturwissenschaftliche Fakultät, July 2019) (cited on pp. 64, 66).

[69] X. Wang, X. Jiao, B. Wang, Y. Liu, X.-P. Xie, M.-Y. Zheng, Q. Zhang, and J.-W. Pan, “Quantum frequency conversion and single-photon detection with lithium niobate nanophotonic chips”, npj Quantum Information **9**, 1–7 (2023) (cited on pp. 64, 66, 67).

[70] J.-Y. Chen, Z. Li, Z. Ma, C. Tang, H. Fan, Y. M. Sua, and Y.-P. Huang, “Photon Conversion and Interaction in a Quasi-Phase-Matched Microresonator”, Physical Review Applied **16**, 064004 (2021) (cited on pp. 64, 66, 67).

[71] R. Gao, H. Zhang, F. Bo, W. Fang, Z. Hao, N. Yao, J. Lin, J. Guan, L. Deng, M. Wang, L. Qiao, and Y. Cheng, “Broadband highly efficient nonlinear optical processes in on-chip integrated lithium niobate microdisk resonators of Q-factor above 108”, New Journal of Physics **23**, 123027 (2021) (cited on pp. 64, 66, 67).

[72] R. W. Boyd, *Nonlinear optics, third edition*, 3rd (Academic Press, Inc., USA, 2008) (cited on pp. 64, 66, 92, 149, 150).

[73] D. Bouwmeester, J.-W. Pan, M. Daniell, H. Weinfurter, and A. Zeilinger, “Observation of Three-Photon Greenberger-Horne-Zeilinger Entanglement”, Physical Review Letters **82**, 1345–1349 (1999) (cited on p. 66).

[74] A. Mair, A. Vaziri, G. Weihs, and A. Zeilinger, “Entanglement of the orbital angular momentum states of photons”, Nature **412**, 313–316 (2001) (cited on p. 66).

[75] T. van Leent, M. Bock, F. Fertig, R. Garthoff, S. Eppelt, Y. Zhou, P. Malik, M. Seubert, T. Bauer, W. Rosenfeld, W. Zhang, C. Becher, and H. Weinfurter, “Entangling single atoms over 33 km telecom fibre”, Nature **607**, 69–73 (2022) (cited on p. 66).

[76] T. Van Leent, M. Bock, R. Garthoff, K. Redeker, W. Zhang, T. Bauer, W. Rosenfeld, C. Becher, and H. Weinfurter, “Long-Distance Distribution of Atom-Photon Entanglement at Telecom Wavelength”, Physical Review Letters **124**, 010510 (2020) (cited on p. 66).

[77] S. Kucera, C. Haen, E. Arenskötter, T. Bauer, J. Meiers, M. Schäfer, R. Boland, M. Yahyapour, M. Lessing, R. Holzwarth, C. Becher, and J. Eschner, “Demonstration of quantum network protocols over a 14-km urban fiber link”, npj Quantum Information **10**, 1–11 (2024) (cited on p. 66).

[78] E. Arenskötter, T. Bauer, S. Kucera, M. Bock, J. Eschner, and C. Becher, “Telecom quantum photonic interface for a 40Ca+ single-ion quantum memory”, npj Quantum Information **9**, 1–8 (2023) (cited on p. 66).

[79] M. Bock, P. Eich, S. Kucera, M. Kreis, A. Lenhard, C. Becher, and J. Eschner, “High-fidelity entanglement between a trapped ion and a telecom photon via quantum frequency conversion”, Nature Communications **9**, 1998 (2018) (cited on p. 66).

[80] E. Bersin, M. Sutula, Y. Q. Huan, A. Suleymanzade, D. R. Assumpcao, Y.-C. Wei, P.-J. Stas, C. M. Knaut, E. N. Knall, C. Langrock, N. Sinclair, R. Murphy, R. Riedinger, M. Yeh, C. Xin, S. Bandyopadhyay, D. D. Sukachev, B. Machielse, D. S. Levonian, M. K. Bhaskar, S. Hamilton, H. Park, M. Lončar, M. M. Fejer, P. B. Dixon, D. R. Englund, and M. D. Lukin, “Telecom Networking with a Diamond Quantum Memory”, PRX Quantum **5**, 010303 (2024) (cited on p. 66).

[81] A. Tchebotareva, “Entanglement between a Diamond Spin Qubit and a Photonic Time-Bin Qubit at Telecom Wavelength”, Physical Review Letters **123**, `10.1103/PhysRevLett.123.063601` (2019) (cited on p. 66).

[82] W. P. Risk, T. R. Gosnell, and A. V. Nurmikko, *Compact blue-green lasers* (Cambridge University Press, Cambridge, 2003) (cited on p. 66).

[83] C. Wang, C. Langrock, A. Marandi, M. Jankowski, M. Zhang, B. Desiatov, M. M. Fejer, and M. Lončar, “Ultrahigh-efficiency wavelength conversion in nanophotonic periodically poled lithium niobate waveguides”, Optica **5**, 1438–1441 (2018) (cited on p. 66).

[84] J.-Y. Chen, Z.-H. Ma, Y. M. Sua, Z. Li, C. Tang, and Y.-P. Huang, “Ultra-efficient frequency conversion in quasi-phase-matched lithium niobate microrings”, Optica **6**, 1244–1245 (2019) (cited on p. 66).

[85] R. Ikuta, M. Yokota, T. Kobayashi, N. Imoto, and T. Yamamoto, “Optical Frequency Tweezers”, Physical Review Applied **17**, 034012 (2022) (cited on p. 66).

[86] Y. Zhang, Y. Qi, Q. Sheng, J.-Q. Lü, H. Zheng, H. Guo, Z. Bai, Y. Wang, D. Yan, W. Shi, and Z. Lu, “640 nm High-Order Laguerre-Gaussian Modes with Controllable Topological Charge up to 42 from a Pr:YLF Laser with Intracavity Spherical Aberration”, ACS Photonics **11**, 4374–4379 (2024) (cited on p. 66).

[87] Y. Senatsky, J.-F. Bisson, J. Li, A. Shirakawa, M. Thirugnanasambandam, and K.-i. Ueda, “Laguerre-Gaussian modes selection in diode-pumped solid-state lasers”, Optical Review **19**, 201–221 (2012) (cited on p. 66).

[88] S. Ramelow, A. Farsi, Z. Vernon, S. Clemmen, X. Ji, J. E. Sipe, M. Liscidini, M. Lipson, and A. L. Gaeta, “Strong nonlinear coupling in a Si_3N_4 ring resonator”, Physical Review Letters **122**, 153906 (2019) (cited on p. 67).

[89] X. Guo, C.-L. Zou, H. Jung, and H. X. Tang, “On-chip strong coupling and efficient frequency conversion between telecom and visible optical modes”, Physical Review Letters **117**, 123902 (2016) (cited on p. 67).

[90] M. Stone, A. Suleymanzade, L. Taneja, D. I. Schuster, and J. Simon, “Optical mode conversion in coupled Fabry–Perot resonators”, Optics Letters **46**, 21 (2021) (cited on pp. 68, 85, 114, 134).

[91] S. A. Miller, Y. Okawachi, S. Ramelow, K. Luke, A. Dutt, A. Farsi, A. L. Gaeta, and M. Lipson, “Tunable frequency combs based on dual microring resonators”, Optics Express **23**, 21527–21540 (2015) (cited on p. 68).

[92] J. Poirson, F. Bretenaker, M. Vallet, and A. L. Floch, “Analytical and experimental study of ringing effects in a Fabry–Perot cavity. Application to the measurement of high finesses”, JOSA B **14**, 2811–2817 (1997) (cited on pp. 72, 96).

[93] D. M. S. Johnson, J. M. Hogan, S.-w. Chiow, and M. A. Kasevich, “Broadband optical serrodyne frequency shifting”, Optics Letters **35**, 745–747 (2010) (cited on p. 78).

[94] S. Guha and J. Falk, “The effects of focusing in the three-frequency parametric upconverter”, Journal of Applied Physics **51**, 50–60 (1980) (cited on pp. 81, 83, 97, 150).

[95] Y.-T. Chen, M. Szurek, B. Hu, J. de Hond, B. Braverman, and V. Vuletic, “High finesse bow-tie cavity for strong atom-photon coupling in Rydberg arrays”, Optics Express **30**, 37426–37435 (2022) (cited on pp. 81, 84, 105).

[96] M. Jaffe, L. Palm, C. Baum, L. Taneja, and J. Simon, “Aberrated optical cavities”, Physical Review A **104**, 013524 (2021) (cited on pp. 81, 96, 102, 105, 114).

[97] Y. Li and J. Thompson, *High-rate and high-fidelity modular interconnects between neutral atom quantum processors*, Jan. 2024 (cited on pp. 81, 84, 135).

[98] M. Leidinger, S. Fieberg, N. Waasem, F. Kühnemann, K. Buse, and I. Breunig, "Comparative study on three highly sensitive absorption measurement techniques characterizing lithium niobate over its entire transparent spectral range", Optics Express **23**, 21690–21705 (2015) (cited on pp. 83, 84, 97).

[99] J. Steinlechner, S. Ast, C. Krüger, A. P. Singh, T. Eberle, V. Händchen, and R. Schnabel, "Absorption measurements of periodically poled potassium titanyl phosphate (PPKTP) at 775 nm and 1550 nm", Sensors (Basel, Switzerland) **13**, 565–573 (2013) (cited on pp. 83, 97).

[100] J. R. Schwesyg, A. Markosyan, M. Falk, M. C. C. Kajiyama, D. H. Jundt, K. Buse, and M. M. Fejer, "Optical loss mechanisms in magnesium-doped lithium niobate crystals in the 300 to 2950 nm wavelength range", in Advances in Optical Materials (2011), paper AIThE3 (Feb. 2011), AIThE3 (cited on pp. 83, 84, 97).

[101] S. Anand, C. E. Bradley, R. White, V. Ramesh, K. Singh, and H. Bernien, "A dual-species Rydberg array", Nature Physics **20**, 1744–1750 (2024) (cited on pp. 84, 135).

[102] J. Ramette, J. Sinclair, Z. Vendeiro, A. Rudelis, M. Cetina, and V. Vuletić, "Any-To-Any Connected Cavity-Mediated Architecture for Quantum Computing with Trapped Ions or Rydberg Arrays", PRX Quantum **3**, 010344 (2022) (cited on p. 84).

[103] J. K. Thompson, J. Simon, H. Loh, and V. Vuletić, "A High-Brightness Source of Narrowband, Identical-Photon Pairs", Science **313**, 74–77 (2006) (cited on p. 84).

[104] K. F. Reim, P. Michelberger, K. C. Lee, J. Nunn, N. K. Langford, and I. A. Walmsley, "Single-Photon-Level Quantum Memory at Room Temperature", Physical Review Letters **107**, 053603 (2011) (cited on p. 84).

[105] S. Ritter, C. Nölleke, C. Hahn, A. Reiserer, A. Neuzner, M. Uphoff, M. Mücke, E. Figueroa, J. Bochmann, and G. Rempe, "An elementary quantum network of single atoms in optical cavities", Nature **484**, 195–200 (2012) (cited on p. 84).

[106] A. Reiserer and G. Rempe, “Cavity-based quantum networks with single atoms and optical photons”, Reviews of Modern Physics **87**, 1379–1418 (2015) (cited on p. 84).

[107] T. Kuga, Y. Torii, N. Shiokawa, T. Hirano, Y. Shimizu, and H. Sasada, “Novel Optical Trap of Atoms with a Doughnut Beam”, Physical Review Letters **78**, 4713–4716 (1997) (cited on p. 84).

[108] M. Saffman, T. G. Walker, and K. Mølmer, “Quantum information with Rydberg atoms”, Reviews of Modern Physics **82**, 2313–2363 (2010) (cited on p. 84).

[109] L. Zhu, A. Wang, S. Chen, J. Liu, and J. Wang, “Orbital angular momentum mode multiplexed transmission in heterogeneous few-mode and multi-mode fiber network”, Optics Letters **43**, 1894–1897 (2018) (cited on p. 84).

[110] A. E. Willner, Y. Ren, G. Xie, Y. Yan, L. Li, Z. Zhao, J. Wang, M. Tur, A. F. Molisch, and S. Ashrafi, “Recent advances in high-capacity free-space optical and radio-frequency communications using orbital angular momentum multiplexing”, Philosophical Transactions of the Royal Society A: Mathematical, Physical and Engineering Sciences **375**, 20150439 (2017) (cited on p. 84).

[111] H. Huang, G. Xie, Y. Yan, N. Ahmed, Y. Ren, Y. Yue, D. Rogawski, M. J. Willner, B. I. Erkmen, K. M. Birnbaum, S. J. Dolinar, M. P. J. Lavery, M. J. Padgett, M. Tur, and A. E. Willner, “100 Tbit/s free-space data link enabled by three-dimensional multiplexing of orbital angular momentum, polarization, and wavelength”, Optics Letters **39**, 197–200 (2014) (cited on p. 84).

[112] Z.-Y. Zhou, Y. Li, D.-S. Ding, W. Zhang, S. Shi, B.-S. Shi, and G.-C. Guo, “Orbital angular momentum photonic quantum interface”, Light: Science & Applications **5**, e16019–e16019 (2016) (cited on p. 84).

[113] F. Steinlechner, N. Hermosa, V. Pruneri, and J. P. Torres, “Frequency conversion of structured light”, Scientific Reports **6**, 21390 (2016) (cited on p. 84).

[114] J. Klaers, J. Schmitt, F. Vewinger, and M. Weitz, “Bose–Einstein condensation of photons in an optical microcavity”, Nature **468**, 545–548 (2010) (cited on p. 84).

[115] L. O. Castaños-Cervantes, L. M. Procopio, and M. Enríquez, “Coherent control of two Jaynes–Cummings cavities”, Scientific Reports **14**, 3790 (2024) (cited on p. 84).

[116] N. Miladinovic, F. Hasan, N. Chisholm, I. E. Linnington, E. A. Hinds, and D. H. J. O’Dell, “Adiabatic transfer of light in a double cavity and the optical Landau-Zener problem”, Physical Review A **84**, 043822 (2011) (cited on p. 84).

[117] J. Larson and E. Andersson, “Cavity-state preparation using adiabatic transfer”, Physical Review A: Atomic, Molecular, and Optical Physics **71**, 053814 (2005) (cited on p. 84).

[118] Schott, *Optical Glass Datasheets*, tech. rep. (2023) (cited on p. 97).

[119] H. E. Bennett and J. O. Porteus, “Relation Between Surface Roughness and Specular Reflectance at Normal Incidence”, JOSA **51**, 123–129 (1961) (cited on pp. 98, 99).

[120] K. H. Guenther, P. G. Wierer, and J. M. Bennett, “Surface roughness measurements of low-scatter mirrors and roughness standards”, Applied Optics **23**, 3820–3836 (1984) (cited on p. 98).

[121] M. Jaffe, L. Palm, C. Baum, L. Taneja, A. Kumar, and J. Simon, “Understanding and suppressing backscatter in optical resonators”, Optica **9**, 878 (2022) (cited on p. 99).

[122] H. Kogelnik, “Imaging of Optical Modes - Resonators with Internal Lenses”, Bell System Technical Journal **44**, 455–494 (1965) (cited on p. 100).

[123] R. V. Pole, “Conjugate-Concentric Laser Resonator”, JOSA **55**, 254–260 (1965) (cited on pp. 100, 103).

[124] Z. Xu, S. Zhang, Y. Li, and W. Du, “Adjustment-free cat’s eye cavity He-Ne laser and its outstanding stability”, Optics Express **13**, 5565–5573 (2005) (cited on p. 100).

[125] N. Schine, A. Ryou, A. Gromov, A. Sommer, and J. Simon, “Synthetic Landau levels for photons”, Nature **534**, 671–675 (2016) (cited on pp. 101, 105, 132).

[126] L. W. Clark, N. Schine, C. Baum, N. Jia, and J. Simon, “Observation of Laughlin states made of light”, Nature **582**, 41–45 (2020) (cited on pp. 101, 105).

[127] J. A. Arnaud, “Degenerate Optical Cavities”, Applied Optics **8**, 189–196 (1969) (cited on p. 103).

[128] A. Periwal, E. S. Cooper, P. Kunkel, J. F. Wienand, E. J. Davis, and M. Schleier-Smith, “Programmable interactions and emergent geometry in an array of atom clouds”, Nature **600**, 630–635 (2021) (cited on p. 103).

[129] D. Goldovsky, V. Jouravsky, and A. Pe’er, “Simple and robust phase-locking of optical cavities with $>$ 200 KHz servo-bandwidth using a piezo-actuated mirror mounted in soft materials”, Optics Express **24**, 28239–28246 (2016) (cited on p. 110).

[130] J. F. Kelly and A. Gallagher, “Efficient electro-optic modulator for optical pumping of Na beams”, Review of Scientific Instruments **58**, 563–566 (1987) (cited on p. 112).

[131] A. Sommer and J. Simon, “Engineering photonic Floquet Hamiltonians through Fabry–Pérot resonators”, New Journal of Physics **18**, 035008 (2016) (cited on pp. 118, 126).

[132] https://github.com/tanejalavanya/thesis, Mar. 2025 (cited on pp. 127, 130).

[133] S. Kar, D. Sahdev, and B. Bhawal, “Scalar waves in a wormhole geometry”, Physical Review D **49**, 853–861 (1994) (cited on p. 132).

[134] https://kingfisherfiber.com/, Mar. 2025 (cited on p. 134).

[135] J. P. Covey, A. Sipahigil, and M. Saffman, “Microwave-to-optical conversion via four-wave mixing in a cold ytterbium ensemble”, Physical Review A **100**, 012307 (2019) (cited on p. 134).

[136] R. C. Bialczak, M. Ansmann, M. Hofheinz, M. Lenander, E. Lucero, M. Neeley, A. D. O'Connell, D. Sank, H. Wang, M. Weides, J. Wenner, T. Yamamoto, A. N. Cleland, and J. M. Martinis, "Fast Tunable Coupler for Superconducting Qubits", Physical Review Letters **106**, 060501 (2011) (cited on p. 135).

[137] D. L. Campbell, A. Kamal, L. Ranzani, M. Senatore, and M. D. LaHaye, "Modular Tunable Coupler for Superconducting Circuits", Physical Review Applied **19**, 064043 (2023) (cited on p. 135).

[138] P. Roushan, C. Neill, A. Megrant, Y. Chen, R. Babbush, R. Barends, B. Campbell, Z. Chen, B. Chiaro, A. Dunsworth, A. Fowler, E. Jeffrey, J. Kelly, E. Lucero, J. Mutus, P. J. J. O'Malley, M. Neeley, C. Quintana, D. Sank, A. Vainsencher, J. Wenner, T. White, E. Kapit, H. Neven, and J. Martinis, "Chiral ground-state currents of interacting photons in a synthetic magnetic field", Nature Physics **13**, 146–151 (2017) (cited on p. 135).

[139] L. Li and A. Kuzmich, "Quantum memory with strong and controllable Rydberg-level interactions", Nature Communications **7**, 13618 (2016) (cited on p. 135).

[140] M. Tada, Y. Kishimoto, K. Kominato, M. Shibata, H. Funahashi, K. Yamamoto, A. Masaike, and S. Matsuki, "CARRACK II — a new large-scale experiment to search for axions with Rydberg-atom cavity detector", Nuclear Physics B - Proceedings Supplements, Proceedings of the 5th IFT Workshop on Axions **72**, 164–168 (1999) (cited on p. 137).

[141] N. Šibalić, J. D. Pritchard, C. S. Adams, and K. J. Weatherill, "ARC: An open-source library for calculating properties of alkali Rydberg atoms", Computer Physics Communications **220**, 319–331 (2017) (cited on p. 144).